






**(Project Number: 945 041)**

**D3.4 Detailed study of conditions  
in isolated DHR loop in long-term reactor operation**

Authors	Due date:	30/09/2022
P. Zách, V. Železný	Actual release date:	29/09/2022
	Version:	1.0

Approved by MST	Coordinator
Jakub Heller	Branislav Hatala
	

Version number: 1.0

Initially released on: 12/02/2022

Final version released on: 29/09/2022

Project start date: 01/10/2020

Project duration: 48 months

Dissemination level			
PU	Public	X	
RE	Restricted to specific group		
CO	Confidential (only for SafeG partners)		

**Project information**

Project full title:	Safety of GFR through innovative materials, technologies and processes
Acronym:	SafeG
Funding scheme:	Research and innovation action
ECGA number:	945041
Programme and call	Horizon 2020 Framework Programme for Research and Innovation (2014-2020) NFRP-2019-2020 (Nuclear Fission and Radiation Protection Research)
Coordinator:	Dr. Branislav Hatala
EC Project Officer:	Cristina Fernandez Ramos
Start date – End date:	01/10/20 – 30/09/2024 i.e. 48 months
Coordinator contact:	+421 905 567 985, <a href="mailto:Branislav.hatala@vuje.sk">Branislav.hatala@vuje.sk</a>
Administrative contact:	+420 602 771 784, <a href="mailto:jakub.heller@evalion.cz">jakub.heller@evalion.cz</a>
Online contacts (website):	<a href="http://www.safeg.eu">www.safeg.eu</a>



„This project has received funding from the Euratom research and training programme 2019-2020 under grant agreement No 945041”.

# 1 COPYRIGHT

The document is proprietary of the SafeG consortium members. No copying or distributing, in any form or by any means, is allowed without the prior written agreement of the owner of the property rights. This document reflects only the authors' view. The European Community is not liable for any use that may be made of the information contained herein.

## 1.1 CONTENT

1	Copyright.....	3
1.1	CONTENT .....	4
2	INTRODUCTION .....	6
3	DHR System Description .....	7
3.1	ALLEGRO 2009 DHR System Description .....	7
3.1.1	DHR concept .....	7
3.1.2	Primary circuit of the DHR system .....	9
3.1.3	Secondary circuit of the DHR system and final heat sink.....	9
3.2	Design changes at the start of the work.....	14
4	Computational domain.....	16
4.1	Test Model .....	16
4.2	Complex Model .....	17
4.2.1	geometry of the internal volume of the heat exchanger tubes .....	18
4.2.2	Cold leg geometry .....	18
5	Computational mesh .....	20
5.1	Test Model .....	20
5.1.1	Hot leg and heat exchanger .....	20
5.1.2	Computational mesh quality .....	25
5.2	Complex Model .....	26
5.2.1	Changes for hot leg and heat exchanger .....	27
5.2.2	Cold leg .....	30
5.2.3	Computational mesh quality .....	32
6	Numerical model definitions .....	34
6.1	Solver settings.....	34
6.2	Settings of thermophysical properties of used materials.....	34
6.2.1	Helium .....	34
6.2.2	Water .....	35
6.2.3	Material of heat exchanger tubes.....	36
6.2.4	Insulation .....	37
7	Test Model calculations .....	39
7.1	Boundary conditions .....	39
7.2	Solution and results .....	39
7.3	Summary .....	42

8	Complex Model calculations .....	43
8.1	Nominální provozní stav Nominal operational state .....	43
8.1.1	Boundary conditions.....	43
8.1.2	Solution and results.....	44
8.2	Havarijní stav Emergency condition .....	48
8.2.1	Solved scenario.....	49
8.2.2	Transient calculation – first phase .....	51
8.2.3	Transient calculation - second phase .....	56
8.3	Summary .....	66
9	Conclusion.....	67
10	REFERENCES.....	68

## 2 INTRODUCTION

The objective of Deliverable D3.4 ("Detailed study of conditions in isolated DHR loop in long-term reactor operation") was to build a fully functional CFD computational model for simulations of selected states and processes of the DHR loop of the helium-cooled ALLEGRO reactor.

The development of the model was based on the defined design of the DHR system, which is described in Chapter 3. The actual solution of the CFD model, described in Chapters 4 to 6, consists of two basic steps that enabled gradual achievement of the desired goal. In the first step, a computational study of a separate hot leg of the DHR loop including the actual heat exchanger (the so-called Test Model) was performed. This allowed to gradually implement geometric simplifications (symmetry, geometry of solid parts, application of the "thin wall" function, etc.), to analyze the computational mesh created, to optimize boundary conditions and to find suitable numerical approaches to the solution (turbulent models, numerical schemes, etc.). In the second step, the entire geometry of the DHR loop, i.e. including the cold leg (the so-called "Complex Model"), has already been modelled and simulated computationally. Apart from the addition of the cold leg, this model also includes modifications to the geometry and computational mesh in the hot leg and DHR exchanger area, which reflects the results of the previous analysis on the Test Model. Calculations simulating the nominal state and the defined transient process (design accident with total loss of power - SBO) were then performed on the Complex Model.

For better readability, the procedure describing the preparation of both models is merged into chapters, starting with the preparation of the geometry, through the creation of the computational mesh, the determination of the calculation conditions, up to the realized simulations.

ANSYS SpaceClaim 19.0 was used to prepare the geometry, GAMBIT 2.4.6 and ANSYS Fluent Meshing 2021 were used to create the computational mesh, and ANSYS Fluent 2021 was used for CFD calculations [1], [2].

### 3 DHR SYSTEM DESCRIPTION

#### 3.1 ALLEGRO 2009 DHR SYSTEM DESCRIPTION

In the following chapters, the CEA ALLEGRO 2009 design of the DHR system is described, both from operation and geometry points of view. Some parts of the system were originally not designed in detail and the work was done in UJV. It concerns mainly the secondary (water) circuit of the system.

##### 3.1.1 DHR CONCEPT

ALLEGRO features dedicated DHR system, which should be originally used to dissipate decay heat whenever the reactor is out of operation and in all accident situations [3]. Newer approach has been prepared, where dedicated DHR system is used as the second option for decay heat removal, only when the main primary loops are not available to do so [4].

During the normal operation, heat is transferred to the secondary circuit via the MHXs. In case of a transient (automatically in the original DHR concept, and in case of unavailability of pony motors in the new concept), residual heat removal is transferred to the DHR loops. This sequence starts with isolation of the main primary loops. It is ensured by check-valves installed inside the MHXs, which close the flow path when the flow rate through a main primary loop drops under 3 % of the nominal value [5].

Shortly after the main check-valves are closed, check-valves in each of the DHR loops open and the transition of core cooling from main to DHR loops is complete.

If the DHR blowers are available, they start immediately after trip of the main blowers and the system operates in forced convection mode. However, the whole DHR system is designed to be able to work also in natural convection mode, e.g. in case of full station blackout. Both DHR concepts are summarized in Table 1.

**Table 1 DHR options in ALLEGRO**

DHR option	Original Strategy	Innovative strategy
1	DHR circuit in forced convection	Primary circuit in forced convection
2	DHR circuit in natural convection	DHR circuit in forced convection
3	x	DHR circuit in natural convection

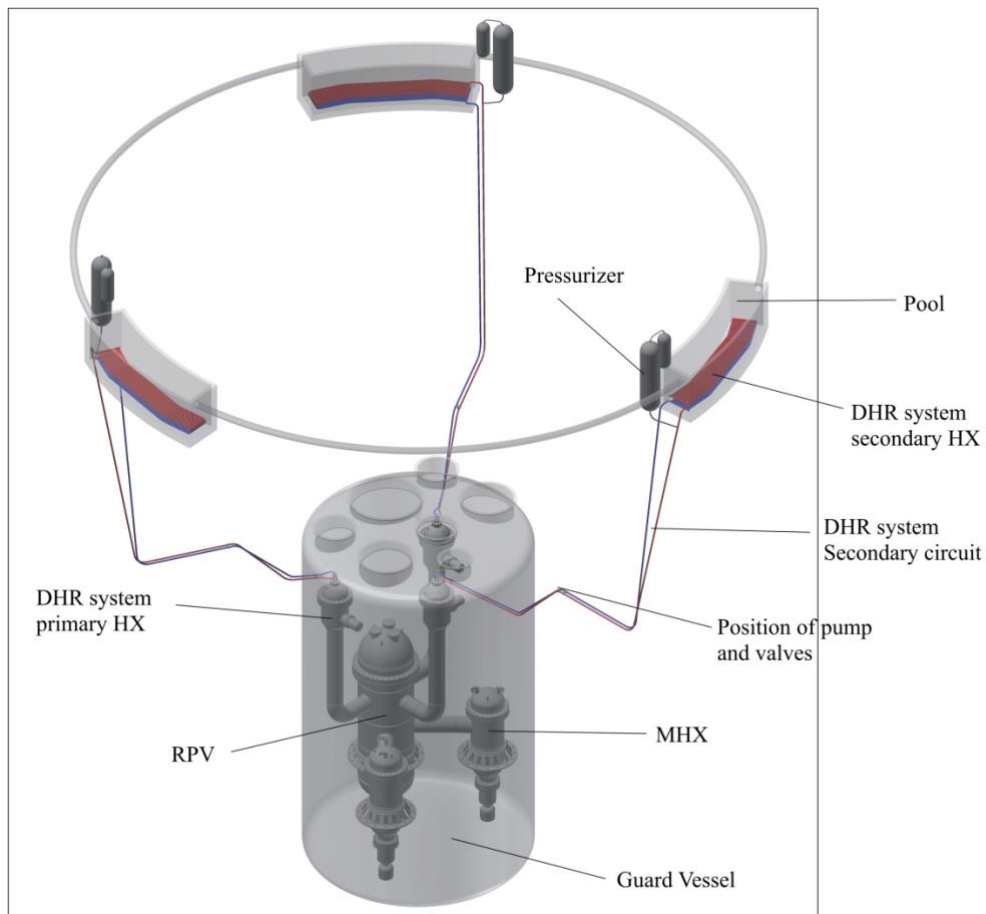


Figure 1 ALLEGRO DHR system overview

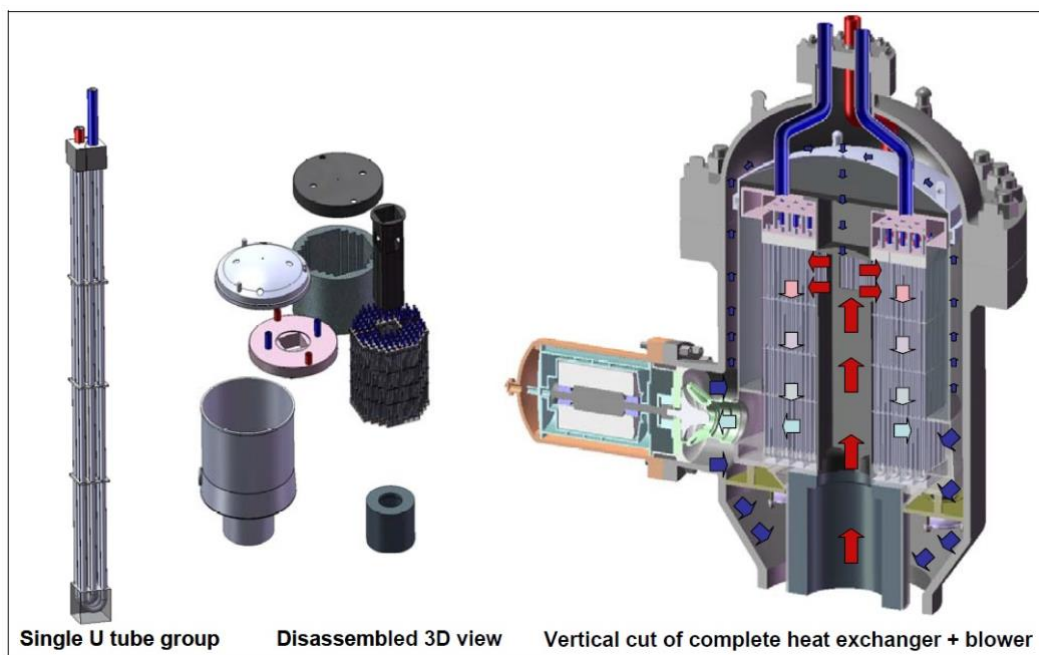


Figure 2 Detail of DHR system primary HX [3]



### 3.1.2 PRIMARY CIRCUIT OF THE DHR SYSTEM

ALLEGRO CEA 2009 concept features 3 identical DHR loops, with heat exchangers located high above the core to favor natural circulation. Complete overview of the system is in Figure 1, detail of the primary heat exchanger in a DHR loop is in Figure 2, including the flow path of helium on the primary side. Additional information about DHR system can be found in [6].

### 3.1.3 SECONDARY CIRCUIT OF THE DHR SYSTEM AND FINAL HEAT SINK

Design of DHR system secondary circuit has been done in UJV, based on specifications and assumptions used by CEA and others in various documents such as [5] and CATHARE models.

Secondary circuit of the DHR system uses water as the medium. Each of the three circuits is independent on the two others. Each circuit consist of components typical for water circuits:

- pump, designed to be passively bypassed if the circuit operates in natural circulation mode
- volume compensator
- pair of isolation check-valves on both the hot and cold leg of the circuit to prevent excessive water ingress to primary circuit in case of loss of DHR primary HX tightness
- heat exchanger submerged in a pool located under the top head of the main containment.

Design pressure of circuit is  $1\text{ MPa}$  [5].

#### 3.1.3.1 U-tubes and collectors inside the DHR primary HX

The part of the secondary (water) DHR circuit inside the main HX consist of water collectors (for hot and cold water) and the actual heat-exchanging U-tubes. These components are part of the original CEA design.

The collectors consist of two chambers separated by a plate, cold water is collected from the upper chamber, hot from the lower one. U-tube bundle is composed of 104 individual U-tube groups, comprising 4 U-tubes each (they are depicted in the left part of Figure 2). In total, there are 416 U-tubes with outer diameter  $20\text{ mm}$  and wall thickness  $1\text{ mm}$ , giving total heat exchanging area  $86.2\text{ m}^2$  for one DHR primary HX.

Cross-section of the collectors showing the principle of water distribution into/from U-tubes is depicted in Figure 3.

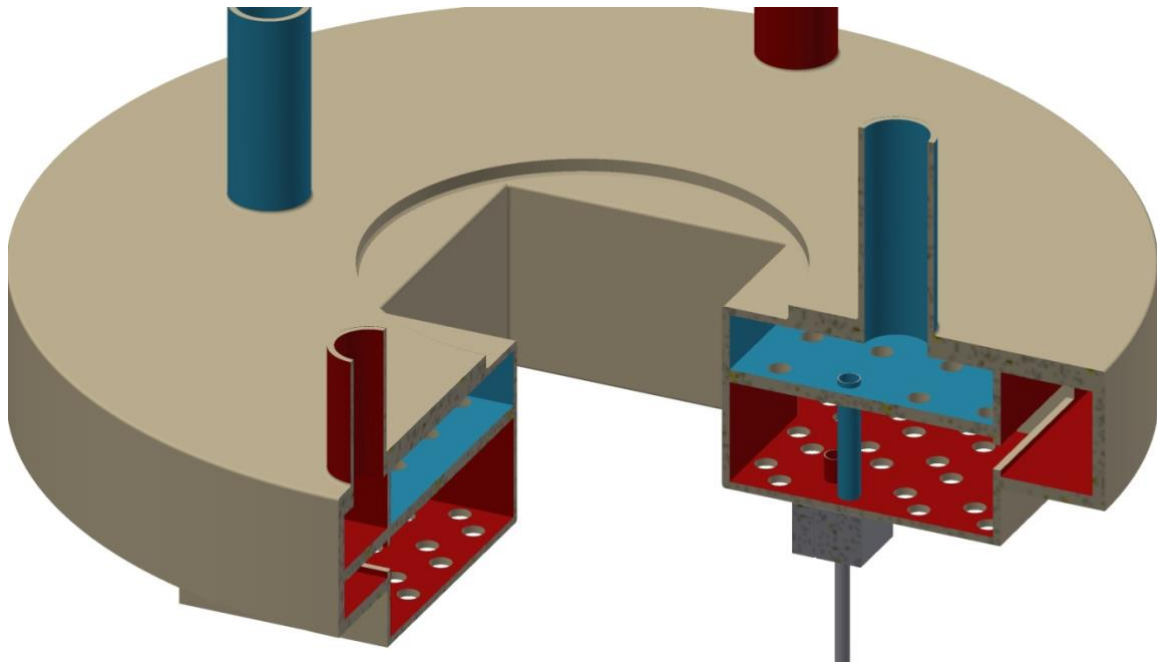


Figure 3 Hot and cold water collectors in DHR MHX

### 3.1.3.2 DHR system secondary system duct

Both cold and hot leg of the secondary duct consist of SS tubes of inner diameter *100 mm* and wall thickness *10 mm*. There are 4 pipes coming from/to each DHR primary HX, these tubes are, close to the exchanger, connected in pairs to just one hot and one cold. There are slight differences in the shape and length of individual ducts, caused by other components in GV and containment. The overall length of the 6 respective ducts is summarized in Table 2.

Table 2 Lengths of DHR system secondary ducts

Duct	Hot leg 1	Hot leg 2	Hot leg 3	Cold leg 1	Cold leg 2	Cold leg 3
Length (m)	42.473	37.145	36.229	40.621	36.101	36.138

### 3.1.3.3 Check-valves in the DHR secondary circuit duct

A pair of check-valves is installed on both legs to prevent water ingress inside primary circuit of the reactor in case of loss of tightness inside the water circuit. Design of the valves was selected according to demand of maximum reliability of the solution and minimal pressure loss in open state to favor natural circulation in case of full blackout. The position of the valves in the duct is a result of compromise between being as-close-as-possible to the primary DHR system HX (to minimize the amount of water which would enter the primary circuit) and possibility to hand-operate the valves in case of unavailability of their remote control. The valves are depicted in Figure 4.

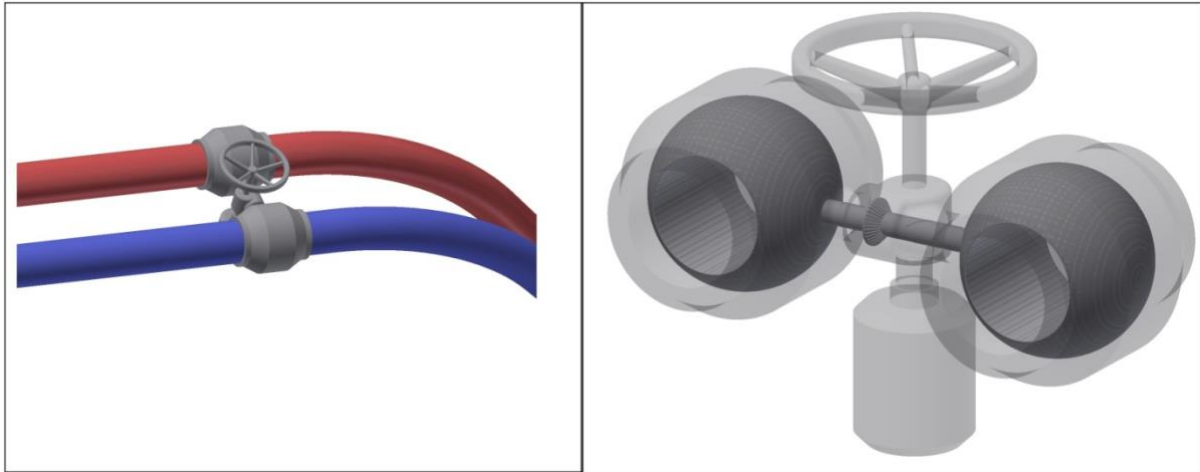


Figure 4 Isolation valves in DHR secondary circuit

### 3.1.3.4 Pressurizer

Each of the three secondary circuit loops is equipped with a pressurizer, located on hot leg near the pool. It is designed as the type of pressurizer with nitrogen atmosphere keeping the desired pressure, because of higher reliability in case of blackout. The nitrogen tank is located inside containment close to the pressurizer. Pressure relieve valves are located on top of pressurizer with outlet to the containment. Preliminary threshold pressure for opening the valves was set to  $2\text{ MPa}$ . Please note that design of pressurizer is very preliminary as for 10/2016.

### 3.1.3.5 Secondary heat exchanger

Secondary heat exchanger of the DHR system is located inside the water pool under the top of containment building. The exchanger was designed in UJV, selected solutions aimed at maximum simplicity, reliability and robustness, taking into account desirability of favoring natural circulation mode of operation.

Boundary conditions, taken into account in the preliminary calculations, are summarized in Table 3.

**Table 3 Boundary conditions for designing process of DHR secondary HX**

Boundary condition	Value
Overall heat transfer	2.6 MW
Inlet/outlet T in tube side	180 °C / 110 °C
Inlet/outlet T on shell side	50 °C / 100 °C
Global heat transfer coeff.	<500 W/m <sup>2</sup> K

All the values were selected with the highest rational amount of conservatism. Decay power to be transferred through the exchanger was taken to be equal to the total decay power in the reactor after 50 s from shutdown, with values of decay power taken from [6]. Inlet temperature on the tube side is the saturation temperature of water at  $1\text{ MPa}$ , temperatures on the shell side are nominal temperature of the pool (50 °C) and

saturation temperature at  $0.1 \text{ MPa}$ . Outlet temperature on the shell side was selected based on engineering judgment. Global heat transfer coefficient limitation was set according to typical values for naturally circulating water in shell-and-tube heat exchanger without boiling. If the designed heat exchanger fulfills all these criteria, it is ensured that it will be able to dissipate decay heat in all the other situations (boiling of water on the shell side, forced convection in the tube side) as well, as long as the exchanger is submerged in water.

Preliminary design of the needed heat exchanger surface area was done according to well-known equation:

$$Q = \alpha \cdot S \cdot \Delta T_m ,$$

where:

$Q$  is the total heat transfer (W)

$\alpha$  is the global heat transfer coefficient ( $\text{W}/\text{m}^2\cdot\text{K}$ )

$S$  is the total outside heat transfer area ( $\text{m}^2$ )

$\Delta T_m$  is the logarithmic mean temperature difference ( $^{\circ}\text{C}$ )

The only unknown in the equation is the surface area of the exchanger, which was calculated from the above presented equation in the form:

$$S = \frac{Q}{\alpha \cdot \Delta T_m} ,$$

For the values showed in Table 3, the minimal heat exchange area is:

$$S = \frac{2.6 \cdot 10^6}{500 \cdot 33.66} = 154.5 \text{ m}^2 .$$

The final design of the secondary DHR heat exchanger is horizontal U-tube heat exchanger with 36 finned tubes made of stainless steel. Total heat exchange area is  $161.2 \text{ m}^2$ . It is depicted in Figure 5.

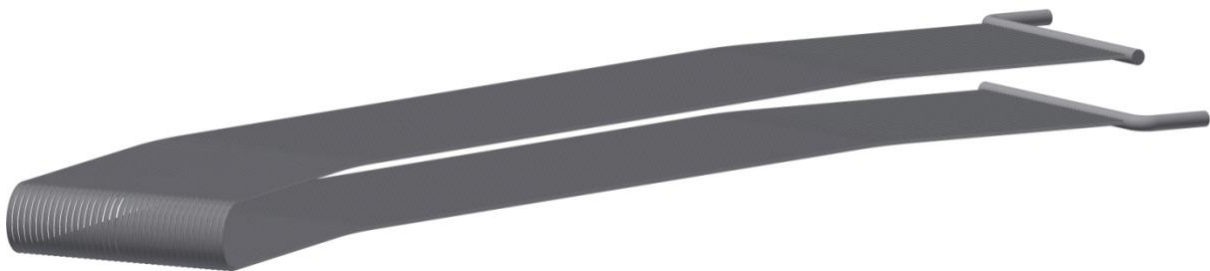


Figure 5 HX in DHR system secondary circuit

### 3.1.3.6 Pump

Presented solution is a preliminary design of the pump in the DHR secondary circuit, more precise sizing will need to be done. Since a water pump is a very common component, it should not be much of a problem. Authors focused more on possibility of passive bypass

system to allow smooth operation in natural circulation. It is presented in Figure 6 and Figure 7, and features a flap with spring on the pump outlet. In natural circulation mode, the flap is in the bottom position and the pump is completely bypassed. When the pump is started, it induces pressure to the flap, moving it into upper position and blocking the previous flow path. Detail CFD study and experiment will be needed to prove this solution.

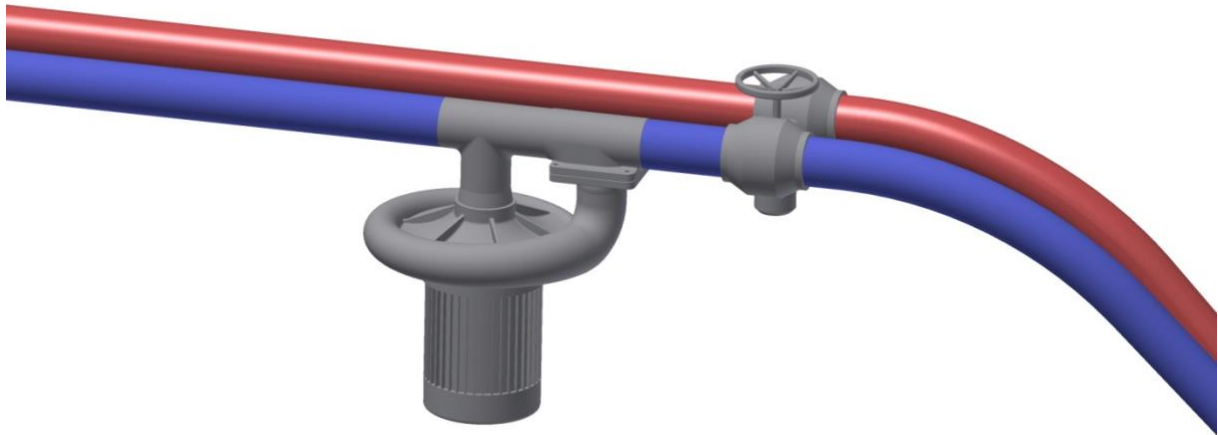


Figure 6 Pump in the DHR system secondary circuit



Figure 7 Detail of the bypass solution

### 3.1.3.7 Pool

There are three pools of water, one for each DHR secondary heat exchanger. Each of the pool can be refilled through a one-way valve located in containment building. The pools are interconnected by a duct near their top (see Figure 1), so all three pools can be refilled through only one of them. The position of the interconnecting duct is selected to prevent draining of other pools in case that one of them would be damaged.

Volume of water in each pool was calculated to be able to dissipate (mainly through evaporation) total decay heat for 5 days after shutdown ( $212\text{ GJ}$ , calculated from decay heat curve in [6]), and is equal to  $94\text{ m}^3$ . Volume of the inside of pool itself (up to the lowest point of the connecting duct) is  $96\text{ m}^3$ .

### 3.2 DESIGN CHANGES AT THE START OF THE WORK

It is assumed that an innovation of the initial DHR system design will be achieved during the project implementation, within Task 3.1. Although it is not possible to cover the changes in work done within Task 3.3 due to their time concurrence, some of the changes were already considered unavoidable right at the start of the two tasks. The most important of these changes being switch from the vertical U-tube design to a straight tube design of the primary DHR heat exchanger.

Vertical U-tube design fails at natural convection heat dissipation. If the pump in the DHR cooling circuit fails, or is not present at all (to achieve higher level of passiveness of the system), the flow inside the vertical U-tubes starts to be compromised due to even heat-up of both the cold and the hot side, that will lead to rapid overheating and failure of the top sections of the both parts of the U-tube (see Figure 8).

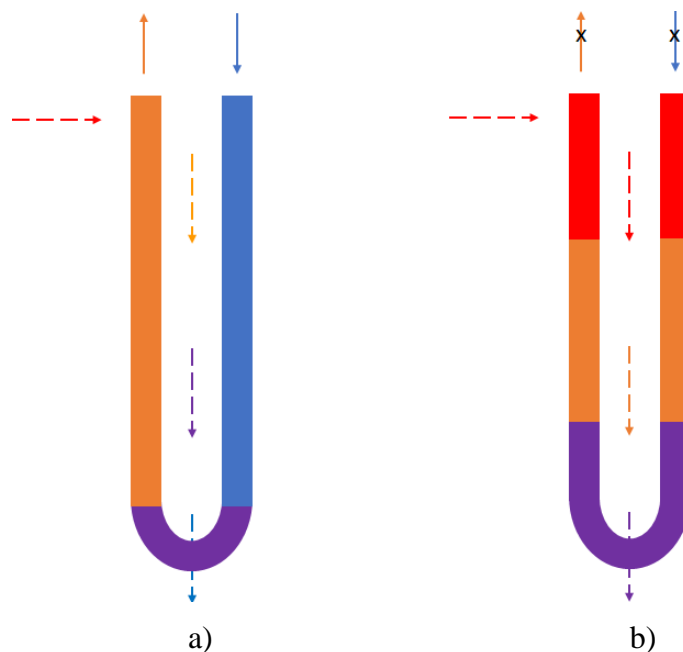


Figure 8 Temperature of U-tubes in forced circulation mode inside (a) vs. in natural circulation mode (b)

Therefore, all the analyses done within T3.3 already assume that straight tube heat exchanger will be used in the DHR system, and the problems are modeled using this assumption.

Figure 9 shows a detail of a part (1/12 of geometry) of the newly designed heat exchanger with straight heat transfer tubes. It can be seen that the cooling water is fed into the heat exchanger through a distribution chamber located at the bottom of the heat exchanger.

The upper part of this chamber is made up as a tube plate into which 810 heat exchanger tubes are routed. Tubes are arranged in 9 concentric rows of 90 tubes in each of them. After passing through the heat exchanger tubes, the water flows into a collection chamber in the upper part, from where it is subsequently led into the pipeline. There are no changes in terms of helium flow and the arrangement shown in Figure 2 remains.

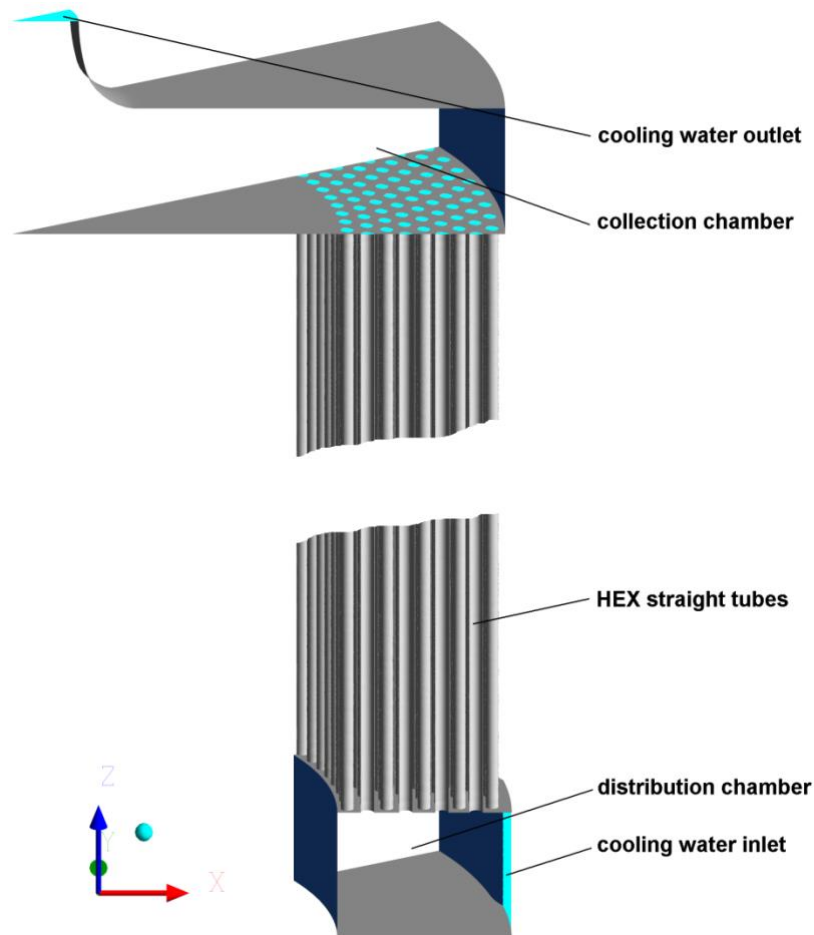


Figure 9 Detail of the straights tubes bundle (1/12 geometry)

## 4 COMPUTATIONAL DOMAIN

The preparation of the computational domain reflects two gradual goals. The first is the creation of a so-called Test Model, which is to perform a computational study on a separate hot leg of the DHR loop including the actual heat exchanger. In the second step, the entire geometry of the DHR loop, i.e. including the cold leg, has already been modelled (the so-called Complex Model). A description of the preparation of both models is given in the following subsections. For both models, a semi-symmetry along the height of the DHR loop (X-Z plane) is used.

### 4.1 TEST MODEL

The Test Model includes a hot leg of the loop and a DHR exchanger, see Figure 10. The geometry consists of a hot leg pipe that exits into a distribution chamber from where the supplied helium is radially distributed to the top of the exchanger. The hot leg piping is simulated including a layer of insulation and a steel wall. In a real loop, these two layers separate the cold leg pipe, which is placed concentrically around the insulated hot leg pipe.

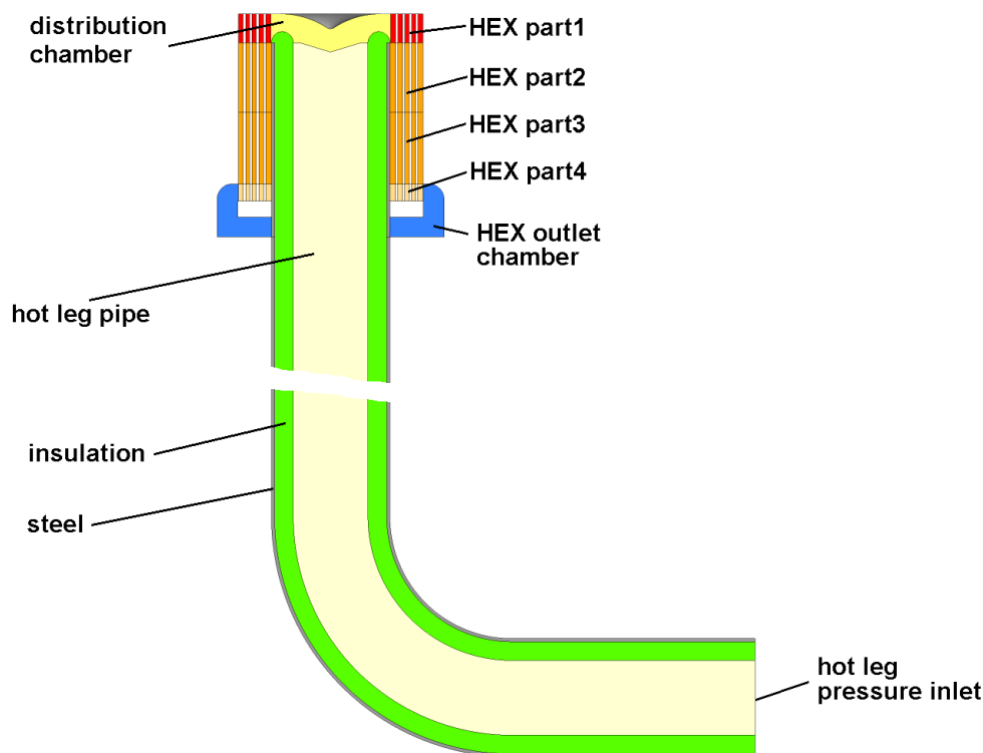


Figure 10: Simulated geometry of hot leg of DHR system

The simulated geometry of the hot leg also includes the own heat exchanger and the outlet chamber below the heat exchanger. In the real loop geometry, the bottom of the chamber, consisting of a 9 mm thick steel plate, as the baffle that separates the hot leg from the cold leg. At the bottom of the chamber there are flaps that form part of the bottom and which open when the system is activated. When opened, the hot and cold legs of the loop are



connected and helium is gradually circulated through the water-cooled tubular heat exchanger.

The heat exchanger itself is divided into four parts in the simulation. The reason for this division is to allow more detailed monitoring of temperature, enthalpy, density and other helium parameters during the calculation. Part one (HEX part1 - hereafter referred to as HEX1) is located in the upper part of the exchanger and the flow here is largely influenced by the helium inflow from the distribution chamber. Here the flow around the exchanger tubes changes from transverse to longitudinal. In terms of heat load, this is the most exposed part of the entire exchanger. Part four (HEX part4 - hereafter HEX4) is located at the bottom of the heat exchanger and the flow here is influenced by the helium outflow to the outlet chamber below the heat exchanger. Here the flow pattern changes from longitudinal to transverse. Parts two and three (HEX part2+3 - hereafter referred to as HEX2+3) then represent the remainder of the heat exchanger where the character of the pipe flow is close to longitudinal.

The actual arrangement of the tubes in the heat exchanger can be seen in Figure 11, which shows the geometry of the lower tube plate. It can be seen that the tubes are arranged in nine concentric rows in the exchanger model, with 45 straight vertical tubes in each row. The cooled helium is supplied from a distribution chamber located on the inside of the exchanger at the top of the exchanger. From the bottom of the exchanger, the helium then flows outwards to the outlet chamber of the exchanger.

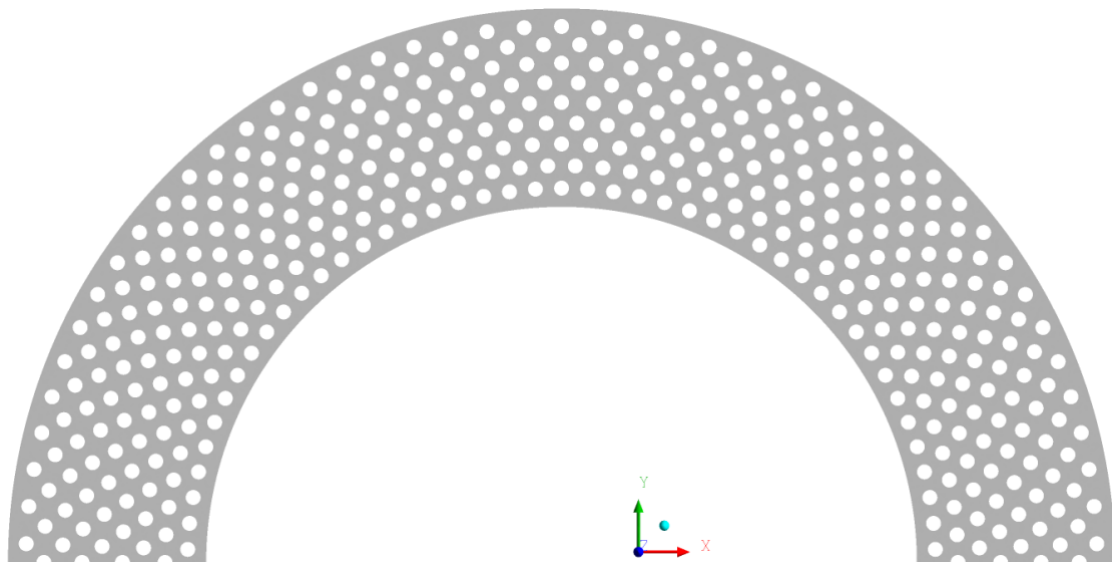


Figure 11: Geometry of bottom tube plate

## 4.2 COMPLEX MODEL

The domain of the Complex Model is based on the domain of the Test Model and is extended by two parts - the internal volume of the heat transfer tubes and the cold leg of the loop.

#### 4.2.1 GEOMETRY OF THE INTERNAL VOLUME OF THE HEAT EXCHANGER TUBES

Based on the results of the simulations performed on the Test Model (see Chapter 7), it was necessary to substantially refine the simulation of the heat transfer into the heat transfer tube bundle. For this purpose, the internal volume of the tubes with simulated cooling water was included in the solved geometry as part of the development of the comprehensive model, see Figure 12.

Since the problem is solved in half symmetry, 9 x 45 internal tube volumes were added to the model.

To reduce the computational complexity, the heat transfer tubes were simulated in a simplified way using a zero-thickness wall (the so-called thin wall function). Thus, a wall thickness of  $1.5\text{ mm}$  is simulated only mathematically using the known material properties of the pipe walls. This simplification ensured a saving of cells in the computational mesh for the simulation of transients in the order of higher units of millions.

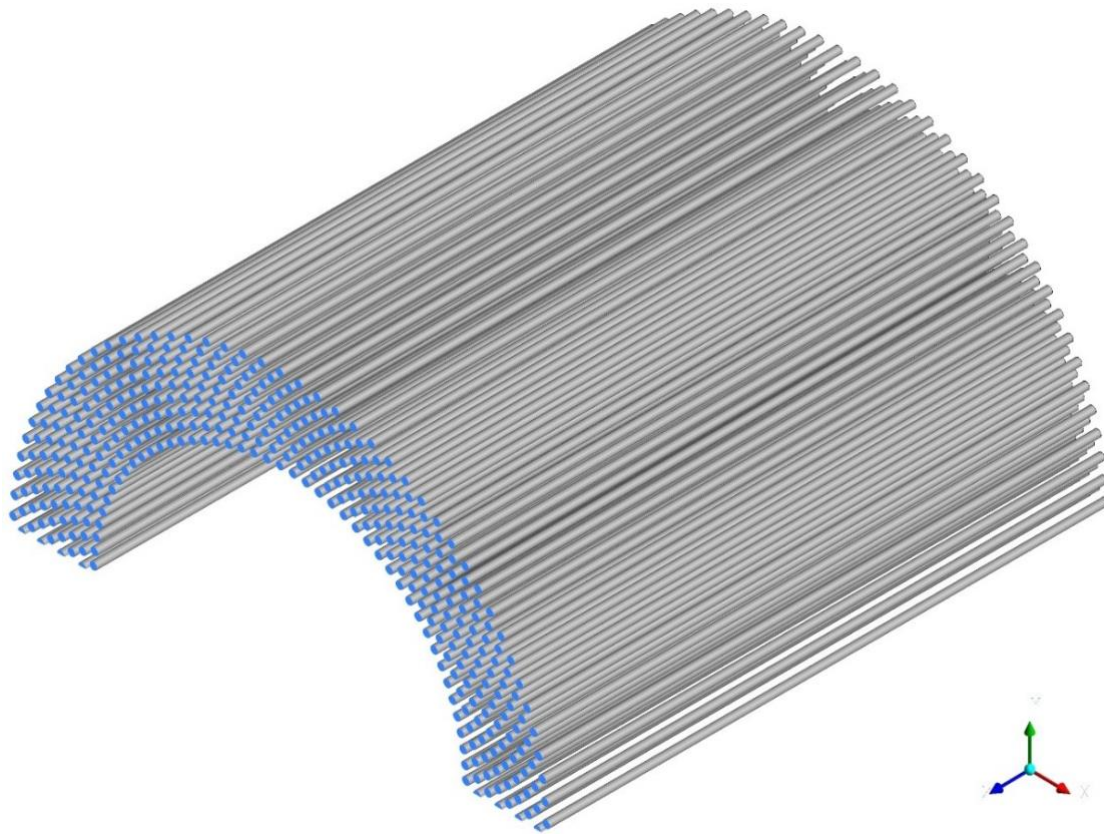


Figure 12: Geometry of HEX tube bundle

#### 4.2.2 COLD LEG GEOMETRY

The complete simulated loop geometry of the residual heat removal system that was used for the Complex Model can be seen in Figure 13. The hot leg geometry is based on the initial study, with the addition of a section simulating the cold leg. This section consists of the cold leg pipe itself and a chamber located below the aforementioned steel baffle that

separates the cold leg and the heat exchanger outlet chamber. Considering the relatively high computational complexity of the whole model, the geometry of the chamber located under the steel baffle has been simplified and the chamber is modelled as a free space with no internal build-up.

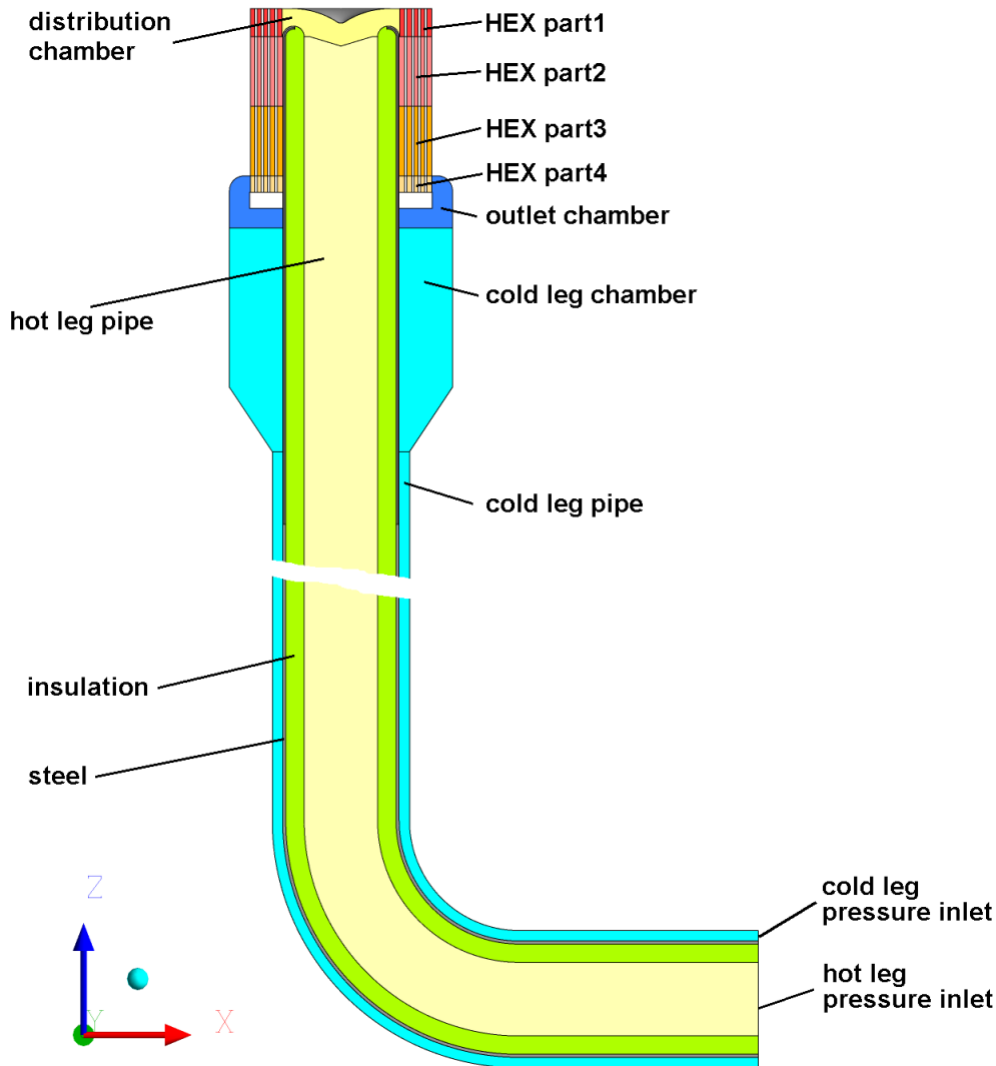


Figure 13: Simulated geometry of hot leg and cold of DHR system

The steel partition, which is in reality *9 mm* thick, is modelled with zero thickness, including the opening part. The external insulation of the cold leg, which is in reality *110 mm* thick, is modelled in the same way. The heat transfer is then simulated using a numerical function.

## 5 COMPUTATIONAL MESH

For the creation of the computational mesh, an approach with maximum use of hexahedral cells was chosen. This type of computational meshes is usually characterized by good behavior in terms of numerical stability and convergence of the computation, as well as favorable parameters in terms of accuracy of the obtained data. Only in places where the use of hexahedral cells would lead to a deterioration of the mesh quality, the use of wedge pentahedral cells is assumed. The quality of a computational mesh of this type was evaluated using two basic parameters, namely *skewness* and *aspect ratio* [1].

Furthermore, the focus was placed on optimizing the number of cells in each part of the models. The size of the model is crucial in the case of simulating longer transients in terms of computational time.

The following subsections separate the mesh generation for both models. The first subchapter describes the hot leg and DHR exchanger generation within the Test Model, the second subchapter describes the computational mesh generation for the Complex Model, i.e., it includes changes from the Test Model for the hot leg and DHR exchanger region, and then the cold leg mesh generation is described. Both subchapters include a summary of the quality of the generated mesh.

### 5.1 TEST MODEL

#### 5.1.1 HOT LEG AND HEAT EXCHANGER

Figure 14 shows the surface computational mesh on the plane of symmetry and on the cross section at the bottom of the hot leg. The figure shows that the computational mesh in this part of the simulated geometry consists only of hexahedral cells. In the steel and in the insulating layer it is a structured mesh. Inside the pipe, it is a combination of structured and unstructured mesh.

The structured mesh was used in the outer part of the pipeline, as this type of mesh can be very efficiently controlled in terms of its arrangement and cell sizes. In the inner part, an unstructured mesh is used. Its use is determined by the geometry of the upper wall of the distribution chamber, see Figure 15, where a structured mesh would not be possible or would lead to a significant deterioration in its quality in terms of *skewness*.

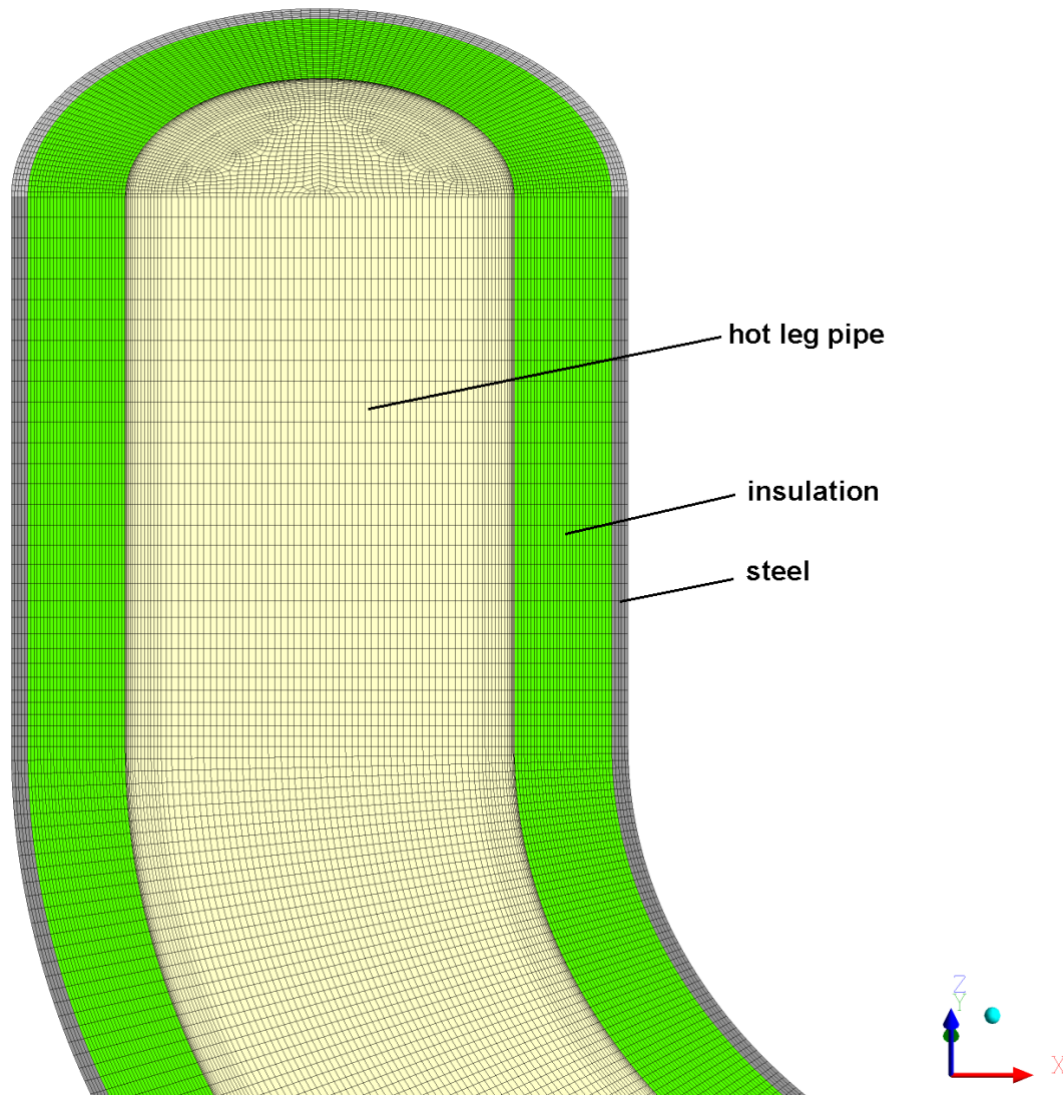


Figure 14: Surface and cross-sectional mesh at down part of a hot leg inlet pipe

In the case of the distribution chamber, a mesh with hexa- and wedge pentahedral cells was used. Figure 15 shows that the mesh with wedge pentahedral cells was used to reduce the mesh density in the circumferential direction between the heat exchanger body and the hot leg inlet pipe, where too high mesh density would have resulted in significantly increased computational requirements.



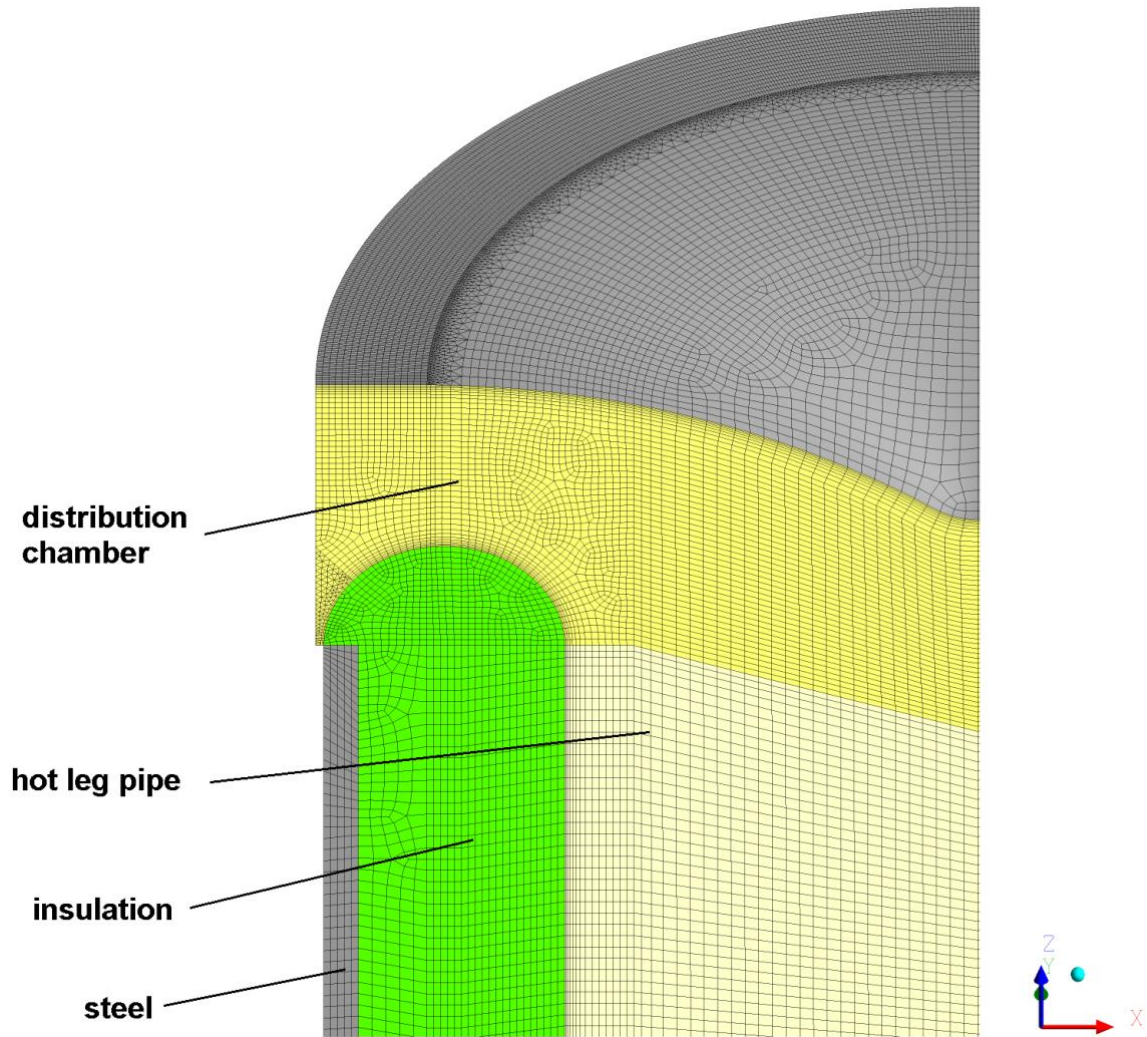


Figure 15: Surface mesh at top part of a hot leg inlet pipe and distribution chamber

In order to maintain the high quality of the mesh, pentahedral wedge-shaped cells were also suitably used in the narrowing part of the distribution chamber between the heat exchanger body and the dividing wall. Both of these cases of the use of pentahedral cells are shown in detail in Figure 16 and Figure 17. Figure 16 shows a detail of the mesh layout at the interface of the distribution chamber and the upper part of the exchanger and Figure 17 shows a detail of the mesh in cross-section at the level of the start of the second part of the heat exchanger.

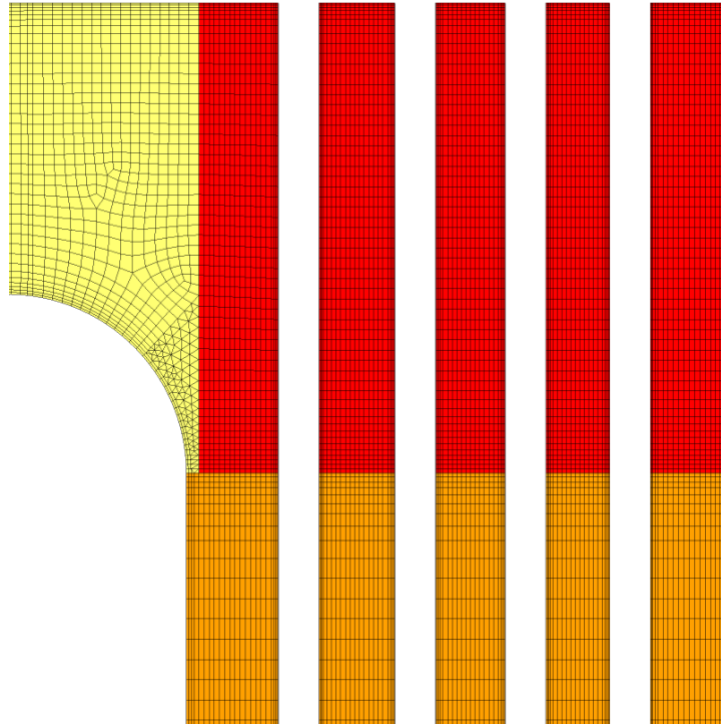


Figure 16: Symmetry plane mesh in a top part of HEX and in distribution chamber

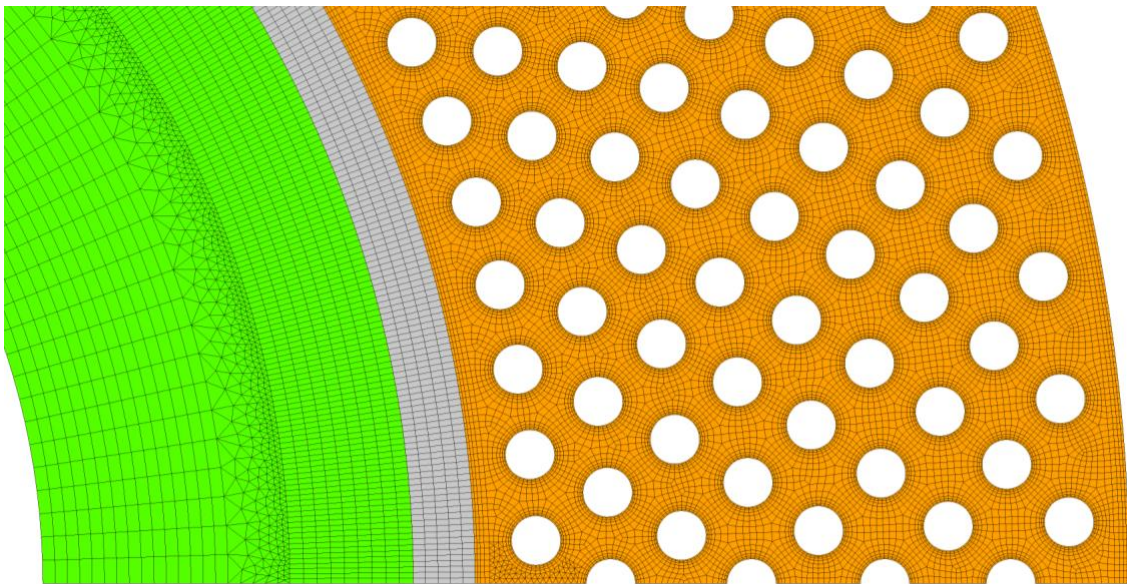


Figure 17: Cross-sectional mesh in HEX part 2, steel and insulation

Figure 18 shows the arrangement of the surface mesh in the space of the lower part of the heat exchanger, i.e., the lower tube plate, the lower part of the heat exchanger tubes, part of the outer wall and in the location of the coolant outlet from the heat exchanger to the outlet chamber. In the vertical direction, there is a noticeable increase in the density of the mesh in the boundary layer above the lower tube plate and further at the level of the heat exchanger outlet. This is the area where the longitudinal flow changes to transverse flow.



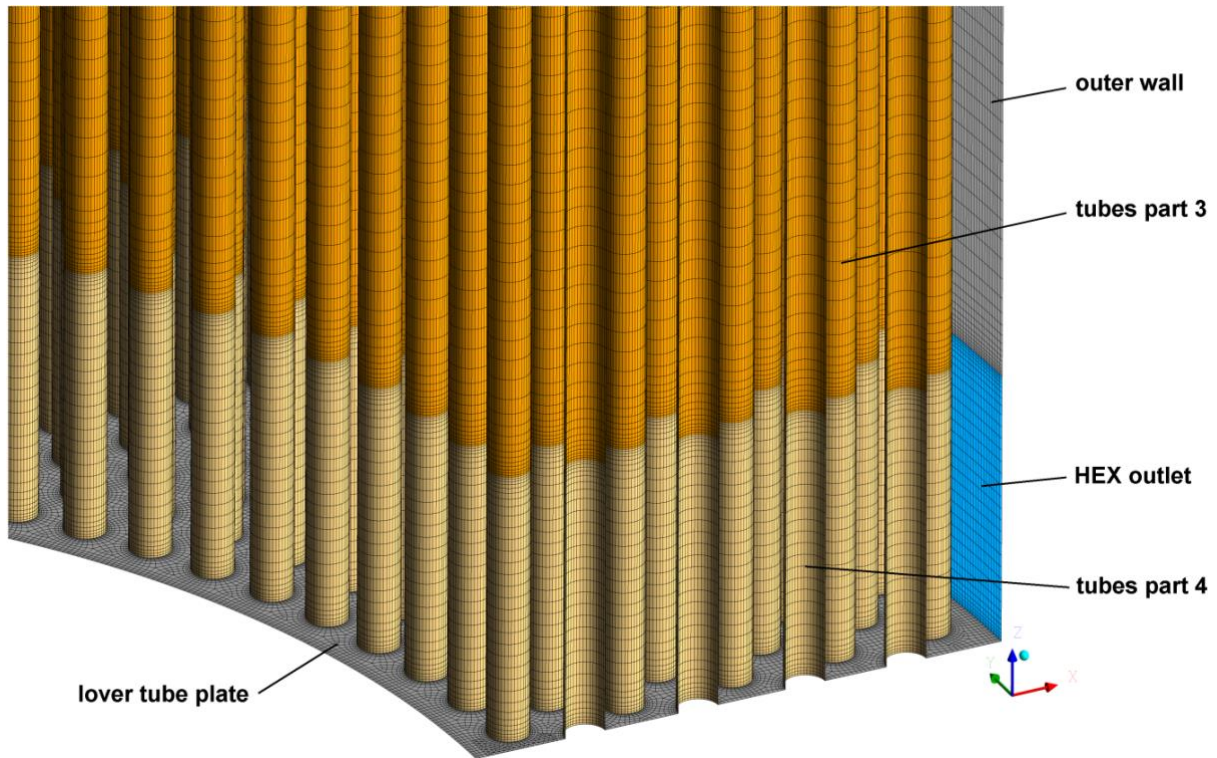


Figure 18: Surface mesh on lower tube plate and HEX tubes

The increase in the density of the mesh in the boundary layer close to the wall can also be clearly seen in Figure 19, which shows its arrangement in the plane of symmetry, in the area of the lower part of the heat exchanger and the outlet chamber.

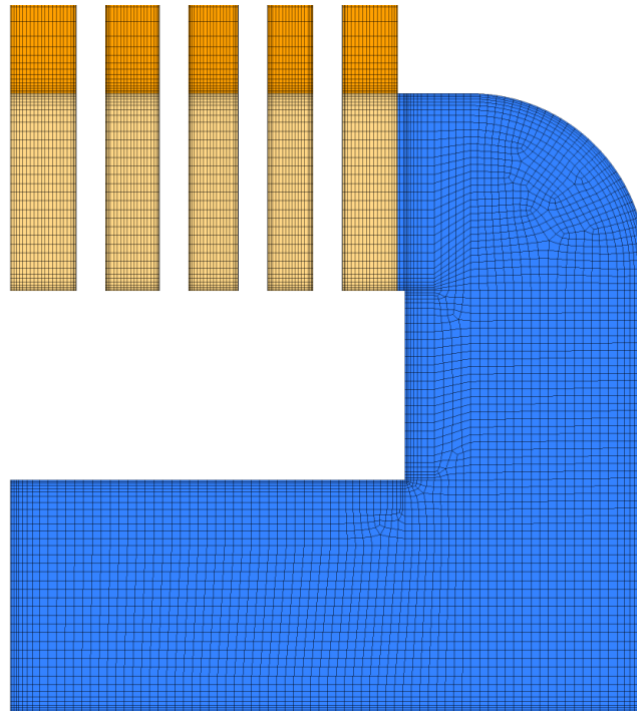


Figure 19: Symmetry plane mesh in a bottom part of HEX and in outlet chamber



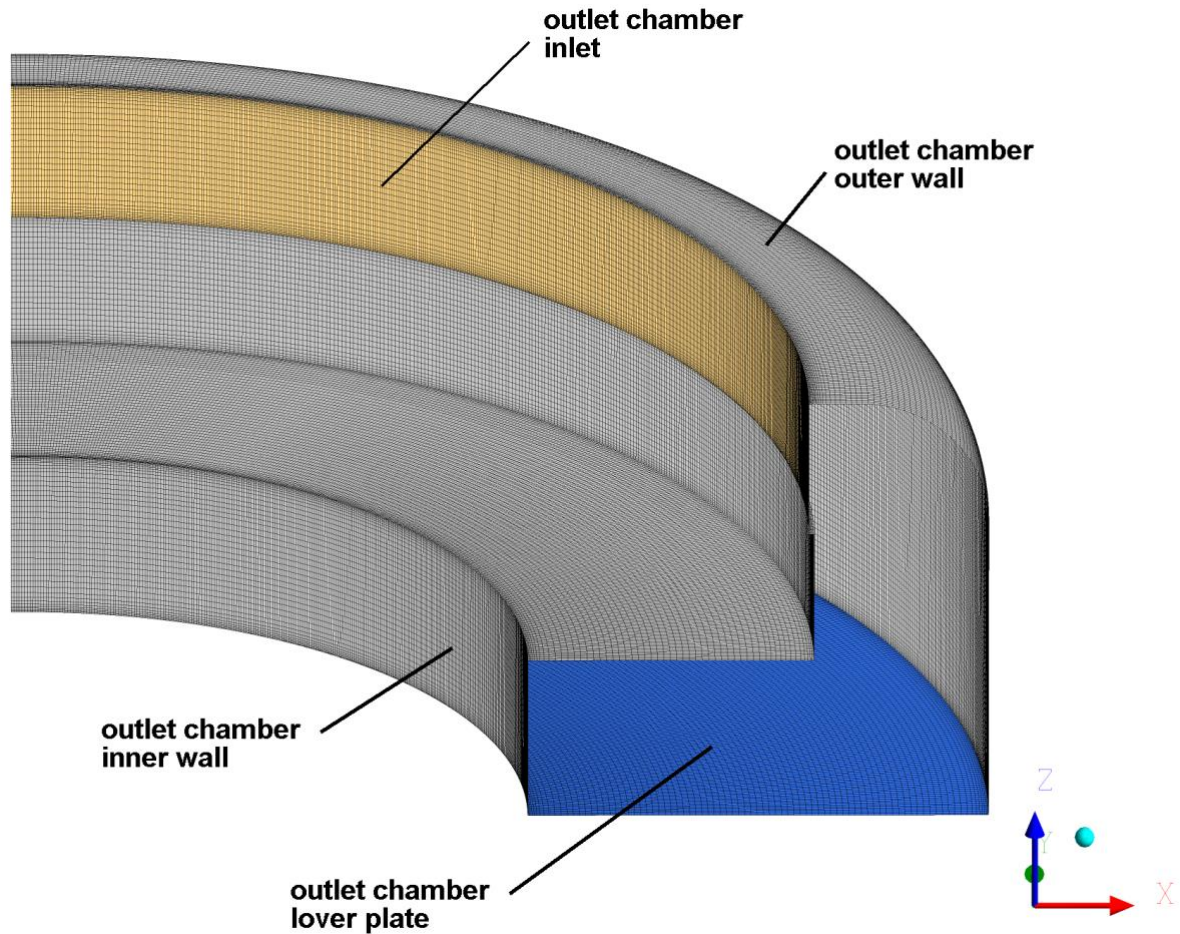


Figure 20: Surface mesh on outlet chamber wall and inlet

In Figure 20, which shows the computational mesh on the surface of the outlet chamber, it can be seen that only hexahedral cells were used throughout the outlet chamber. It can also be seen that wherever possible in terms of geometry, the use of a structured mesh was preferred.

### 5.1.2 COMPUTATIONAL MESH QUALITY

The graph in Figure 21 shows the frequency distribution of cells as a function of the *skewness* parameter. Here, the highest level of *skewness* is below 0.69 and even below 0.62 in the case of fluid zones. These values can be considered very favorable. Moreover, in the case of fluid zones, more than 97.5 % of the cells have a skew value less than 0.25. On the other hand, only 0.02 % of the cells exceed the value of 0.50. In the case of solid zones (insulation and steel), a total of 89 % of the cells have a skew of less than 0.25 and only 1.5 % of the cells exceed 0.50.

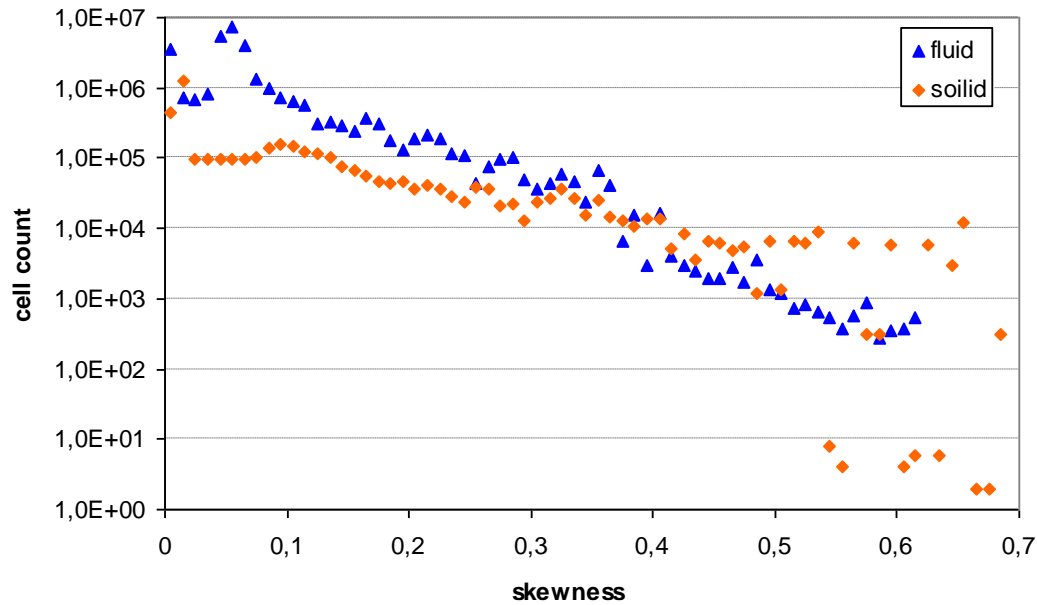


Figure 21: *Skewness* cells distribution in computational mesh

In the case of the *aspect ratio* parameter, whose distribution is shown in the graph in Figure 22, the situation is reversed. In solid zones, the maximum value of *aspect ratio* is only around 9. In fluid zones, approximately 82 % of the cells have an *aspect ratio* value less than 10. Subsequently, the value of 20 is exceeded by 0.25 % of the cells located in the vertical part of the hot leg pipe, in the boundary layer near the insulation wall surface. In the pipe heat exchanger area, the maximum *aspect ratio* value is around 20 and again these are cells located in the boundary layer near the surface of the heat exchanger tubes. These cells can be seen, for example, Figure 17 and Figure 18.

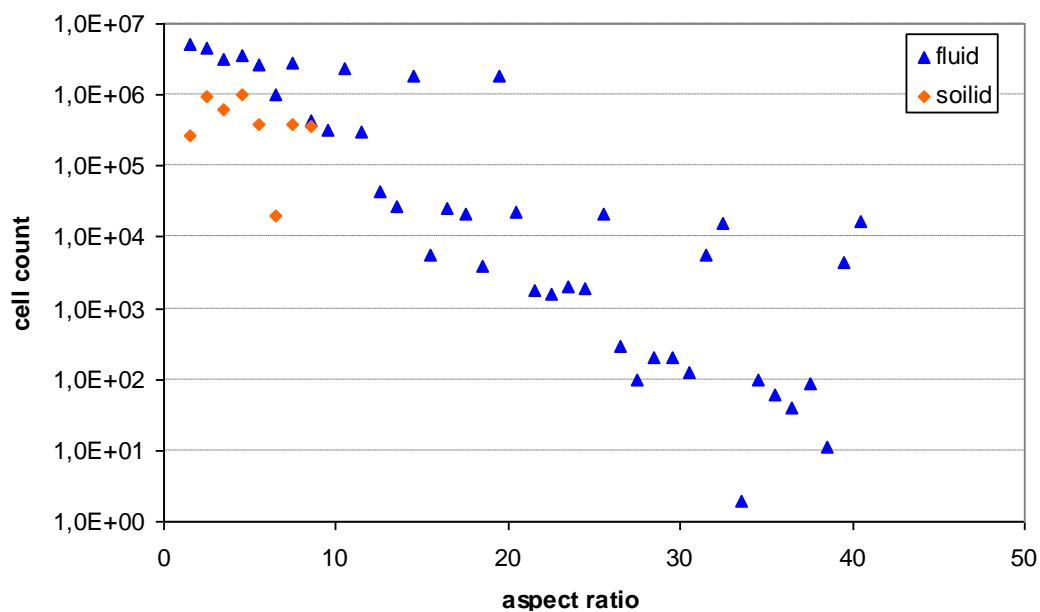


Figure 22: *Aspect ratio* cells distribution in computational mesh

## 5.2 COMPLEX MODEL

### 5.2.1 CHANGES FOR HOT LEG AND HEAT EXCHANGER

On the basis of the test calculations (see chapter 7), selected adjustments were made in the mesh design. These include the steel wall and insulation space, the steel baffle space and the inclusion of a fluid zone simulating heat dissipation by the refrigerant flowing in heat exchanger tubes.

#### 5.2.1.1 Space of steel wall and insulation

In Figure 15 it can be seen that the mesh in the space near the steel wall was originally designed as conformal, i.e. continuous. However, this approach led to too high density of the mesh in the steel wall of the hot leg supply pipe and in the adjacent insulation where only heat transfer through the line takes place. Therefore, a new interface function was used to connect the non-conformal mesh. The Interface function was placed in the middle of the thickness of the solid zone simulating the steel wall.

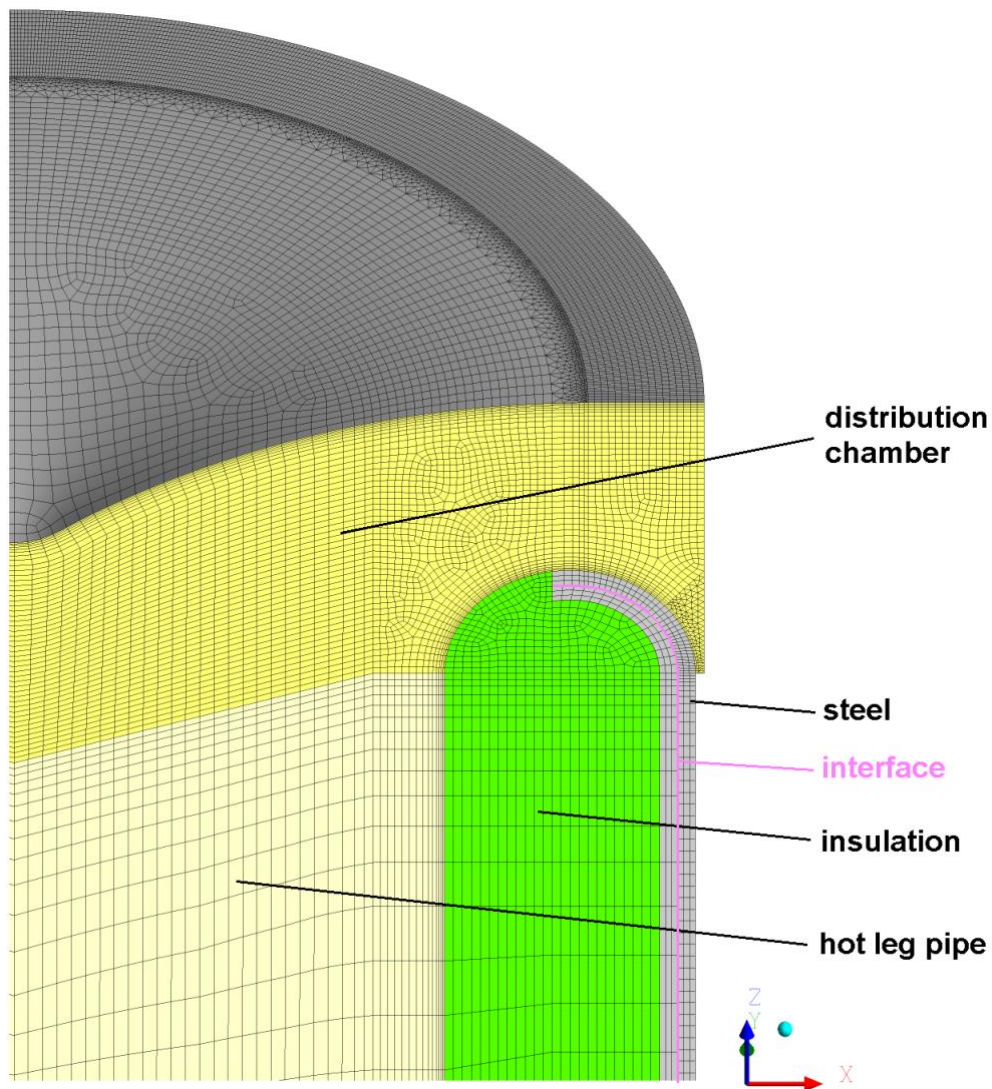


Figure 23: Surface mesh at top part of a hot leg inlet pipe and distribution chamber

From Figure 23, it can be seen that this approach allowed a significant reduction in the density of the computational mesh, both in the longitudinal axis direction and in the circumferential direction. The reduction in density was reflected in the steel wall section and in the insulation as well as in the upper part of the hot leg feed pipe. In total, this saved approximately two million cells in the solid zones of the steel and insulation, and half a million cells in the fluid zone of the hot leg inlet pipe.

#### 5.2.1.2 Space of steel baffle

Figure 24 shows the computational mesh on the plane of symmetry around the steel baffle separating the hot and cold legs at the location of the heat exchanger outlet chamber and the cold leg distribution chamber. Where the baffle contains flaps to ensure the passage of helium from the hot to the cold leg in the event of an emergency, a densifying of the mesh in the radial direction can be seen where the edges of these flaps are located.

Furthermore, the use of an interface function in the middle of the steel wall of the hot leg supply pipe is also evident, which allows the density of the computational mesh to be adjusted independently on both sides, thus reducing the overall computational complexity of the Complex Model.

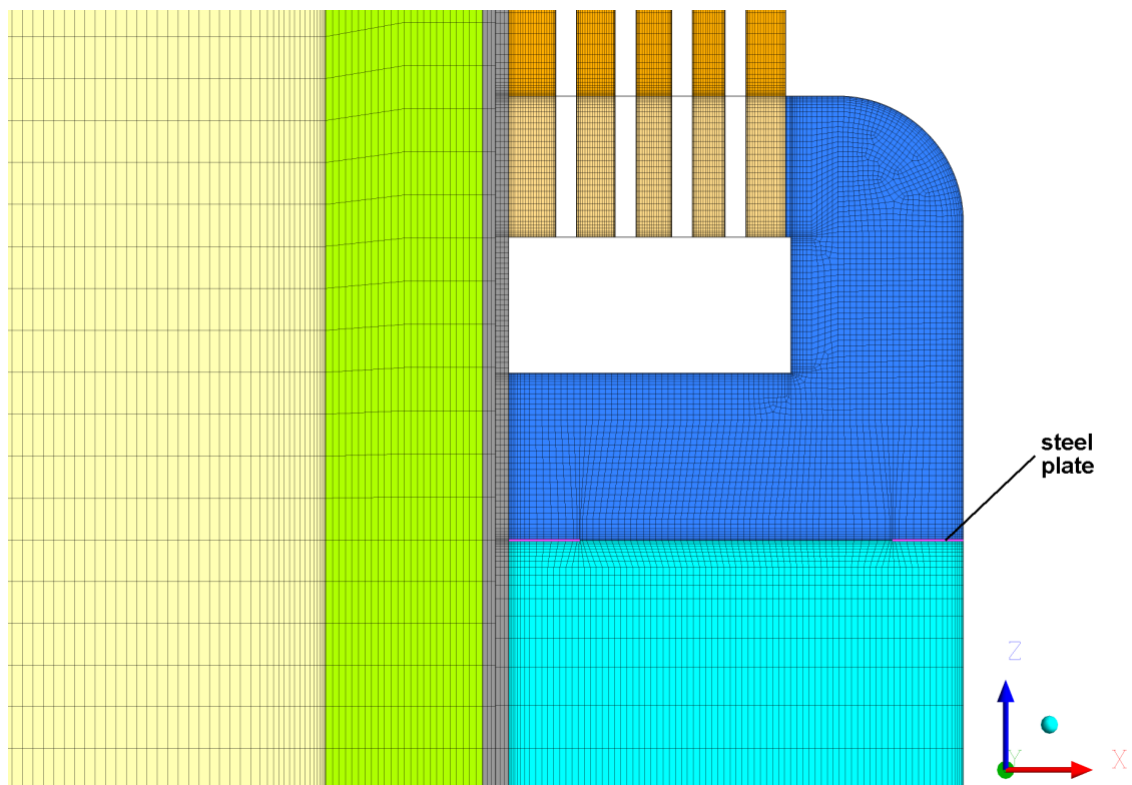


Figure 24: Symmetry plane mesh in a bottom part of HEX in outlet chamber and in cold leg chamber

#### 5.2.1.3 Intertubular area

As mentioned in the section "tube bundle geometry", for the purpose of the Complex Model it was necessary to create a volume including the flowing coolant. Figure 25 shows



the lower tube plate together with the computational mesh at the inlet to the heat exchanger tubes. The mesh inside the tubes was modelled using cells in the shape of triangular or quadrilateral prisms. The type of mesh is dictated by the number of cells that are located on the perimeter of the tube, i.e. on the fluid side of the helium zone.

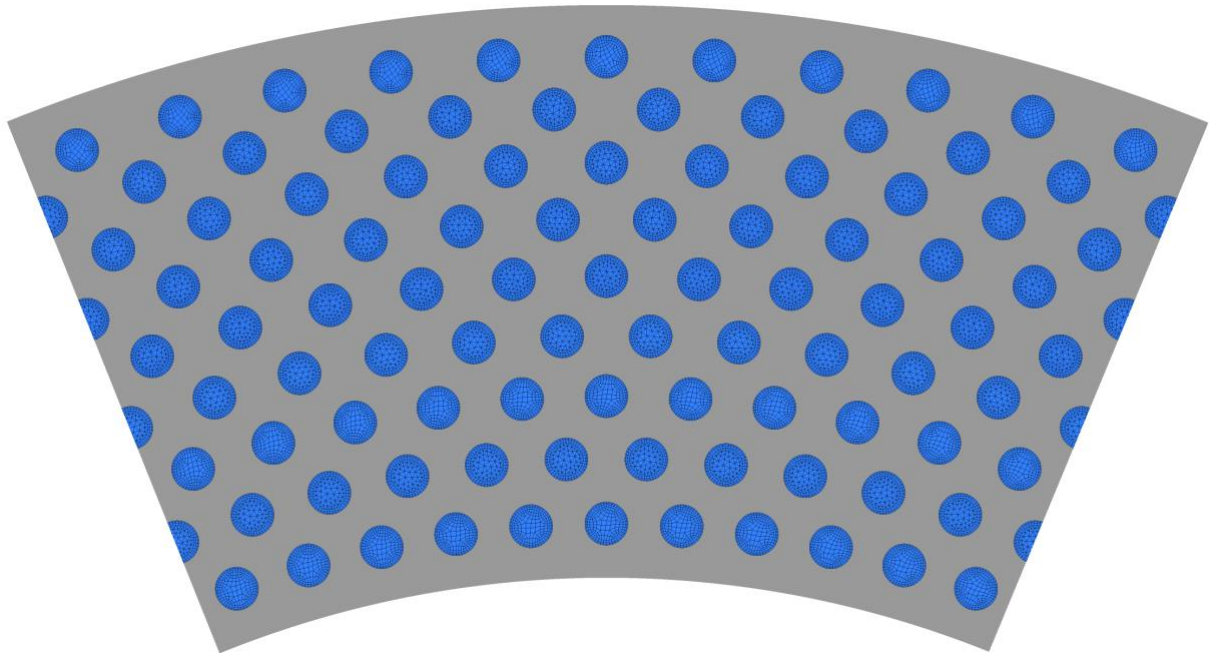


Figure 25: Lower tube plate and tube inlet surface mesh

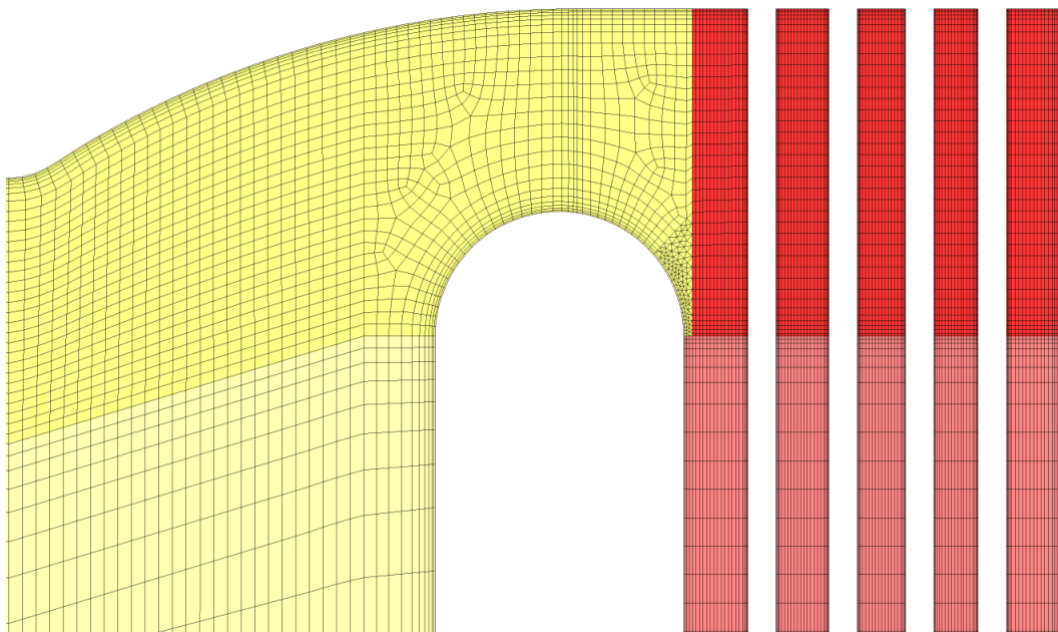


Figure 26: Symmetry plane mesh in a top part of HEX and in distribution chamber

The active part of the heat exchanger in connection with the intertube space is the most demanding area in terms of the number of cells. Thus, to maintain a reasonable size of the computational mesh, the increase in the number of cells was minimized by reducing the mesh density along the height of the exchanger. Thus, a reduction of approximately half the number of cells was achieved in the HEX2+3 parts, and a reduction of 30 to 40 % in the inlet and outlet part. The new mesh arrangement in the exchanger area can be seen in Figure 26 and Figure 27.

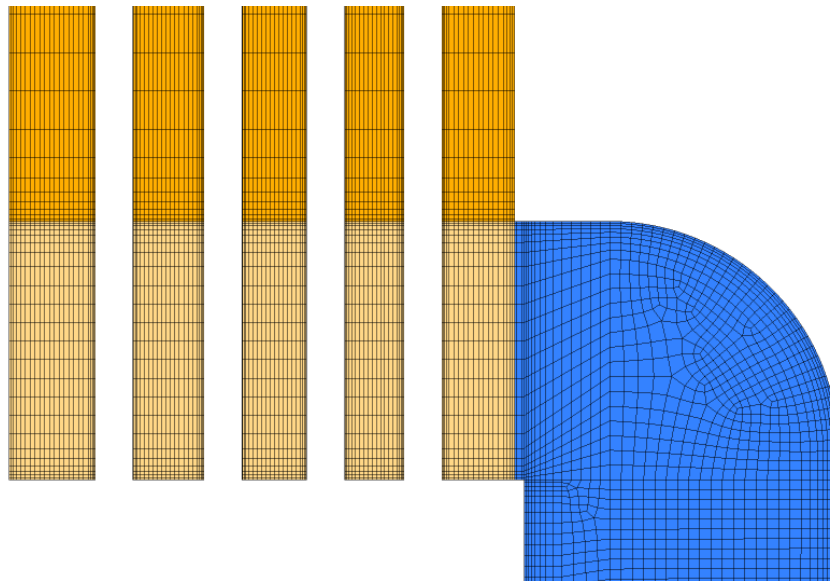


Figure 27: Symmetry plane mesh in a bottom part of HEX and in outlet chamber

The saving in the number of cells achieved by this modification in the intertube space was able to practically compensate for the increase in the number of cells due to the formation of fluid zones of the coolant, i.e. the interior of the heat transfer tubes. This resulted in an increase of only 1.1 million cells.

### 5.2.2 COLD LEG

Figure 28 shows the surface mesh in the space of the cold leg distribution chamber. In the figure the flaps in the bottom of the heat exchanger outlet chamber, are color coded and marked. In the figure also it can be seen that the computational mesh is slightly densified around the opening part of the bottom not only in the axial direction but also in the radial and circumferential direction. Hexahedral cells were again used throughout the cold leg area.

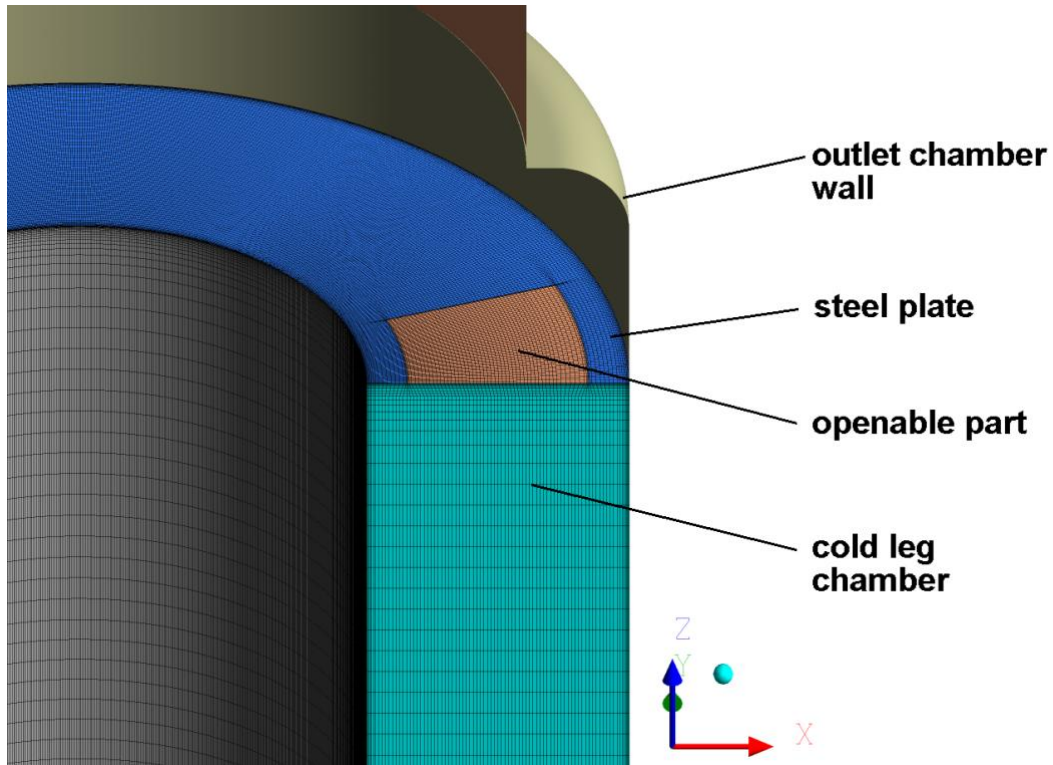


Figure 28: Surface mesh at cold leg distribution chamber

Figure 29 shows the surface mesh in the lower part of the distribution chamber and the upper part of the cold leg pipe, which is of inter-circuit cross section. The use of pentahedral wedge cells oriented in the radial direction is evident below the conical portion of the interpipe space. This has allowed subsequent connection to the already generated hot leg computational mesh without the need for further use of non-conformal networks and hence interface function.

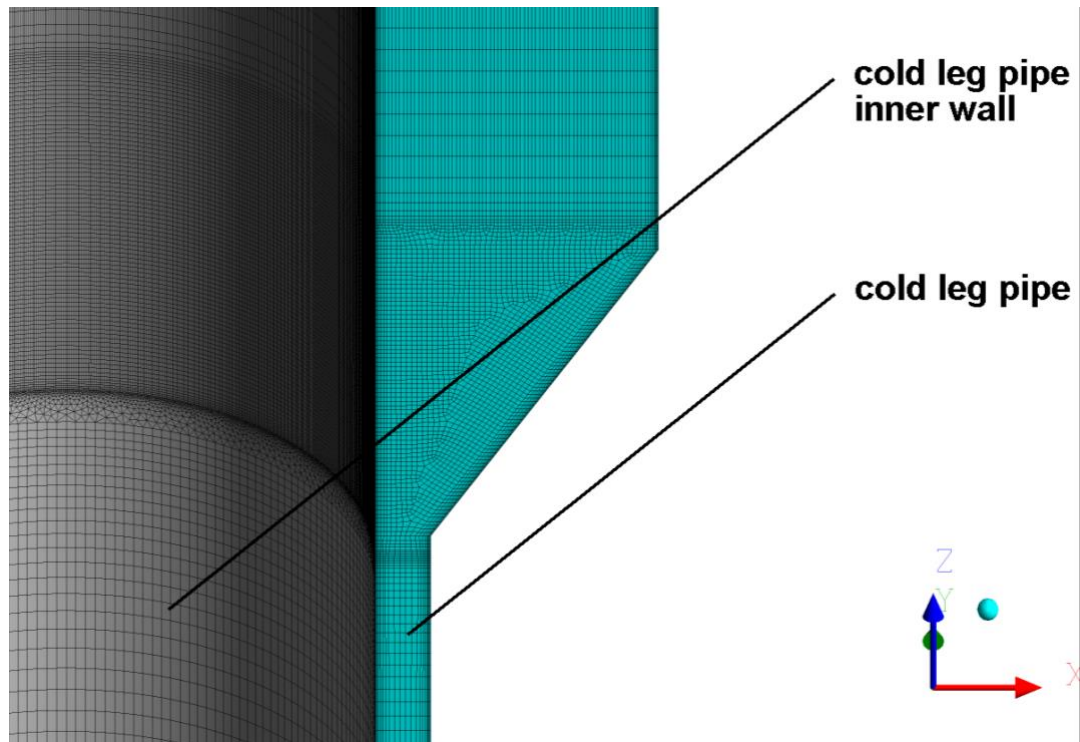


Figure 29: Surface mesh at cold leg distribution chamber and cold leg pipe

### 5.2.3 COMPUTATIONAL MESH QUALITY

Similar to the hot leg simulation itself (Test Model), the quality of the computational mesh was evaluated using the *skewness* and *aspect ratio* parameters for the Complex Model.

Careful adjustments made to the hot leg and heat exchanger and the addition of the cold leg computational network had a positive effect on the quality of the computational mesh for the entire Complex Model.

The maximum *skewness* in the fluid zones, which exceeded 0.62 in the previous model, has been reduced so that the maximum *skewness* currently exceeds 0.52. The 0.50 level is then exceeded by approximately 1400 cells, which represents approximately 0.004 % of the total. Similarly, in the solid zones, the maximum *skewness* has been reduced from 0.595 to 0.525. These parameters can be considered very good with respect to the complexity of the simulated geometry. The overall distribution of cell *skewness* in the computational mesh is shown in graph in Figure 30.

In the case of the *aspect ratio* parameter, the distribution of which is shown in graph in Figure 31, the maximum value of the *aspect ratio* increased from 9 to 18 for the solid zones, with the most prolonged cells located in the steel pipe wall. This is due to the change in the mesh arrangement in the steel as a result of the application of the interface function. These changes are fully acceptable, especially since these are solid zones where only the simulation of heat transfer through the conduction occurs.

For the fluid zones, the maximum value is slightly increased from 41 to 44. There is also possible to see a significant increase in the number of cells that exceed the value of 20. This is an increase in the number of stretched cells that have newly appeared in the middle



part of the exchanger, where the length of the cells has practically doubled. Given that these are cells in the first and second row of the boundary layer on the surface of the heat exchanger tubes, the centers of which are only tenths of a millimeter from the walls, this should not have a negative effect on the numerical or physical nature of the simulations.

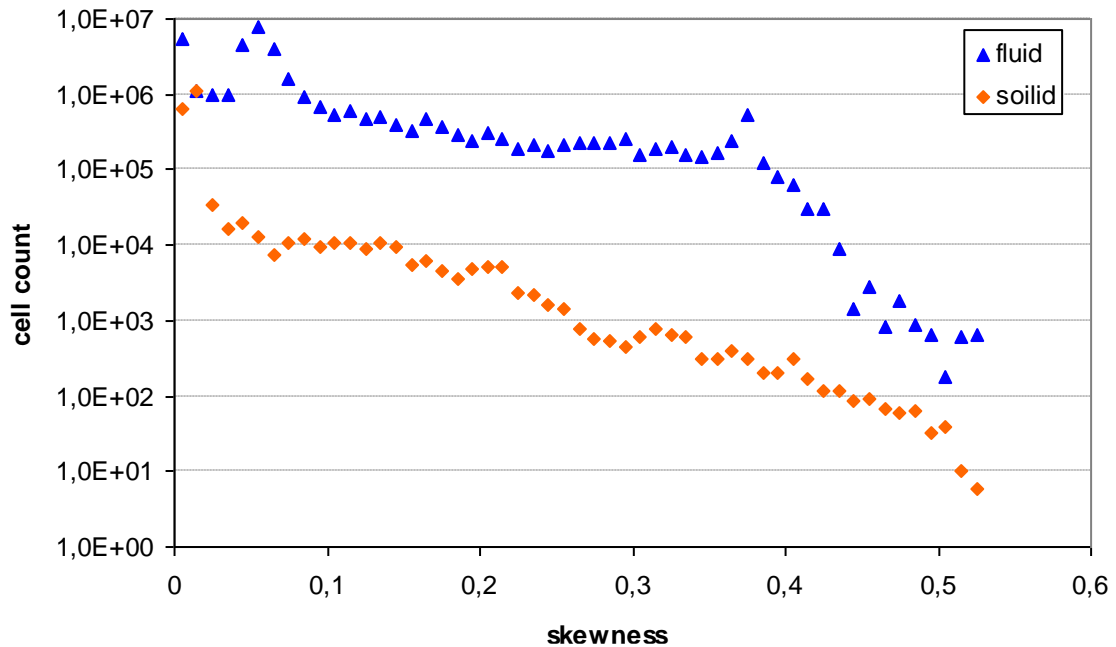


Figure 30: *Skewness* cells distribution in computational mesh

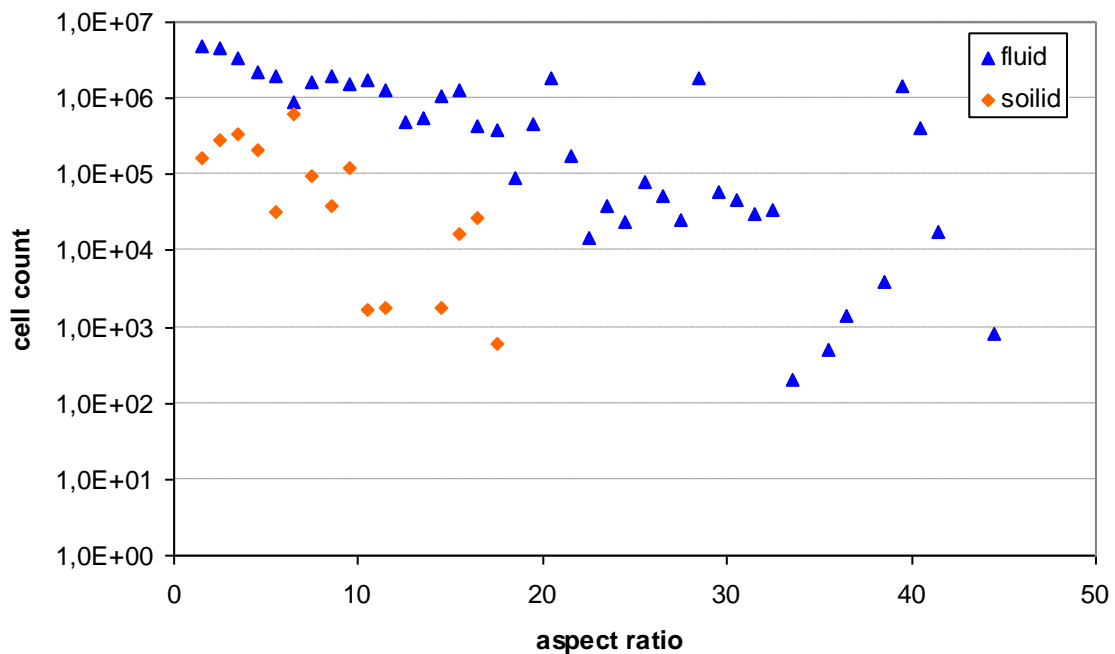


Figure 31: *Aspect ratio* cells distribution in computational mesh

## 6 NUMERICAL MODEL DEFINITIONS

### 6.1 SOLVER SETTINGS

Table 4 summarizes the settings of the basic parameters of the used model. The used definitions of the individual parameters of the numerical model are based on generally valid recommendations and on experience gained from the previously solved numerically similar problems.

**Table 4 Setting of the basic numerical parameters of the calculation**

Parameter	Setting	Note
Time dependence	Stationary simulation, transient simulation	In particular, non-stationary events according to predefined scenarios were solved. Stationary calculation was usually used for preliminary stabilization of parameters.
Solver	Pressure-based	The flow of both media is simulated as insufficient and the thermal-physical properties are dependent only on temperature.
Pressure-velocity coupling	SIMPLE, PISO	The scheme used depends on whether the stationary or non-stationary process was simulated and also on the behavior of the calculation.
Discretization schemes	Gradient – least squares cell based	
	Pressure – body force weighted	
	Others – second order upwind	
Turbulence model	$k$ - $\omega$ BSL (low Reynolds)	The $k$ - $\omega$ BSL model has a good ability to approximate a stationary solution, which can then be used as an initial state for a defined scenario.

### 6.2 SETTINGS OF THERMOPHYSICAL PROPERTIES OF USED MATERIALS

The following subchapter deals with the definition of the basic thermophysical properties (density, heat capacity, thermal conductivity and dynamic viscosity) for each material, i.e. helium, water, heat exchanger tube material and insulation. As in the previous calculations, a method referred to as piecewise linear, was used to define the material properties as a function of temperature. In this method, material properties are calculated by linear interpolation between two adjacent defined values. The advantage of this method is reliability and, with appropriate selection of individual points, very solid accuracy.

#### 6.2.1 HELIUM

The graphs in Figure 32 and Figure 33 show the temperature dependence of each helium property as defined in the calculation.

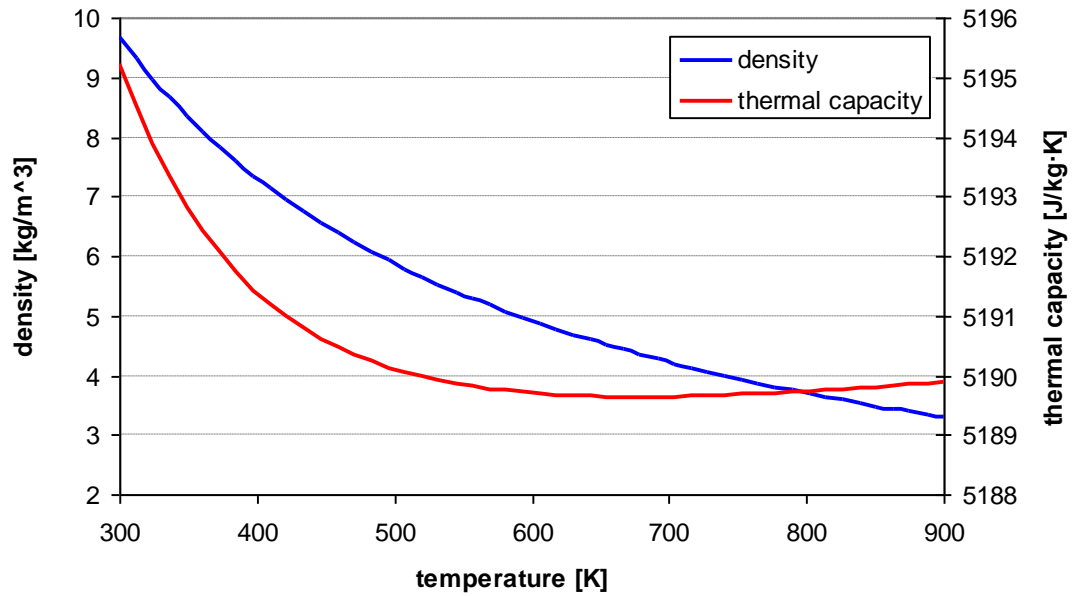


Figure 32: Helium density and thermal capacity

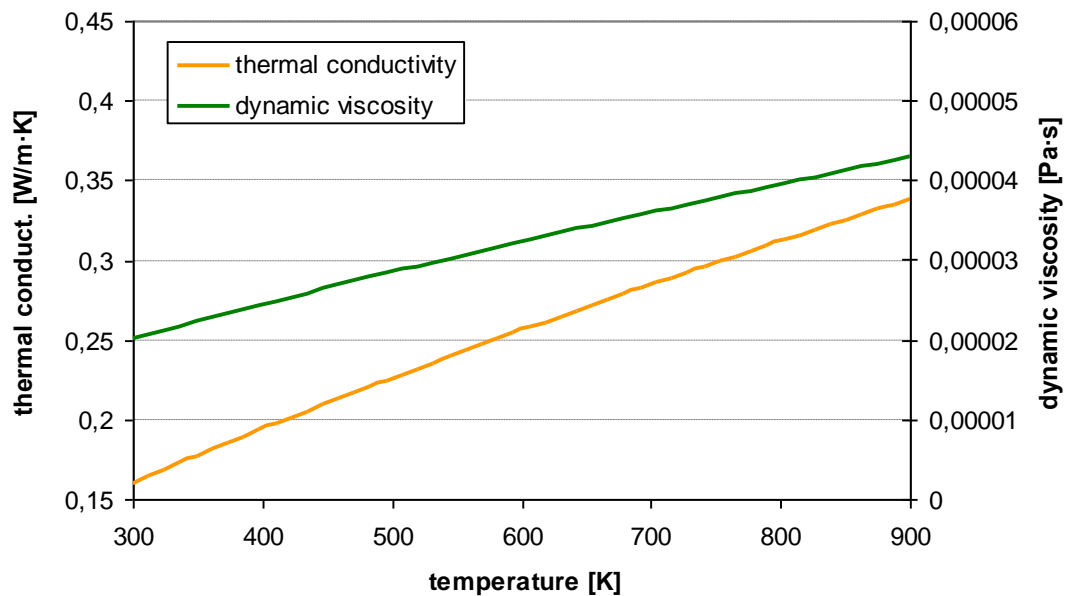


Figure 33: Helium thermal conductivity and dynamic viscosity

### 6.2.2 WATER

The graphs in Figure 34 and Figure 35 show the dependence of each water property on temperature as defined in the calculation.

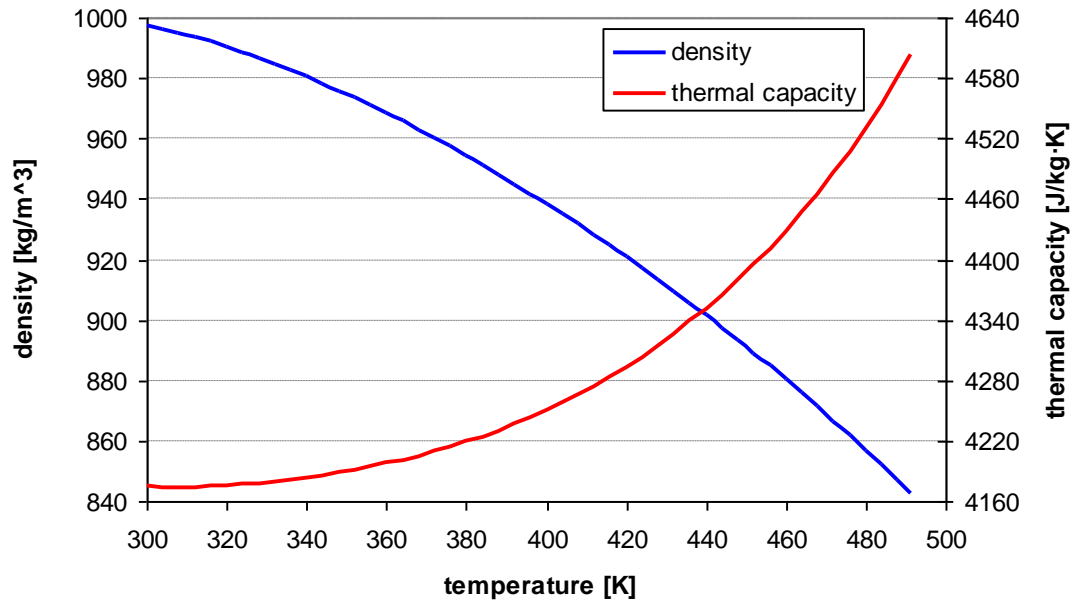


Figure 34: Water density and thermal capacity

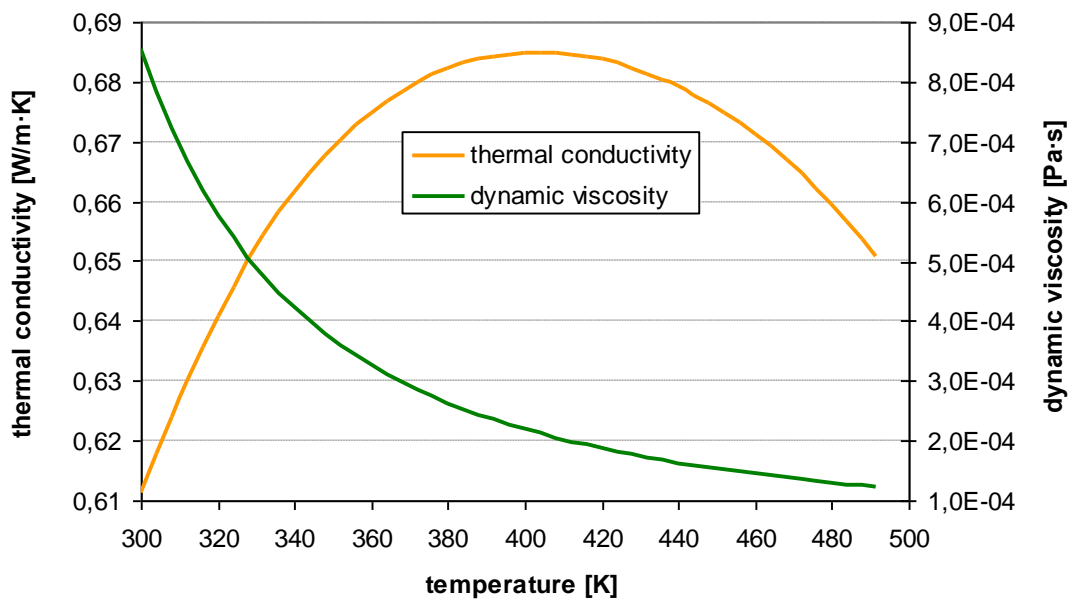


Figure 35: Water thermal conductivity and dynamic viscosity

### 6.2.3 MATERIAL OF HEAT EXCHANGER TUBES

For the purpose of the realized simulations, a constant density of the heat exchanger tube material was chosen, namely  $7665 \text{ kg/m}^3$ . In real conditions, the material density is of course temperature dependent due to thermal expansivity. However, the calculation does not consider the change in geometry due to thermal expansivity of the material and therefore the density can be defined as constant. In the case of heat capacity and thermal

conductivity, however, it is already necessary to consider the change in these properties as a function of temperature. The dependence of both properties on temperature is shown in the graph in Figure 36.

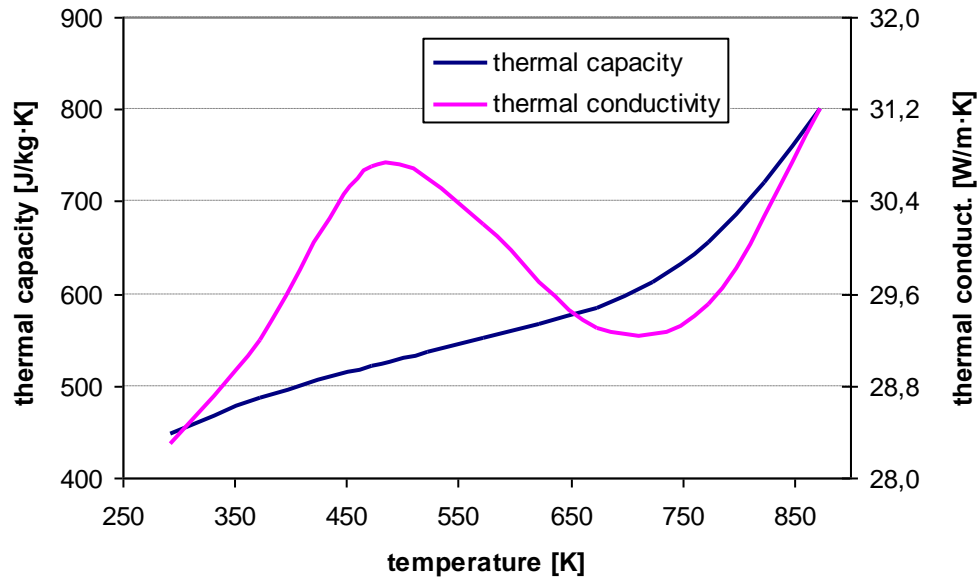


Figure 36: Steel thermal conductivity and thermal capacity

#### 6.2.4 INSULATION

For the purpose of the realized simulations, a constant density of the insulation material was chosen, namely  $160 \text{ kg/m}^3$ . As with steel, the expansivity of the material due to temperature changes and the associated density changes are not modelled here. Therefore, the density can be defined as constant. However, in the case of heat capacity and thermal conductivity, it is already necessary to consider the change in these properties as a function of temperature. The dependence of both properties on temperature is shown in the graph in Figure 37.

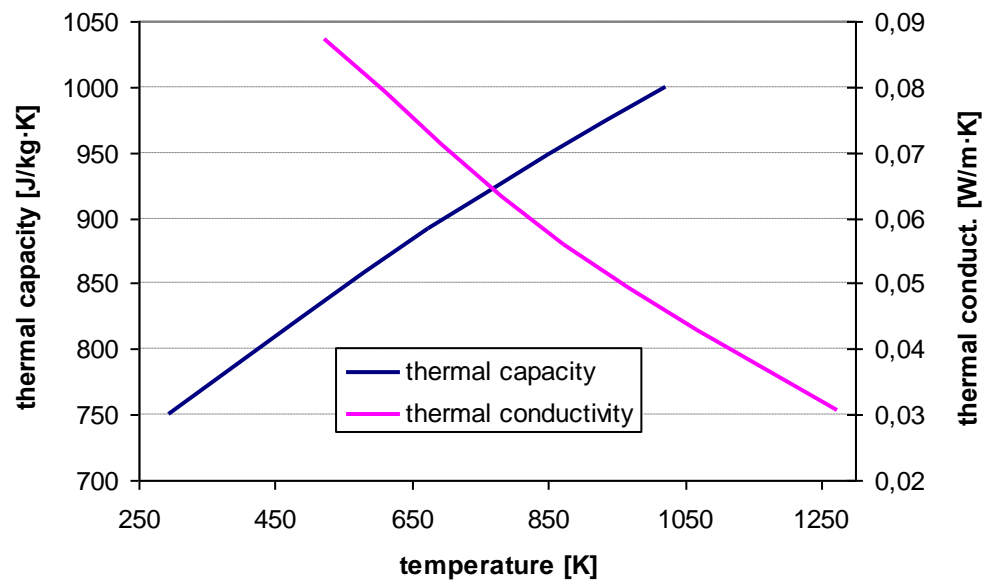


Figure 37: Insulation thermal conductivity and thermal capacity

## 7 TEST MODEL CALCULATIONS

The Test Model is used for a computational study of a separate hot leg of the DHR loop. The achieved results allowed subsequently to incorporate further suitable geometrical simplifications, to optimize the computational mesh and the boundary and initial conditions of the solved scenarios, or to find suitable numerical approaches to the solution. For the test calculations, boundary conditions are defined first, followed by a description of the results obtained.

### 7.1 BOUNDARY CONDITIONS

Table 5 summarizes the basic boundary condition settings for the simulated problem, which includes a helium inlet temperature of  $800\text{ K}$ , and a heat exchanger tubes wall temperature of  $323\text{ K}$ . Both values are constant throughout the calculation.

**Table 5 Setting of boundary conditions**

Location	Condition	Note
Helium inlet	Pressure inlet	Temperature $800\text{ K}$ . The pressure inlet condition allows to solve non-flow geometries, where one surface serves both as inlet and outlet.
Walls of heat exchange tubes	Wall (temperature)	Temperature $323\text{ K}$ .
The outer walls of the model	Wall (heat flux)	Adiabatic boundary condition (Heat flux = $0\text{ W/m}^2$ ).
Materials interfaces	Wall (coupled)	Coupled condition of contact surfaces at the interface of different materials allowing free heat transfer.

### 7.2 SOLUTION AND RESULTS

In the first phase, the calculation was designed as stationary. Its purpose was to obtain an approximate distribution of velocity and temperature, from which a non-stationary problem was then run with a duration of  $100\text{ s}$ . The aim of this calculation was to evaluate the helium circulation in the solved region and to evaluate the evolution of selected physical parameters (temperature, power dissipation, mass fluxes, etc.). The time profiles of the maximum and mean temperatures in the different parts of the exchanger are shown in Figure 38.

The division of the heat exchanger into parts HEX1, HEX2+3 and HEX4 allows to monitor these parts separately. From the graph it is clear that the active area of the exchanger extends only to the upper part (HEX1), where the hotter helium from the distribution chamber flows. The remaining parts of the exchanger are almost entirely filled with helium, the temperature of which is close to the temperature at the surface of the heat exchanger tubes ( $323\text{ K}$ ).

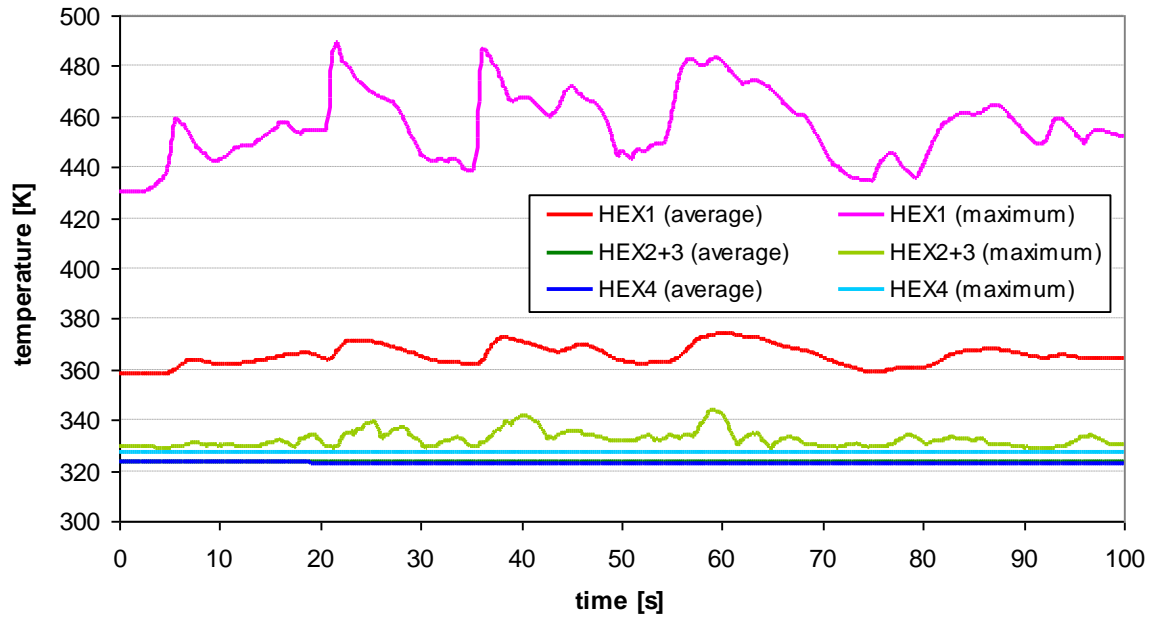


Figure 38: Time temperature profiles in individual parts of the heat exchanger

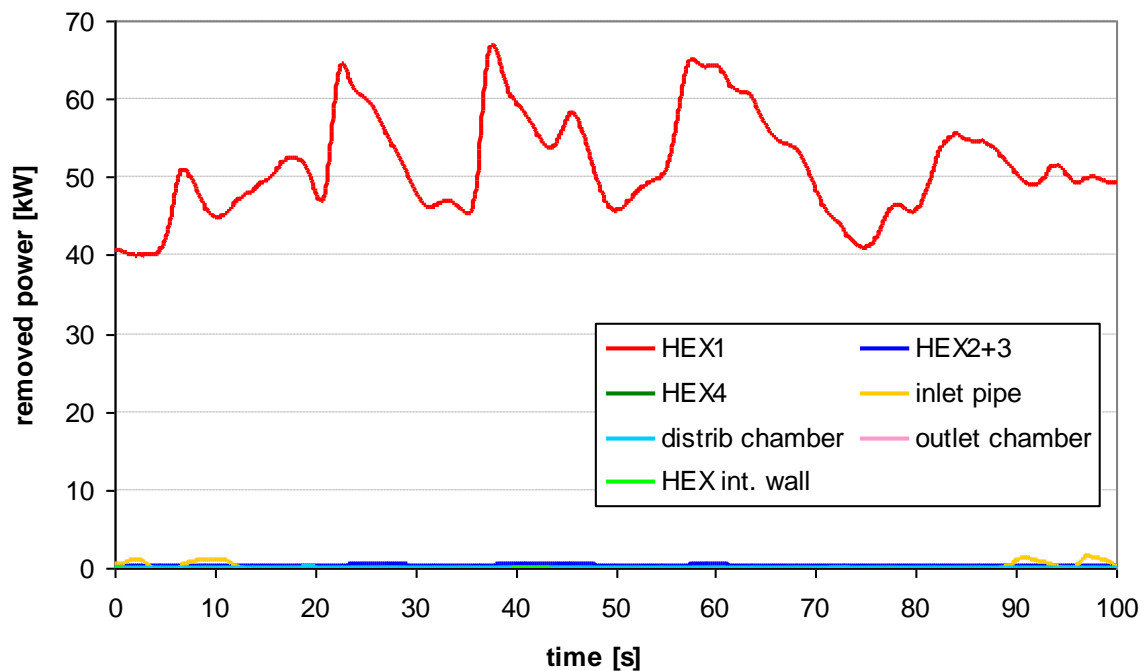


Figure 39: Time heat removal profiles in individual parts of the heat exchanger

The graph in Figure 39 shows the time history of power removal. Again, it can be seen that heat removal takes place only in the upper part of the tubes, with about 99 % of the power being removed through the surface of the tubes in the HEX1 section.

The situation is further illustrated by the temperature and velocity distribution  $v(z)$  on the vertical section in the plane of symmetry, which is shown in Figure 40. In the



intertubular space, higher helium temperatures are seen only in the upper part; the remaining parts are filled with helium cooled to a temperature close to the temperature at the surface of the heat transfer tubes. The outflow of the cooled helium back into the supply pipe is by means of a cold tongue that forms at the bottom of the distribution chamber. Subsequently, the cold tongue in the hot leg gradually mixes with the warmer helium flowing in from below. From the point of view of the velocity field, very low velocities are achieved in the intertubular space, averaging around  $0.1 \text{ m/s}$ . The more pronounced flow occurs in the upper region of the hot leg inlet pipe where the descending cooled and ascending warm helium meet.

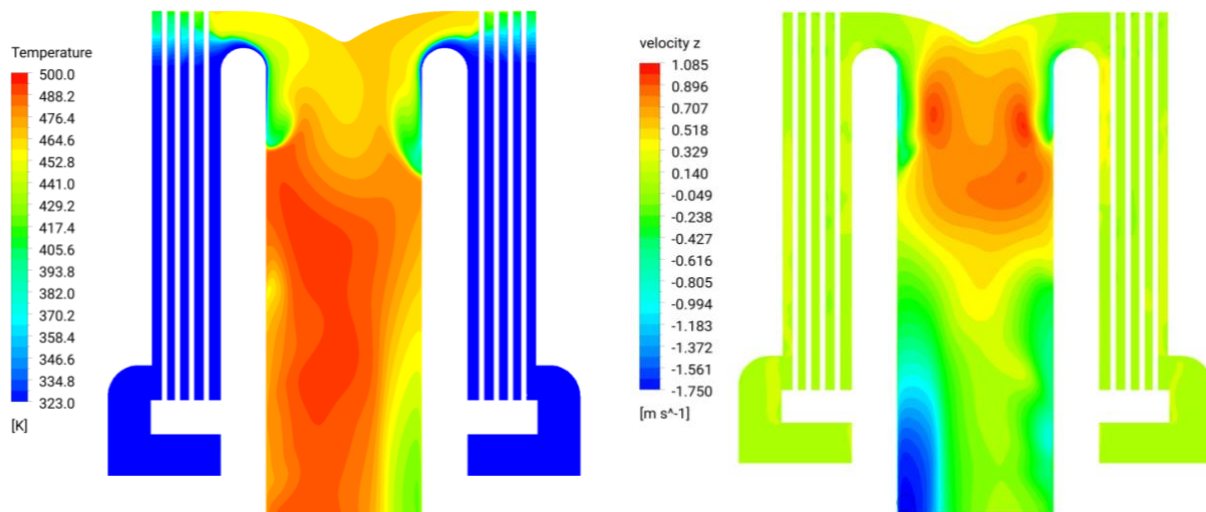


Figure 40: Heat exchanger temperature and z-velocity distribution in a time 100 s

The gradual mixing of helium in the hot leg pipeline can be observed in Figure 41, where the temperature and velocity distribution  $v(z)$  in selected horizontal sections is displayed. Here, the rising stream of hotter helium is kept near the inner side of the pipe elbow, while at the outer side the cooler helium flows downwards. This character is maintained over most of the vertical section of the pipe.

In the unsteady calculation, the average temperature in the hot leg pipe is kept almost constant in the range  $500\text{-}510 \text{ K}$ , while the maximum temperature in the hot leg pipe is given by the input value  $800 \text{ K}$ .

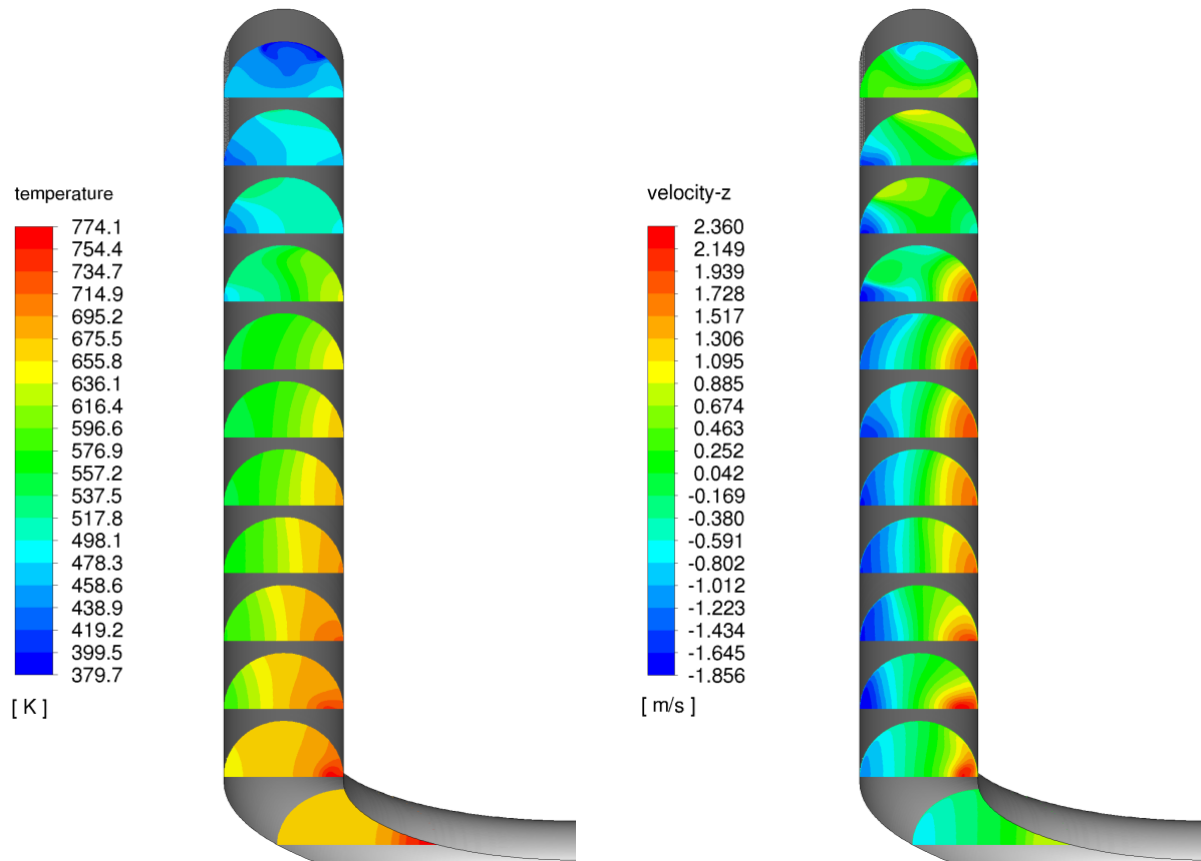


Figure 41: Hot leg pipe temperature and z-velocity distribution in a time *100 s*

### 7.3 SUMMARY

The test task allowed to analyze the Test Model as a whole, i.e. from the modelled area and computational mesh, through the suitability of the boundary conditions definition, to the selection of appropriate numerical models and the successful control of the iterative process. The main contribution was the insight into the quality of the computational mesh in the DHR heat exchanger region and the analysis of the boundary condition for heat removal from the helium flow. The analyses performed were subsequently reflected in the comprehensive model, see the modifications presented in Section 5.2.1.

## 8 COMPLEX MODEL CALCULATIONS

In order to achieve the objectives set out in Deliverable 3.4, a comprehensive model was developed and two basic tasks were performed on it. The first simulates the state of an isolated DHR loop when the reactor is operating at nominal parameters, the second task verifies the functionality of the loop during the initial part of the project accident with complete loss of electricity supply.

The simulation of normal reactor operation, where the DHR loop is closed at the point of the separation baffle between the hot and cold legs, is described in subsection 8.1. The input parameters and results presented in both subsections are related to a model with half symmetry, i.e. the mass flow rates and heat outputs for the whole DHR loop are in fact twice the values.

### 8.1 NOMINÁLNÍ PROVOZNÍ STAV NOMINAL OPERATIONAL STATE

The first problem solved on the Complex Model simulates the operating condition of the reactor at nominal values. The resulting values are then used as a starting point for the simulation of the transient scenario. For the nominal state simulation, the boundary conditions of the calculation are defined first, followed by a description of the results obtained.

#### 8.1.1 BOUNDARY CONDITIONS

Table 6 summarizes the settings of the main boundary conditions of the nominal operating state. All conditions at the inlets of both media are defined as constant throughout this calculation. In comparison to the simulation on the Test Model, the fluid zones with coolant inside the heat exchanger tubes are included in the Complex Model in the DHR exchanger (see subsection 4.2.1), where a new condition for the cooling water inlet has thus been set.

**Table 6 Setting of boundary conditions**

Location	Condition	Note
Helium hot leg inlet	Pressure inlet	Pressure was set at 0 Pa. Temperature was set 800 K. The pressure inlet condition allows to solve non-flow geometries, where one surface serves both as inlet and outlet.
Cold hot leg inlet	Pressure inlet	Pressure was set at 0 Pa. Temperature was set 530 K.
Colling water inlet	Mass-flow inlet	Temperature 363 K, mass-flow 6.1 kg/s.
The outer walls of the model	Wall (heat flux)	Adiabatic boundary condition (Heat flux = 0 W/m <sup>2</sup> ).
Materials interfaces	Wall (coupled)	Coupled condition of contact surfaces at the interface of different materials allowing free heat transfer.

### 8.1.2 SOLUTION AND RESULTS

In the first stage, the calculation was solved as stationary in order to obtain approximate distributions of velocity, temperature and other variables in the cold and hot legs. From this state, an unsteady simulation was then run in order to find a steady-state solution as far as possible. For these purposes, a simulation of 100 s was run, as in the case of the simulation run for the Test Model.

The behavior of the calculation is shown in the graph in Figure 42, where the maximum and mean temperatures in the individual parts of the heat exchanger are plotted. The results obtained are similar to the simulation of a separate hot leg of the loop within the Test Model. The active region of the exchanger is concentrated in the upper part (HEX1) where the hotter helium from the distribution chamber is flowing. The remaining parts of the exchanger are almost entirely filled with helium, the temperature of which is close to the temperature at the surface of the water-cooled heat exchanger tubes in many places, where the inlet temperature is 363 K. In the first part of the calculation, oscillations of the maximum temperature in the HEX2+3 section can be seen, which are caused by the occasional intrusion of warmer helium into the upper region of this section of heat exchanger.

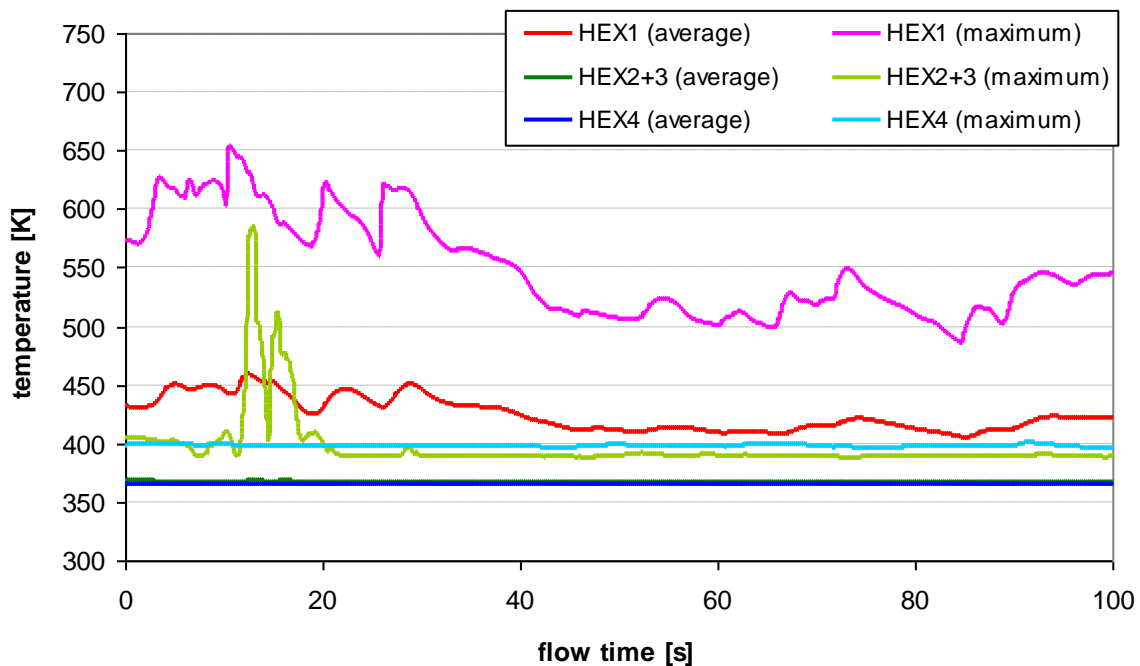


Figure 42: Time temperature profiles in individual parts of the heat exchanger

The temperature distribution in Figure 43 shows a relatively insignificant heating of the helium in the outlet chamber. This is due to its significantly lower temperature in the cold loop, which heats the steel baffle from below. The power delivered is only in the order of a few kilowatts.

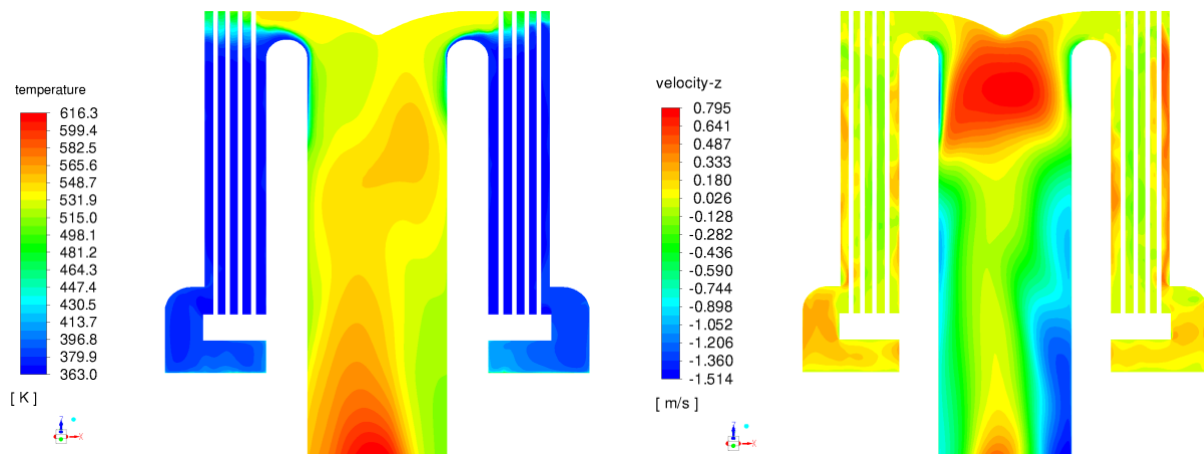


Figure 43: Heat exchanger temperature and z-velocity distribution at the end of stabilization calculation

Figure 44 shows the time history of the power removal, which reflects the temperature distribution in Figure 43. The heat removal to the cooling water reaches approximately  $70 \text{ kW}$  at the end of the simulation. About 85 % is removed through the upper part of the heat exchanger (HEX1), while the remaining power is removed in the HEX2+3 section.

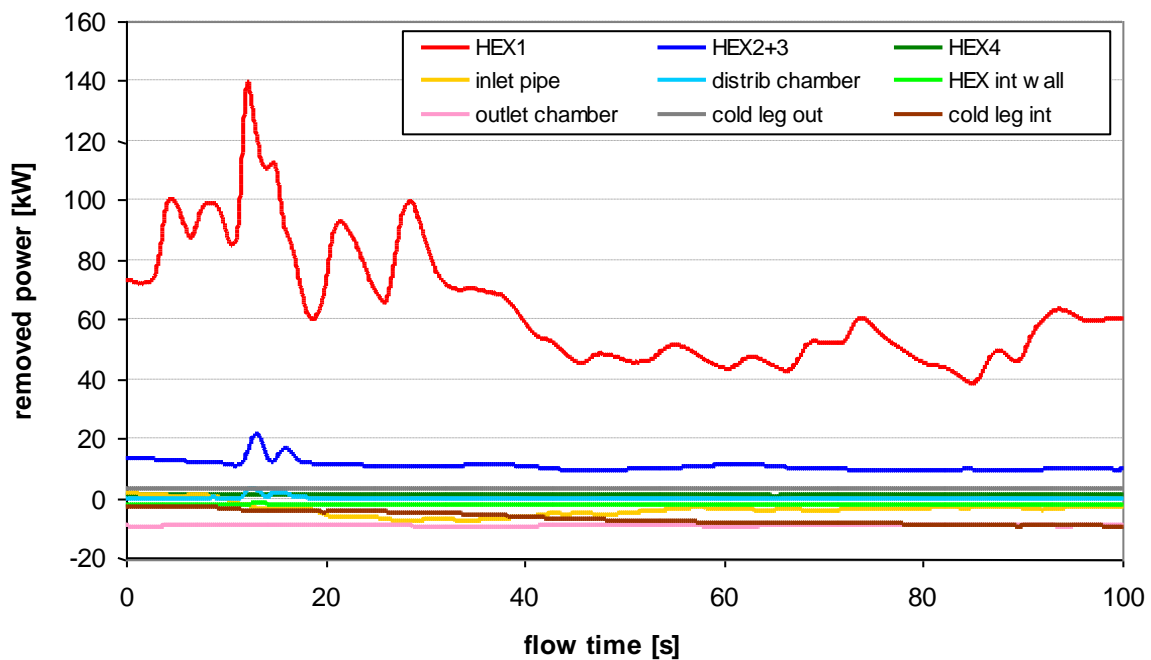


Figure 44: Time heat removal profiles in individual parts of the HEX and others parts of simulated geometry

It can also be seen from the graph that the power delivered from the cold leg through the steel baffle to the heat exchanger outlet chamber is relatively small and is only around  $9 \text{ kW}$ . The power passing through the wall and insulation separating the hot and cold legs is also at a similar level.

Furthermore, significant oscillations of the power dissipated between  $t = 10\text{ s}$  and  $t = 30\text{ s}$  can be observed in Figure 44, which correspond to the temperature profiles in Figure 42. These oscillations are also reflected in the distribution chamber, see Figure 45.

It is clear that for the Complex Model, the prediction using the stationary calculation is no longer as accurate as it was for the Test Model where the temperatures at the surface of the heat exchanger tubes were defined in a fixed way. In this case, the non-stationary part of the calculation is therefore an important part of the problem to be solved.

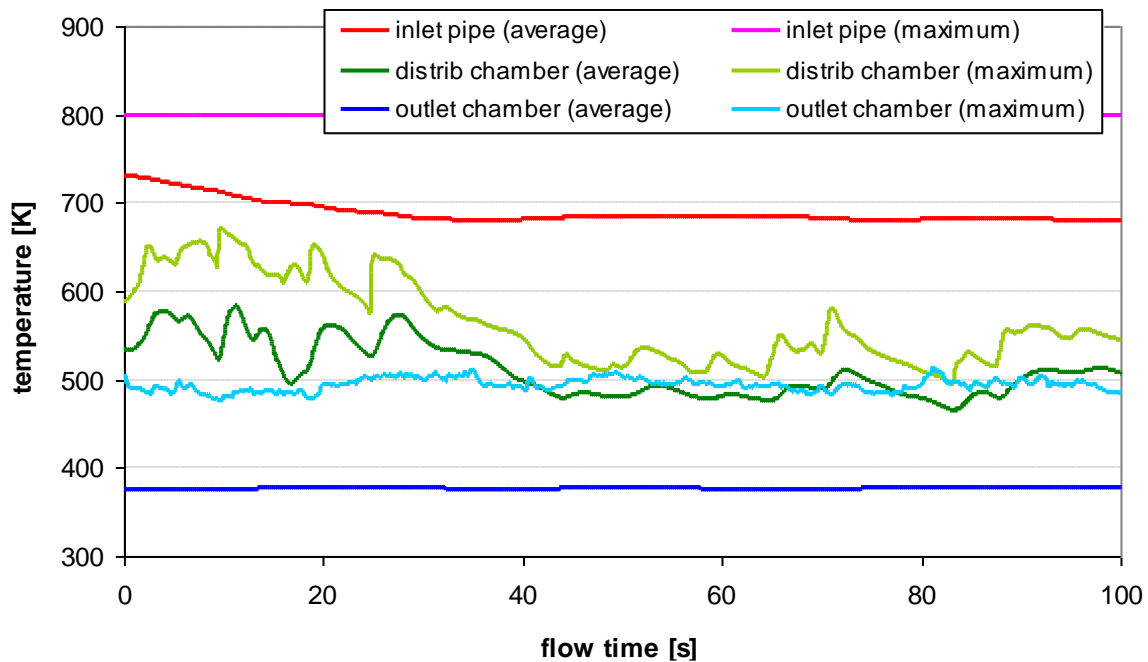


Figure 45: Time temperature profiles in other parts of hot leg

The fact that the character of the flow is close to the simulation of a separate hot leg is also evident in Figure 46, which shows the temperature and velocity distribution  $v(z)$  in selected horizontal sections of the hot leg pipe. Here, the inflowing hotter helium stream is confined to the inner side of the arch and the connected vertical section of hot leg pipe where it rises upwards. The helium cooled in the exchanger then flows down the opposite side. This character is maintained for most of the vertical section, only at the top of the hot leg pipe is it affected by the mixing of the coolant below the distribution chamber.

The graph in Figure 47 shows the temperature trends in the cold leg of the loop. It can be seen that the temperatures here are largely stable and without significant oscillations. The maximum temperatures exceed the temperature defined in the boundary condition at the cold leg inlet ( $530\text{ K}$ ) by several degrees, which has two basic causes. The first one is the fact that during the initialization of the calculation, the temperature in the insulation and the steel pipe was set to  $600\text{ K}$ , which causes a gradual transfer of accumulated heat from the wall to the cold leg during the simulation. The heating of the helium in the cold leg is also partly due to the heat transfer from the hot leg through the insulation and steel wall. The graph in Figure 44 shows that this power input gradually increases to a value approaching  $10\text{ kW}$ .



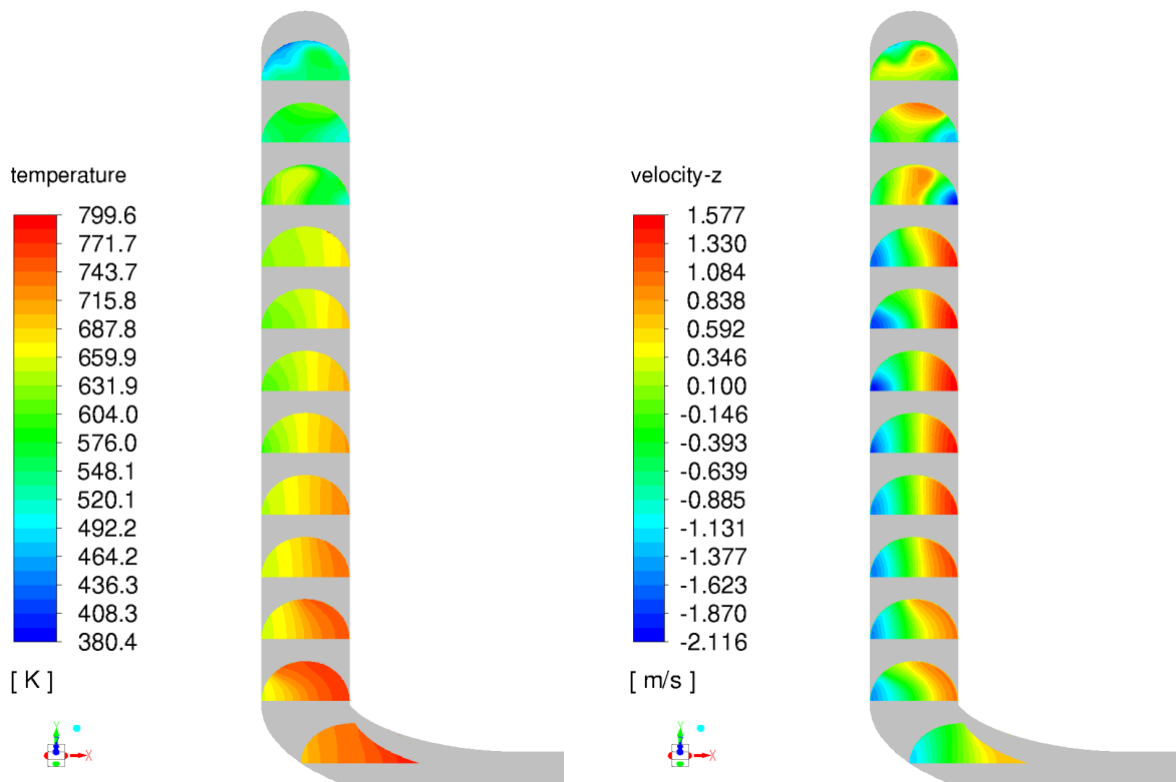


Figure 46: Hot leg pipe temperature and z-velocity distribution at the end of stabilization calculation

Figure 48 shows in selected horizontal sections the distribution of helium temperature and velocity  $v(z)$  throughout the vertical section of the cold leg and the distribution chamber. The velocities  $v(z)$  indicate similar behavior to that found in the hot leg supply line. An upward flow is formed over the inside of the arch and an equally downward flow on the outside. The temperatures, on the other hand, are largely balanced. The heat transfer between the hot leg and the cold leg probably has some influence.

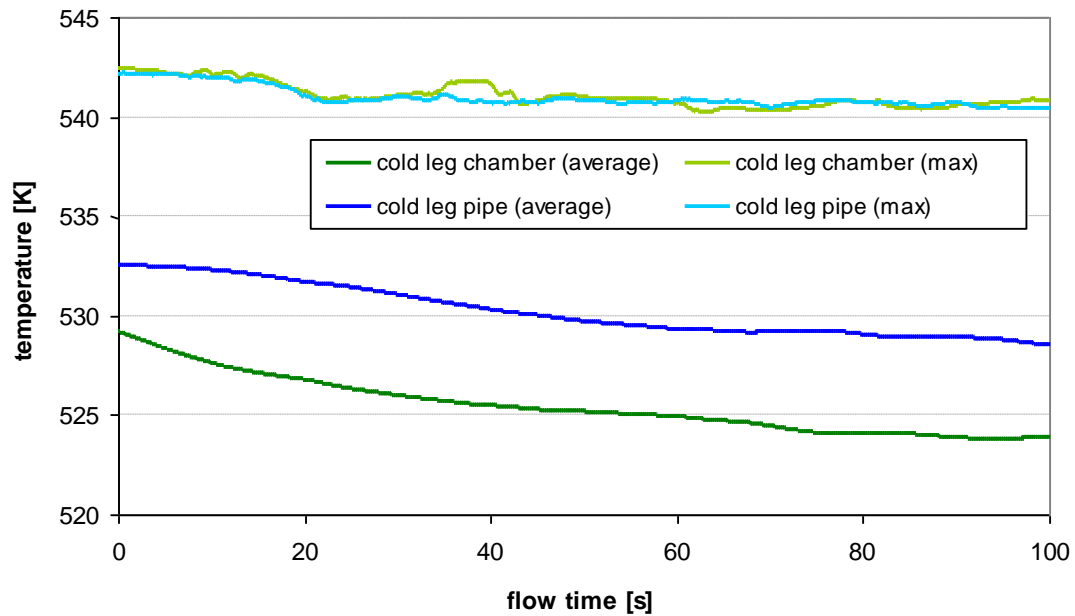


Figure 47: Time temperature profiles in parts of cold leg

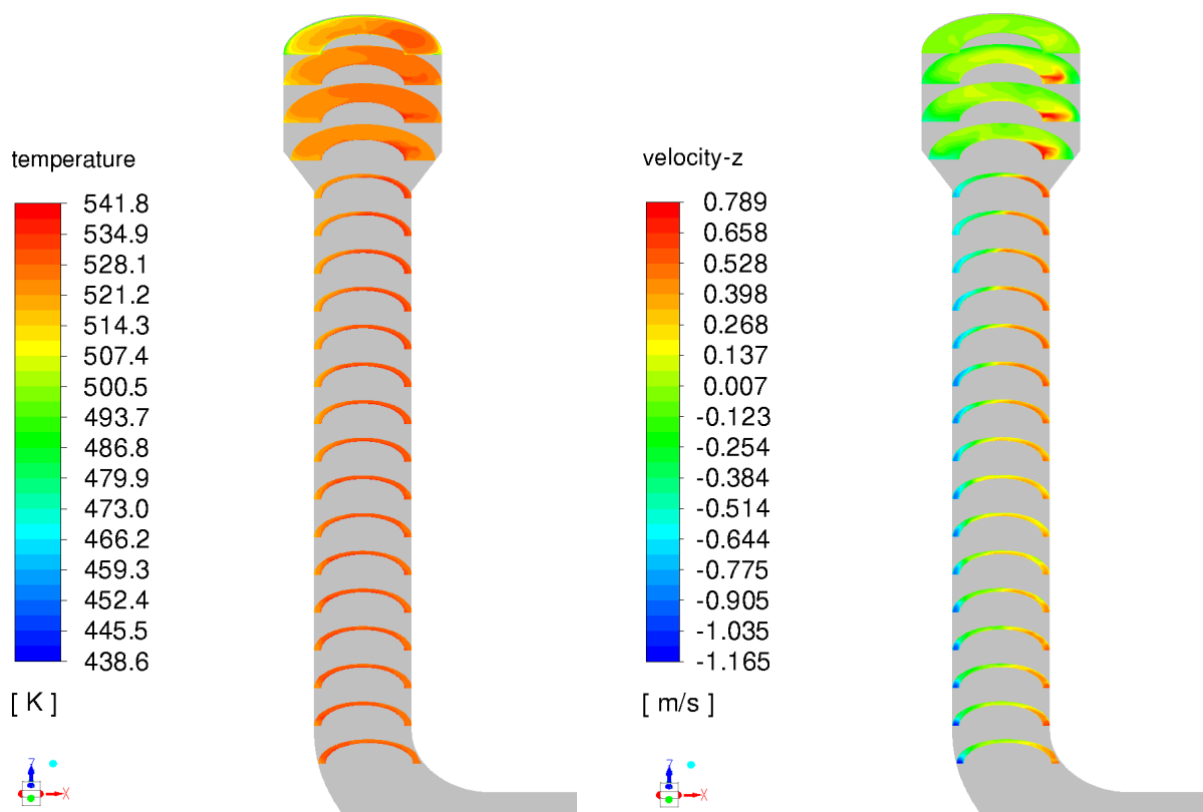


Figure 48: Cold leg pipe temperature and z-velocity distribution at the end of stabilization calculation

## 8.2 HAVARIJNÍ STAV EMERGENCY CONDITION

The second problem, solved on the Complex Model, simulates the initial part of an emergency condition with complete loss of external power supply. The problem is further

divided into two phases. The first one is characterized by changes at the reactor/DHR loop interface until a flap in the steel baffle separating the two legs of the DHR loop opens (time  $t = 56$  s). The second phase of the calculation then simulates the start of the helium circulation after the interconnection of the two legs, up to time  $t = 126$  s. To describe both phases of the calculation, a subsection defining the boundary conditions of the emergency scenario is included below.

### 8.2.1 SOLVED SCENARIO

The input parameter profiles for both media are shown in Figure 49 to Figure 52. The values shown in the graphs are based on the results of a crash simulation using the RELAP system thermohydraulic code [7].

The graph in Figure 49 describes the helium temperature profile during the first phase of the transition state, at the inlet to both the hot and cold legs. Similarly, the graph in Figure 50 shows how the temperature and mass flow of cooling water at the inlet to the tube bundle is defined.

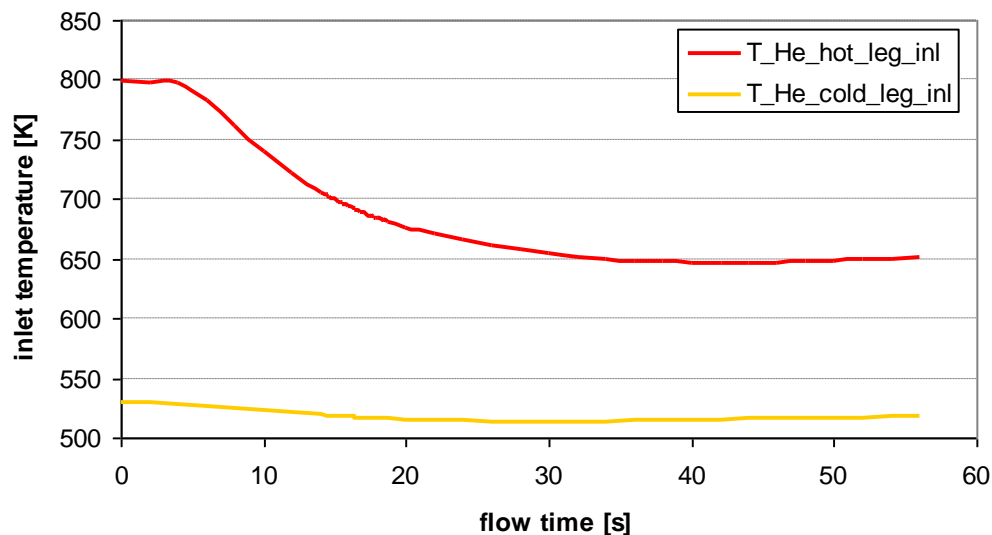


Figure 49: Temperature profiles for helium inlets

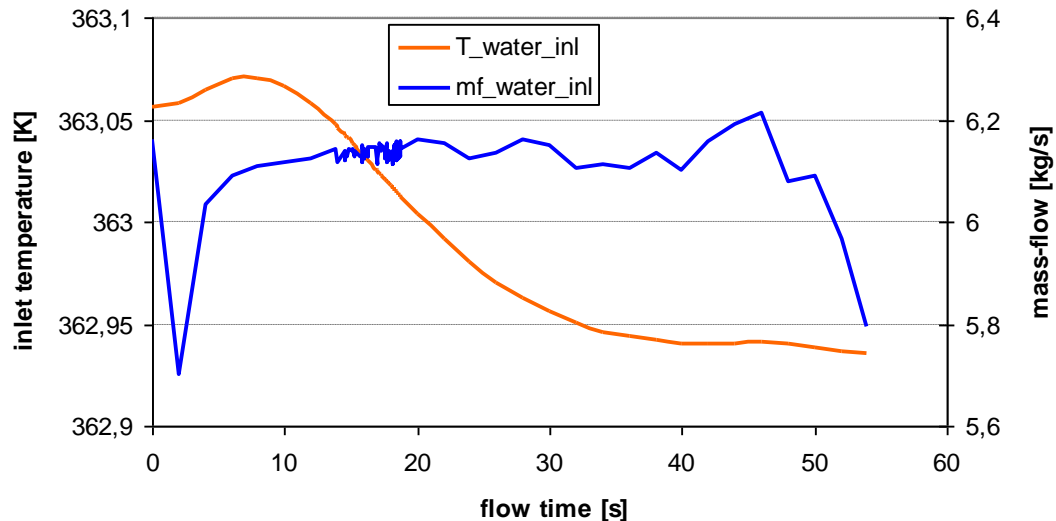


Figure 50: Temperature and mass-flow profiles for water inlet

At time  $t = 56$  s, the flaps in the baffle between the hot and cold legs of the DHR loop open. Figure 51 shows the time history of the inlet helium temperatures during both phases of the simulated event, with the moment of baffle opening indicated by the dashed line. The temperature on the hot leg gradually increases from  $651$  K at the beginning of the second phase of the simulation to  $681$  K at the end of the simulation. In the case of the cold leg, on the other hand, the temperature drops from  $520$  K to approximately  $470$  K. The graph also describes the profile of the static pressure at the inlet of the hot leg, which is defined from the moment of the connection of the two parts of the loop.

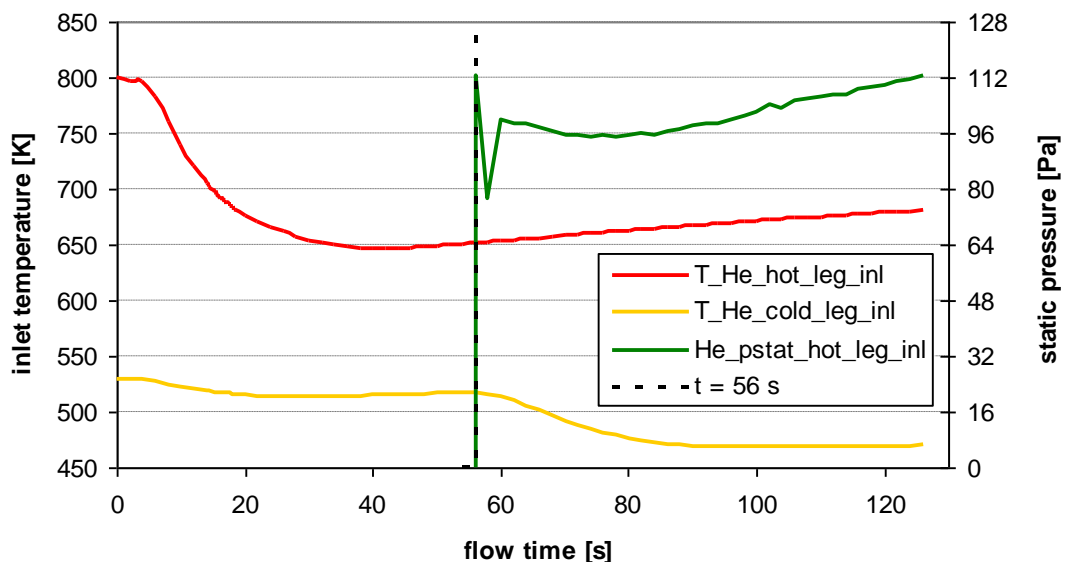


Figure 51: Temperature and pressure profiles for helium inlets

The graph in Figure 52 shows the profiles of cooling water mass flow and temperature. The point at which the two parts of the loop are connected is again indicated on the graph by a vertical dashed line. A gradual increase in temperature of approximately  $20$  K can be seen after the two loops are connected. The mass flux development depends on the time

the circulator is powered from the batteries after the SBO is formed (about 60 s). After  $t = 60$  s, the flow rate subsequently drops to virtually zero ( $t = 72$  s). This is followed by a rapid increase to a level of 5 kg/s, which is due to the gradual start of natural circulation. At the end of the simulated part of the transient, the mass flux is assumed to gradually decrease, reaching only 0.4 kg/s at  $t = 96$  s and then gradually decreasing to 0.023 kg/s at  $t = 126$  s, when the simulation ends.

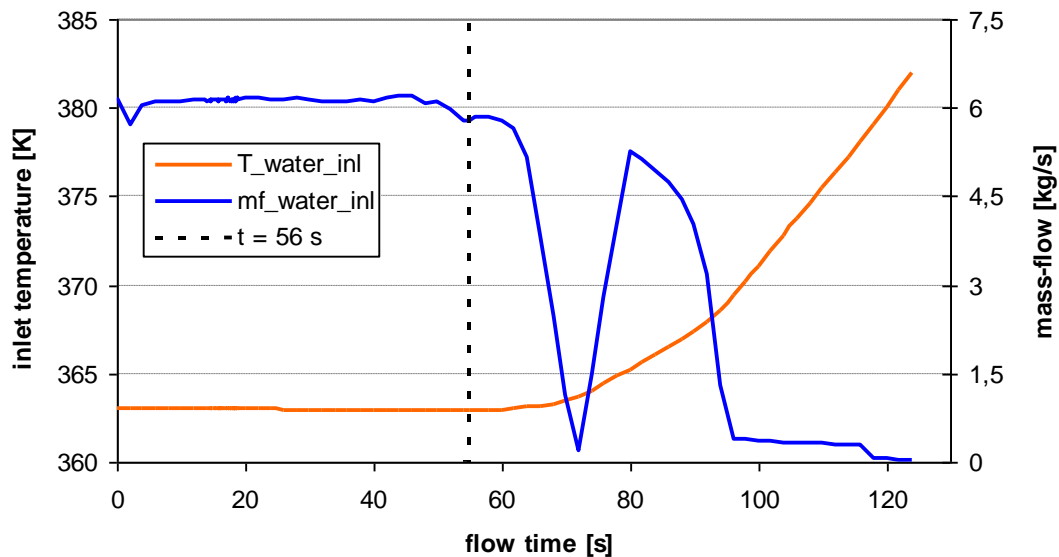


Figure 52: Temperature and mass-flow profiles for water inlet

## 8.2.2 TRANSIENT CALCULATION – FIRST PHASE

In the first phase of the simulation of the accident under consideration, changes already occur at the reactor/DHR loop interface and last until the opening of the flaps in the steel baffle at the interface of the two legs of the DHR loop is initiated. The initiation of this phase is simulated as a state at time  $t = 0$  s and lasts until  $t = 56$  s. The progression of the boundary conditions and the results obtained are presented in the following subsections.

### 8.2.2.1 Boundary conditions

Table 7 summarizes the setting of the main boundary conditions for the second phase of the transient. The conditions at the inlets of both media were taken from the crash simulation results, see Figure 49 and Figure 50. The individual time dependents of the values are defined in ANSYS Fluent using the profile function.

**Table 7 Setting of boundary conditions**

Location	Condition	Note
Helium hot leg inlet	Pressure inlet	Pressure was set at 0 Pa. Temperature was set via profile displayed in Figure 49. The pressure inlet condition allows to solve non-flow geometries, where one surface serves both as inlet and outlet.

Helium cold leg inlet	Pressure inlet	Pressure was set at 0 Pa. Temperature was set via profile displayed in Figure 49.
Colling water inlet	Mass-flow inlet	Temperature and mass-flow was set via profiles displayed in Figure 50.
Outer walls of the model	Wall (heat flux)	Adiabatic boundary condition (Heat flux = 0 W/m <sup>2</sup> ).
Materials interfaces	Wall (coupled)	Coupled condition of contact surfaces at the interface of different materials allowing free heat transfer.

### 8.2.2.2 Solution and results

The behavior of the calculation is shown in the graphs in Figure 53 and Figure 54, where the maximum and mean temperatures in the individual parts of the heat exchanger and in other parts of the hot leg (inlet pipe, distribution chamber and outlet chamber of the heat exchanger) are plotted.

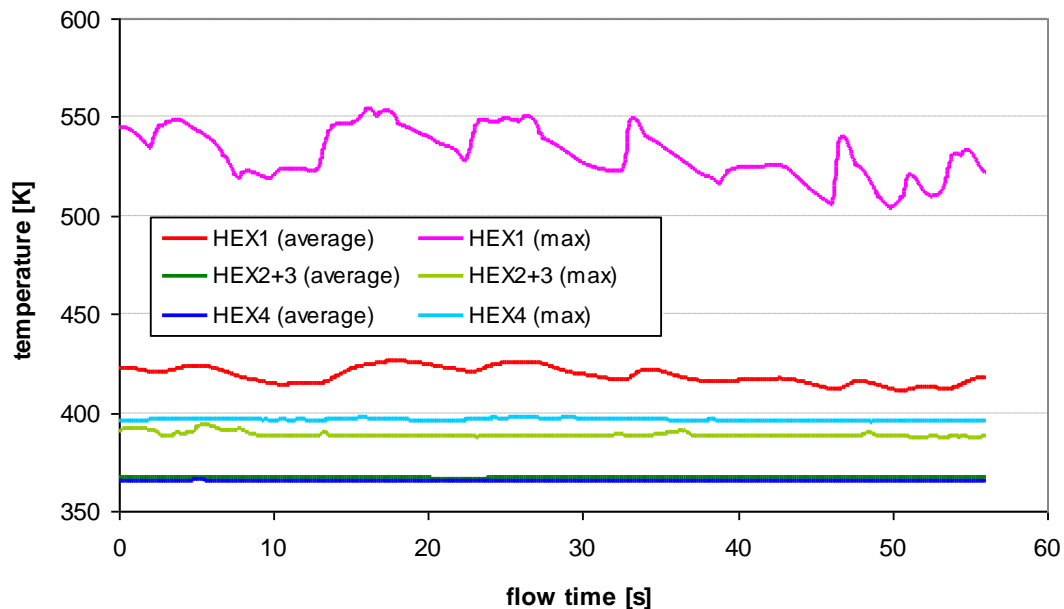


Figure 53: Time temperature profiles in the individual parts of the heat exchanger



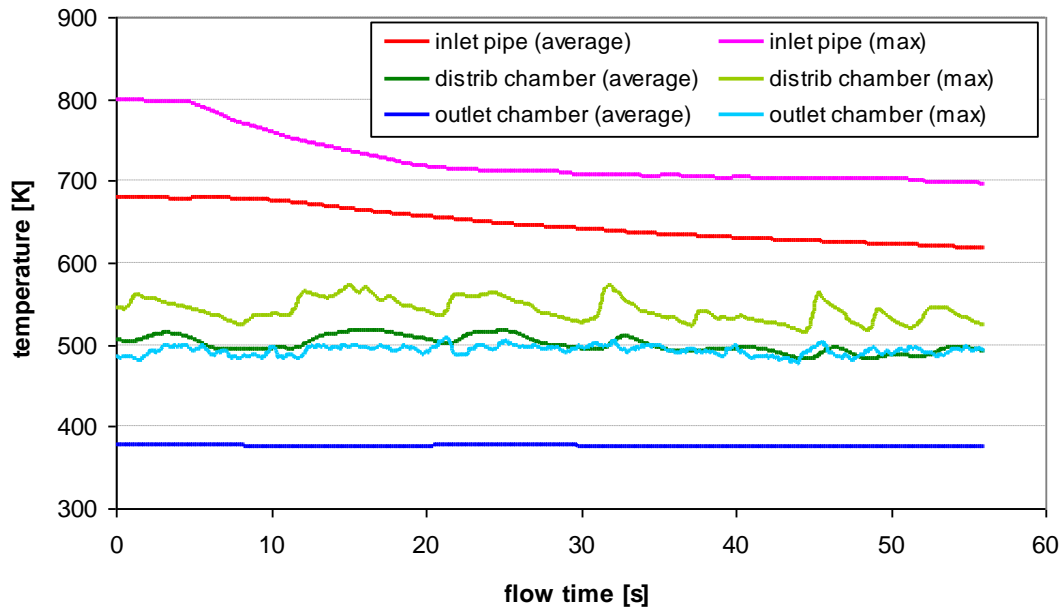


Figure 54: Time temperature profiles in the other parts of the hot leg

It can be seen from both graphs that the change in helium temperature at the hot leg inlet is particularly pronounced in the hot leg inlet pipe, where both the maximum and mean helium temperatures drop significantly, as the inlet helium temperature drops.

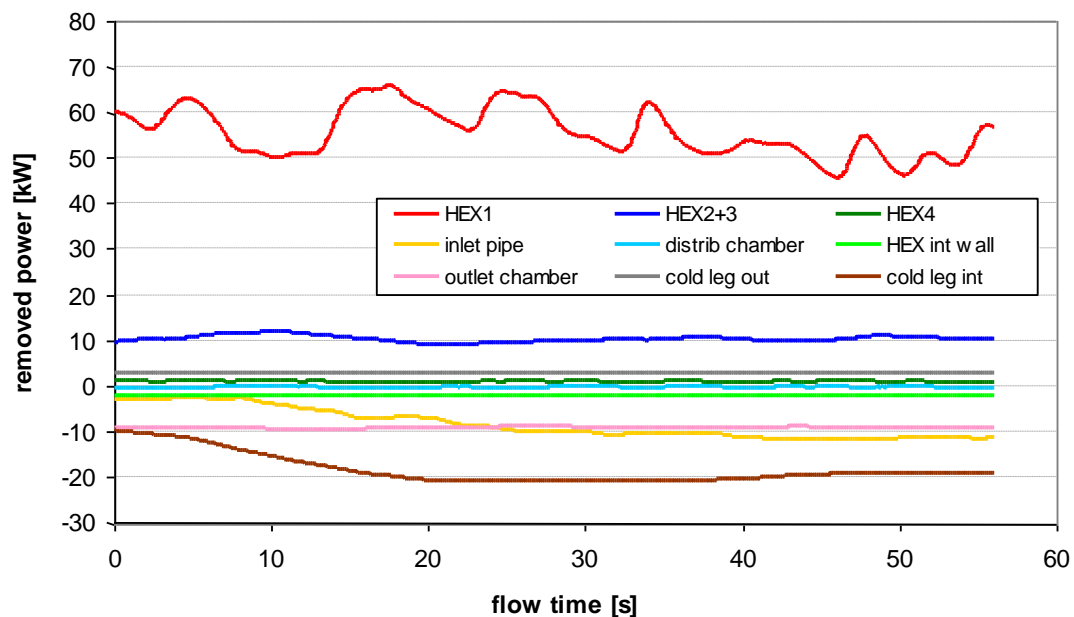


Figure 55: Time heat removal profiles in individual parts of the HEX and others parts of simulated geometry

The graph in Figure 55 shows the time history of the power removal. The graph shows that the situation did not change significantly during this phase of the simulation. There is only a slight decrease in the power dissipated in the HEX1 part of the heat exchanger. The remaining parts of the heat exchanger are affected by the heat input to the heat

exchanger outlet chamber through the steel baffle that separates it from the cold leg. Another noticeable change is the increase in power entering the helium in the feed line.

Figure 56 shows the temperature and velocity distribution  $v(z)$  on the plane of symmetry at the top of the hot leg pipe and in the DHR exchanger space. It can be seen that the helium heating in the outlet chamber space is relatively small. The situation is similar in the downstream parts of the HEX4 and HEX2+3 exchanger, where the maximum temperatures are around  $390\text{ K}$ .

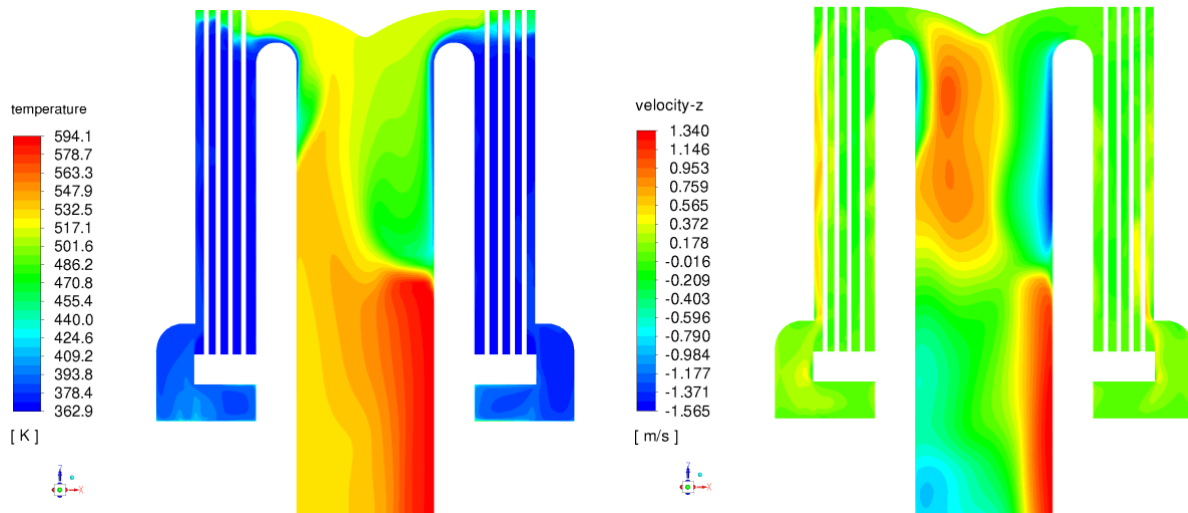


Figure 56: Heat exchanger temperature and z-velocity distribution in a time 56 s

In Figure 57, the temperature and velocity distributions  $v(z)$  are shown on selected horizontal sections in the hot leg pipe for the condition at the end of the first phase of the simulated transient. The resulting temperature and velocity distributions here are very similar to the condition at the end of the calculation that simulated the normal operating condition.

The temperature distribution at the end of the first phase of the calculation ( $t = 56\text{ s}$ ) shows slightly less pronounced gradients than in the case of the simulated normal operating condition. This is due to the decrease in the inlet temperature and thus a reduction in the overall temperature difference.

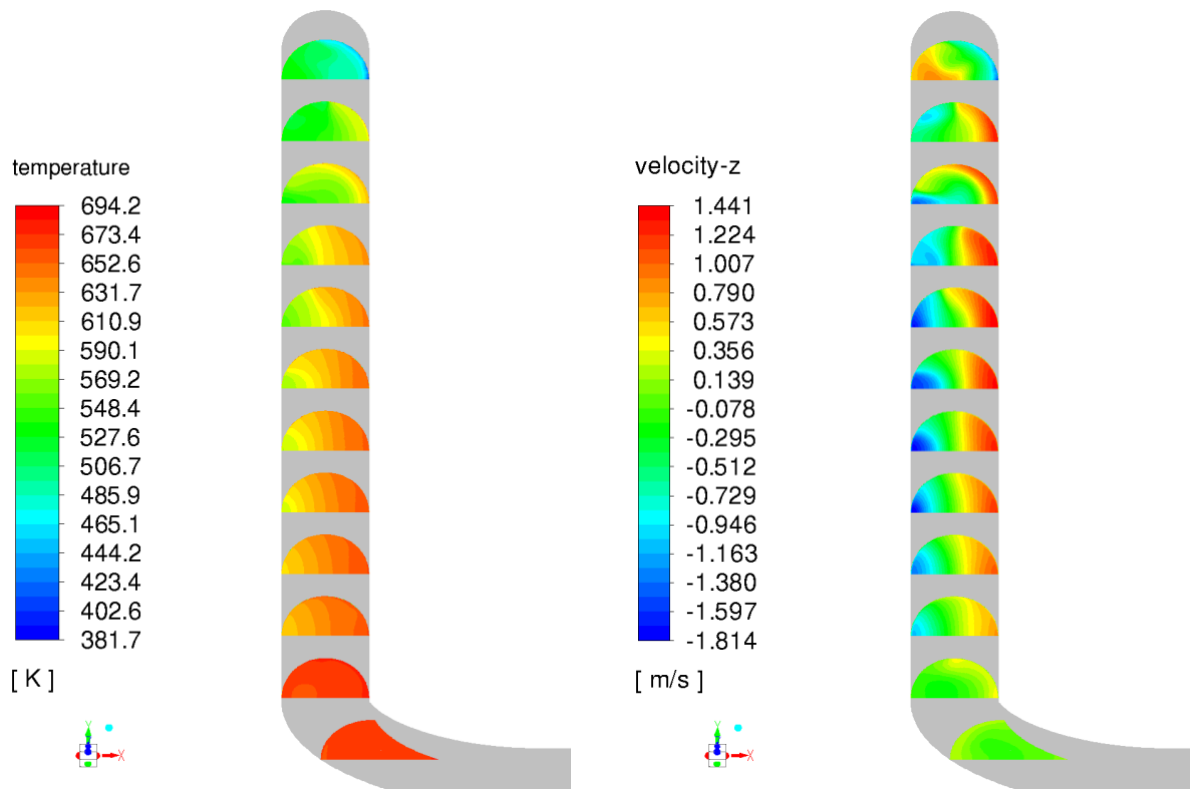


Figure 57: Hot leg pipe temperature and z-velocity distribution in a time 56 s

The graph in Figure 58 shows the temperature profiles in the cold leg of the loop. The graph shows that there are no significant changes in the temperature distribution in the cold leg during the simulated transient.

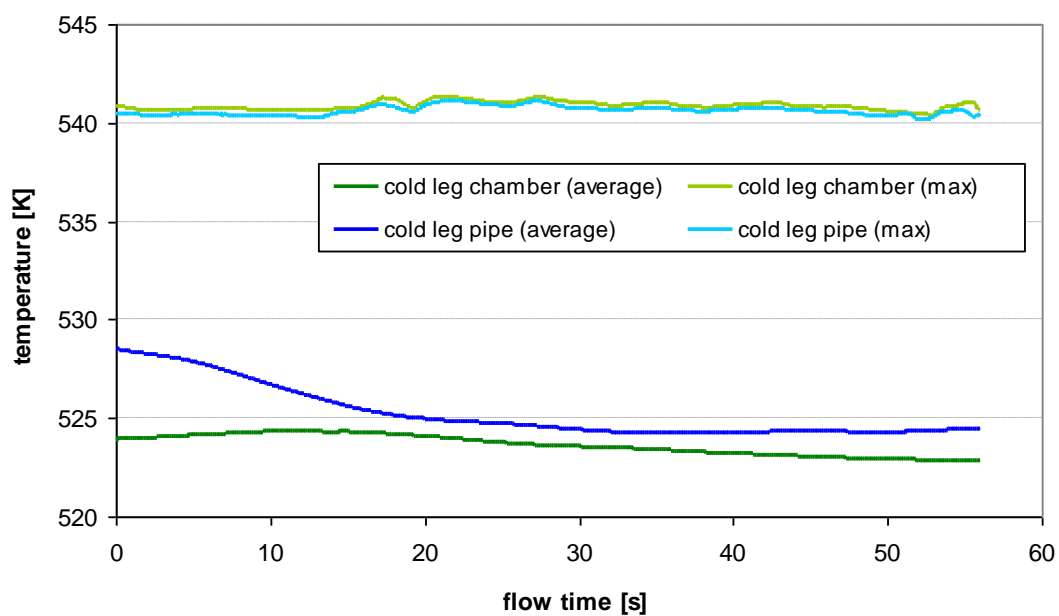


Figure 58: Time temperature profiles in the parts of the cold leg

Figure 59 shows the distribution of helium temperature and velocity  $v(z)$  in the selected horizontal sections throughout the vertical section of the cold leg pipe and the distribution chamber. The temperature distribution here is largely uniform and thus no significant temperature differences between the rising and descending streams are apparent. In the case of the velocity distribution  $v(z)$ , on the other hand, there are clearly visible upward and downward currents with velocities up to  $1 \text{ m/s}$ .

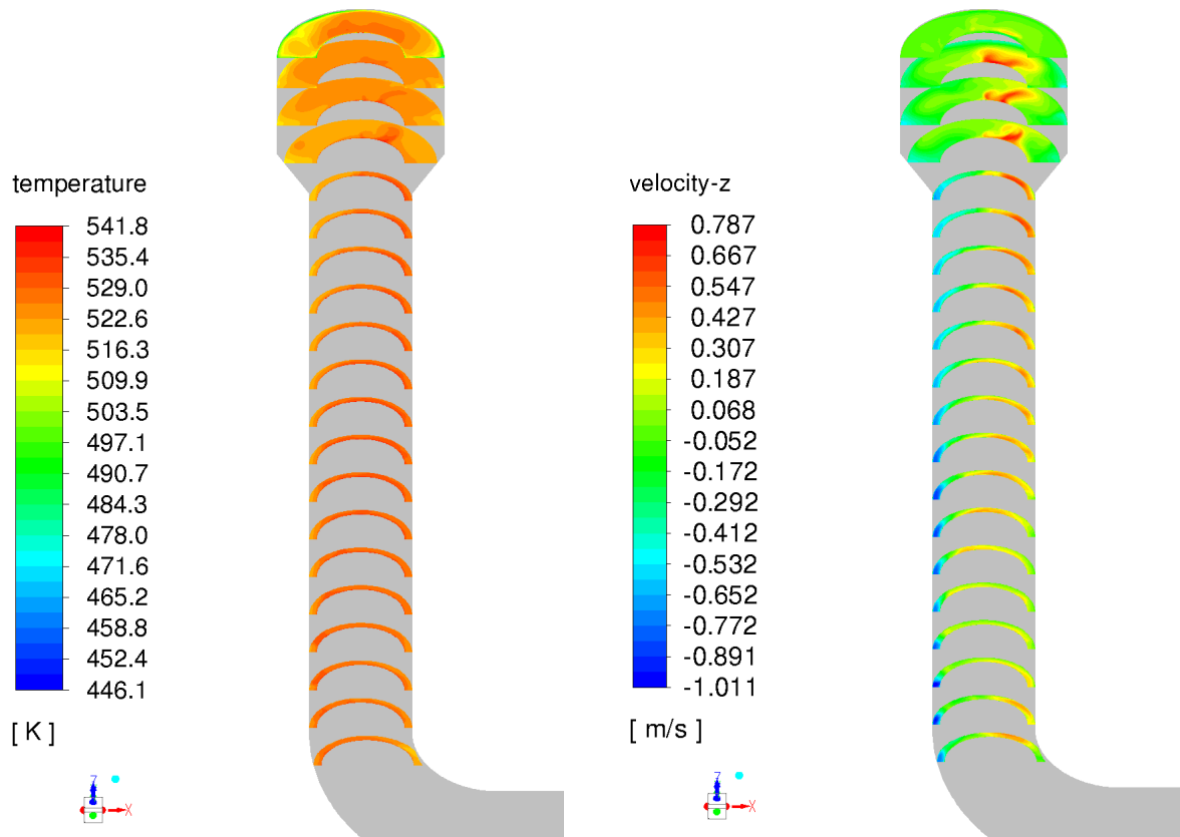


Figure 59: Cold leg pipe temperature and z-velocity distribution in a time 56 s

### 8.2.3 TRANSIENT CALCULATION - SECOND PHASE

The second part of the transient simulates the start of the helium circulation after the connection of the two legs, i.e. between times  $t = 56 \text{ s}$  and  $t = 126 \text{ s}$ . The boundary conditions and the results of the simulations are presented in the following subsections.

#### 8.2.3.1 Boundary conditions

Similar to the simulation of the first phase of the transient, where the two parts of the loop remained separated, profiles are used to define the boundary conditions at the cooling water and helium inlets, see Section 8.1. The setting of the main boundary conditions is summarized in Table 8.

**Table 8 Setting of boundary conditions**

Location	Condition	Note
Helium hot leg inlet	Pressure inlet	Pressure and temperature were set via profile displayed in Figure 51. The pressure inlet condition allows to solve non-flow geometries, where one surface serves both as inlet and outlet.
Cold hot leg inlet	Pressure outlet	Pressure was set to 0 Pa. Temperature was set via profile displayed in Figure 51.
Colling water inlet	Mass-flow inlet	Temperature and mass-flow were set via profiles displayed in Figure 52.
The outer walls of the model	Wall (heat flux)	Adiabatic boundary condition (Heat flux = 0 W/m <sup>2</sup> ).
Materials interfaces	Wall (coupled)	Coupled condition of contact surfaces at the interface of different materials allowing free heat transfer.

### 8.2.3.2 Solution and results

At time  $t = 56$  s, the hot and cold legs are connected through open flaps in the steel baffle. Then, almost immediately (within 1 s), the flow is adjusted in the direction from the hot to the cold leg. As can be seen from Figure 60, a maximum flow of about 2.8 kg/s is reached at about time  $t = 65$  s. Subsequently, the flow through the loop gradually decreases to a value of 2.25 kg/s at the end of the simulated process.

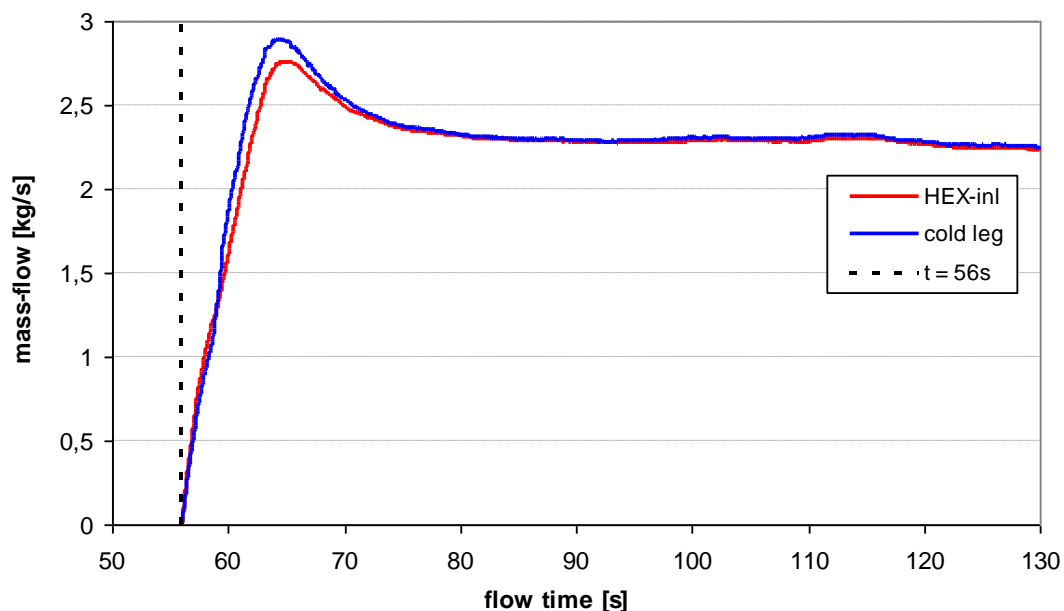


Figure 60: Mass-flow monitoring in hot and cold leg

The graphs in Figure 61 and Figure 62 show the temperature profile in the hot leg and in the active part of the heat exchanger. The temperature profile in the supply line and the distribution chamber is very rapidly flattening, which is newly determined by the increasing amount of helium flowing into the hot leg. At time  $t = 66$  s, the temperatures

are already rising slowly as the inlet temperature rises. A similar pattern of temperature rise with a slight transport delay is seen at the outlet chamber of the heat exchanger. As the helium gradually cools, the difference between the average and maximum temperature is maintained.

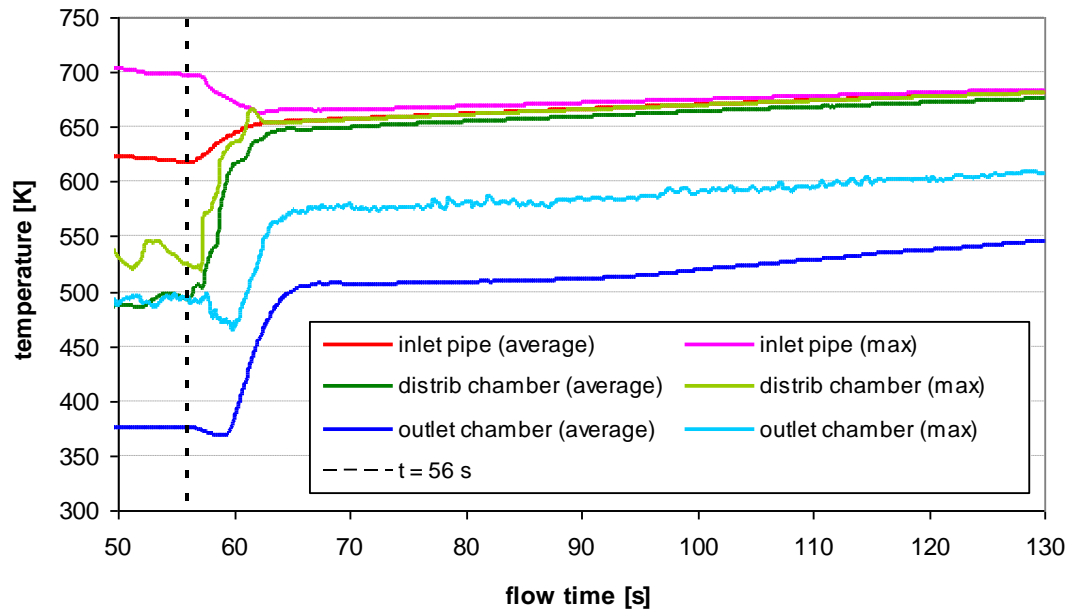


Figure 61: Time temperature profiles in other parts of the hot leg

The flow regime change in the active part of the heat exchanger is shown in Figure 62. The temperature profiles correspond to the temperature profiles in Figure 61. The slight overshoot of the maximum temperature, which is observed for the HEX1 and HEX2+3 section, is due to the inflow of a portion of the more heated helium accumulated in the upper part of the hot leg inlet pipe. At the same time, it can be seen how as the helium cools down, the non-uniformity in terms of temperature increases, with the difference between the maximum and average temperature in the HEX4 section reaching approximately 90 K. The difference between the maximum and minimum temperature is even more than 200 K.



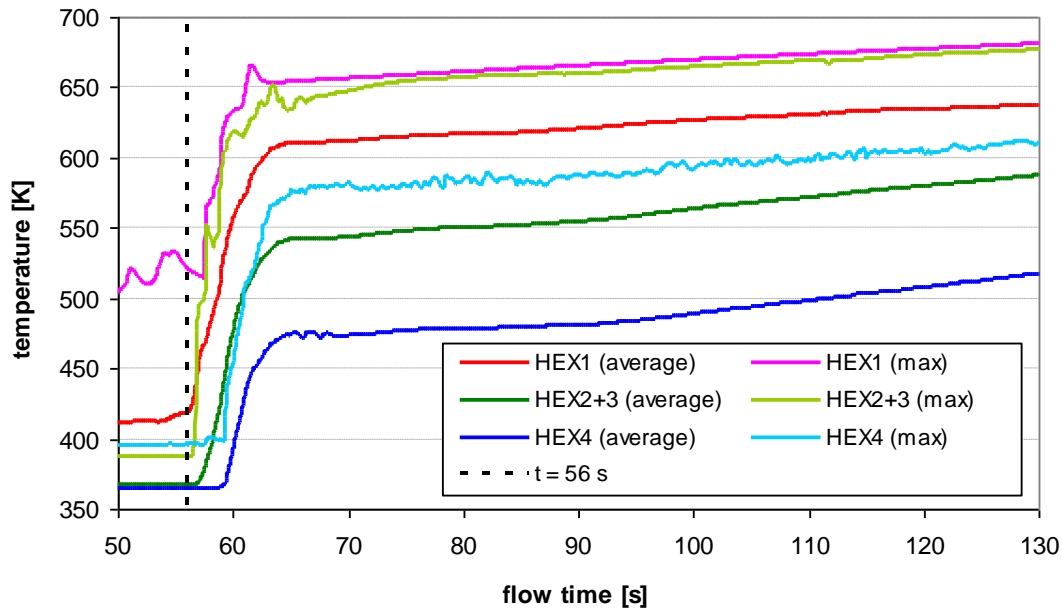


Figure 62: Time temperature profiles in individual parts of the heat exchanger

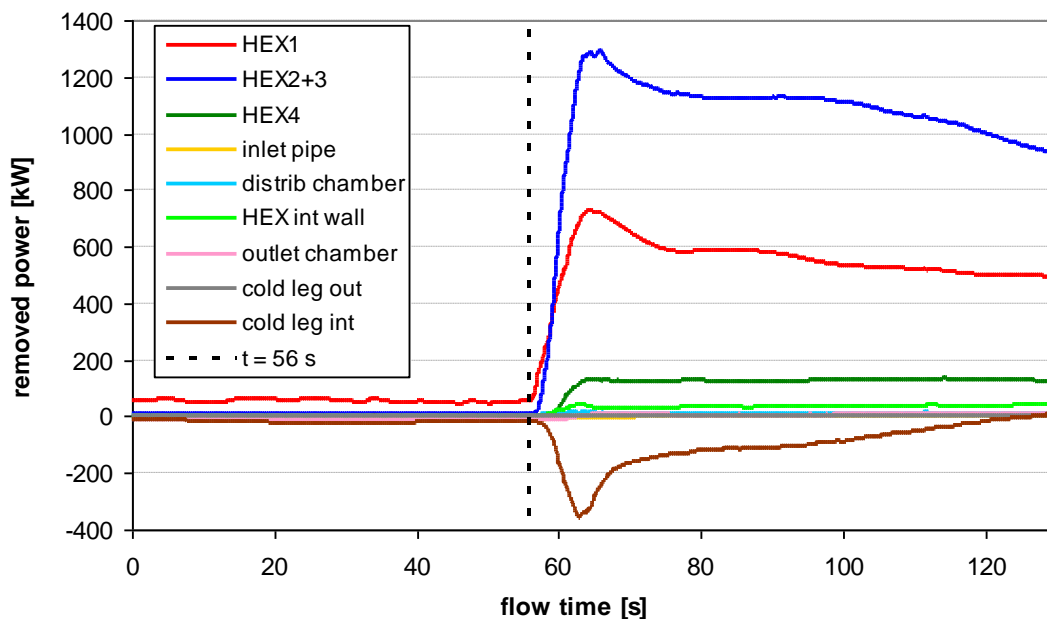


Figure 63: Time heat removal profiles in the individual parts of the HEX and the others parts of simulated geometry

The change of the loop flow regime also affects the heat removal rates, see Figure 63. The 70 kW power removed to the cooling water during the separated loops in the second phase of the transient reaches a maximum at time  $t = 66$  s of approximately 2100 kW. Thereafter, there is a gradual decrease to 1500 kW at the end of the simulated transient. In contrast to the mode before the opening of the flaps, most of the power is dissipated here in the HEX2+3 part, as expected. The reason is that this section is much larger than HEX1 and HEX4 respectively. The resulting negative power dissipation on the cold leg wall is due to the gradual displacement of cold helium that has been collected and cooled

in the exchanger intertube space and the exchanger outlet chamber before the flaps open. The cold leg thus receives helium at a significantly lower temperature than the temperature of its walls.

Temperature profiles of the cooling water at the outlet of each tubes series of heat exchanger are displayed in Figure 64. The rapid rise in water temperature after opening the flaps is very well apparent. The time delay of start of this rise corresponds roughly to the duration of the helium flow through the heat exchanger. From approximately  $t = 70$  s onwards, a further temperature rise is evident due to the decrease in cooling water flow and lasts until approximately  $t = 80$  s when the coolant flow is restored.

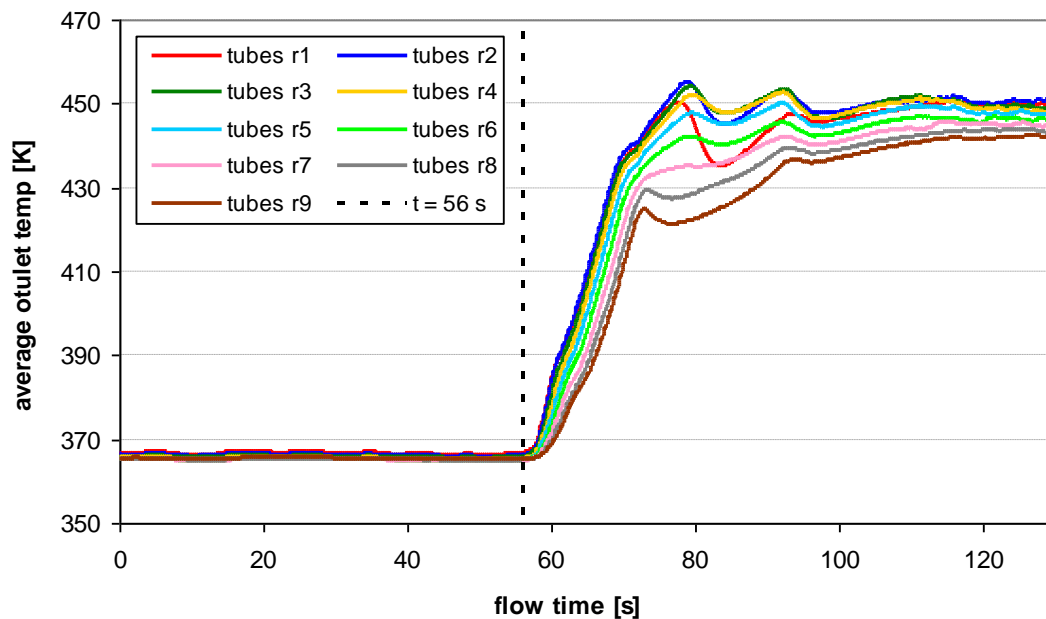


Figure 64: Time water temperature profiles on heat exchanger tubes outlets

The change in the helium temperature distribution in the DHR region of the exchanger after the two loop sections are connected is illustrated in Figure 65, which shows the temperature and velocity distribution  $v(z)$  on the plane of symmetry for  $t = 66$  s. Both the supply line and the distribution chamber are filled with helium at a temperature close to the temperature condition at the hot leg inlet. During the flow through the heat exchanger, a gradual temperature drop can then be observed, which on average reaches approximately  $150$  K. The velocity distribution  $v(z)$  shows that there is some stratification in the inlet pipe. As a result of the abrupt change in the nature of the flow, a drift is formed on the inside of the bend in the supply pipe, in which the flow slows down significantly to stagnation.

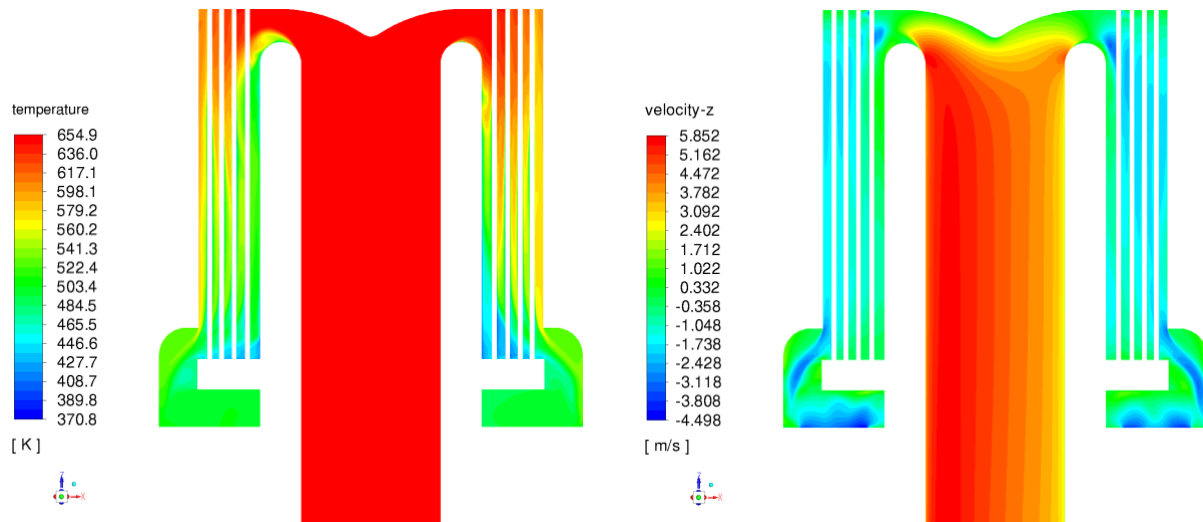


Figure 65: Heat exchanger temperature and z-velocity distribution in a time 66 s

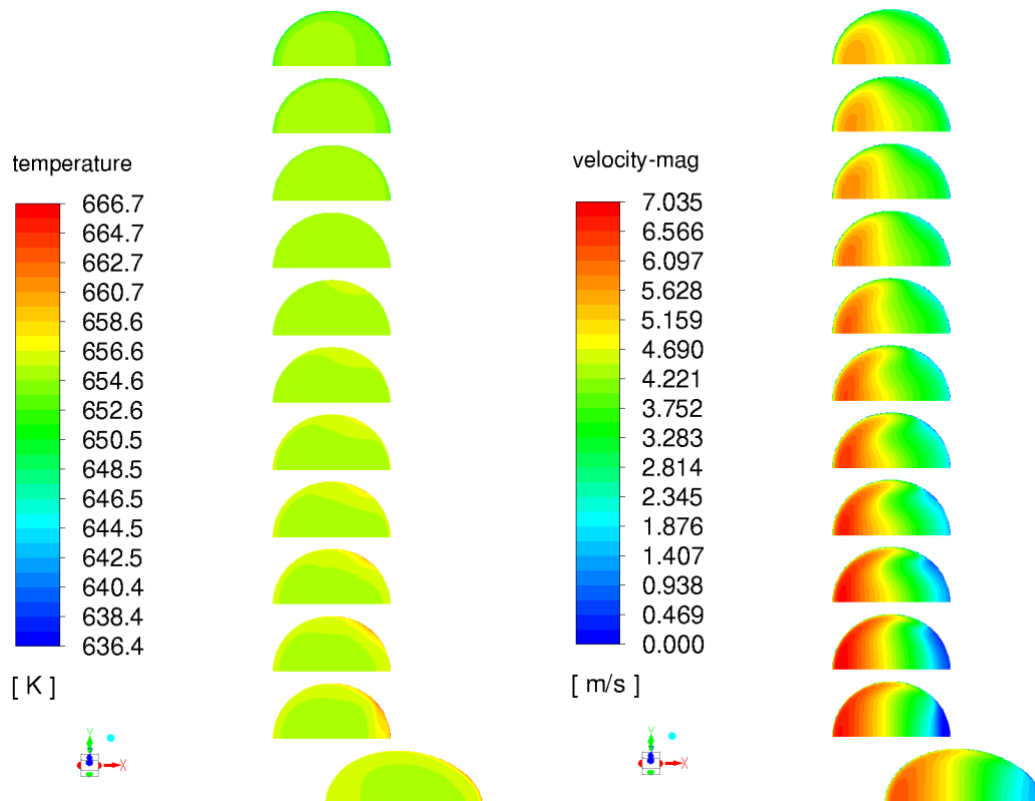


Figure 66: Hot leg pipe temperature and velocity-magnitude distribution in a time 66 s

In Figure 66, which shows the velocity and temperature distribution in the inlet pipe, it can be seen that the temperature is practically uniform throughout the space and is related to the temperature at the inlet to the hot leg. In the case of velocity, the figure shows the drift that occurs on the inside of the bend in the pipe, where the flow slows down significantly to practically stagnation.

At the moment when the hot and cold legs are connected, two factors begin to act simultaneously. Firstly, a boundary condition is set that determines the pressure difference at the two inlets (see Figure 51), and secondly, helium of significantly different temperatures and therefore densities comes into contact. In the cold leg, the average temperature at the time of opening is approximately  $525\text{ K}$ , whereas the active part of the exchanger, with the exception of HEX1, is filled with helium cooled to  $365 - 375\text{ K}$ . For density, this means a difference of  $2.5\text{ kg/m}^3$ . Both factors thus facilitate the natural circulation of helium in the direction from the hot to the cold leg.

The result of the action of these two factors can be seen in Figure 67, which displays the temperature and velocity contours  $v(z)$  at the top of the cold leg at time  $t = 57\text{ s}$ , i.e.  $1\text{ s}$  after the flaps in the baffle have been opened. The temperature distribution shows very well how the cooled helium from the heat exchanger starts to flow into the cold leg distribution chamber. The turnover of the flow that occurs in the outlet pipe below the chamber can also be seen.

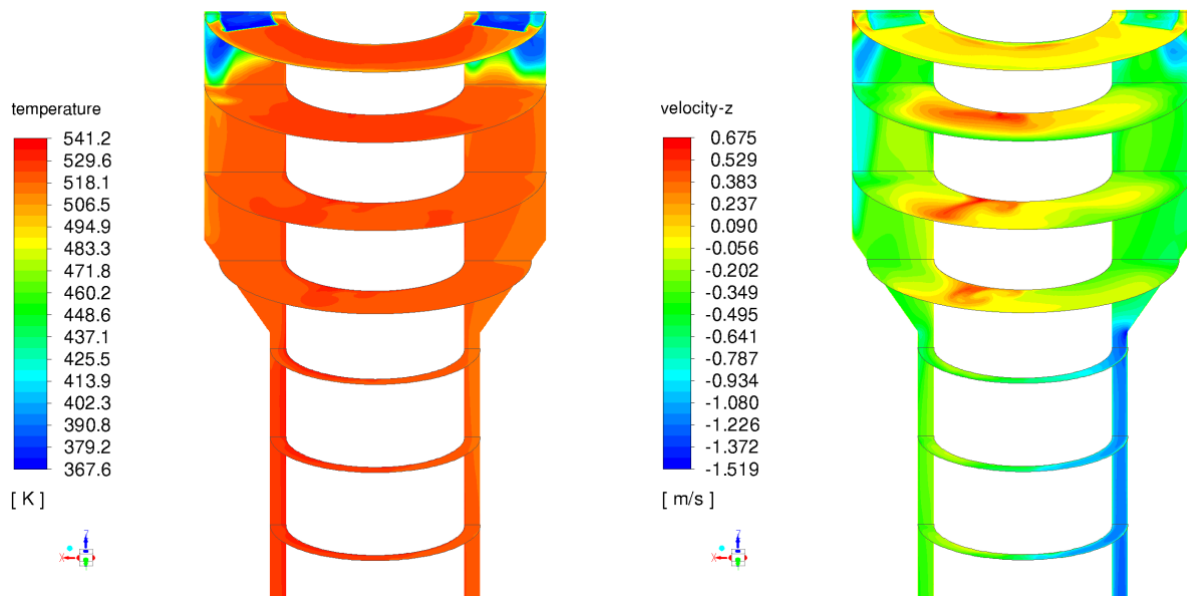


Figure 67: Cold leg pipe temperature and z-velocity distribution in a time 57 s

The temperature and velocity distribution  $v(z)$  at time  $t = 59\text{ s}$  in Figure 68 shows the intensity of the flow of cooled helium from the heat exchanger towards the cold leg distribution chamber. The cold tongues below the flaps already reach the top of the cold leg piping and the average helium temperature in the chamber has dropped by almost  $35\text{ K}$ , see also Figure 69. The velocity profile shows that the flow in the cold leg pipe is already completely reversed downwards in its entire cross-section.

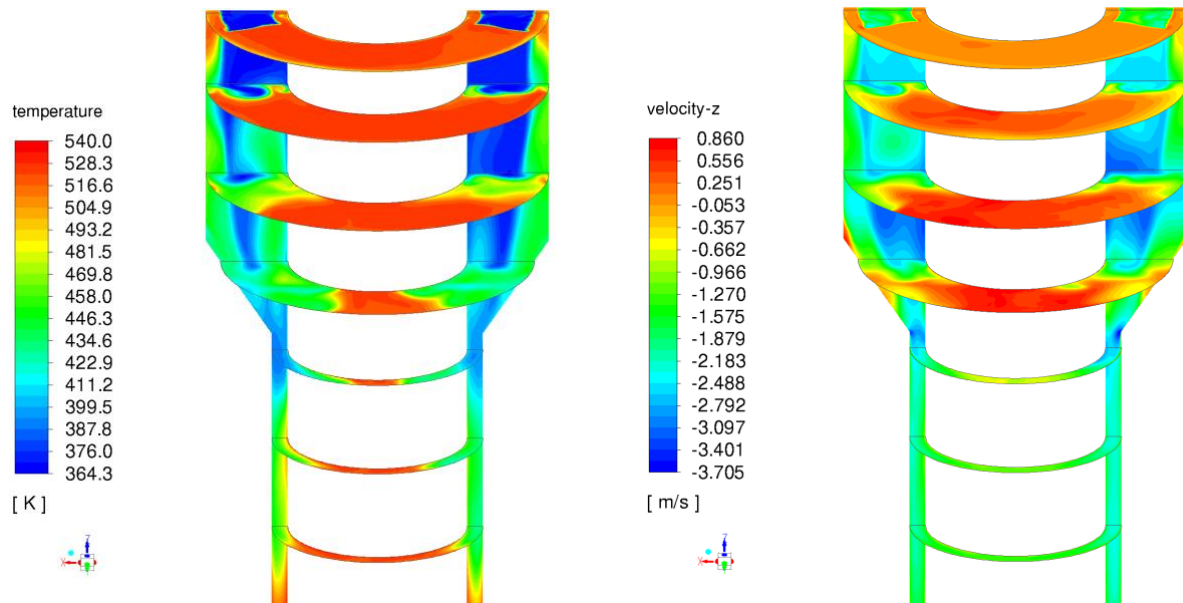


Figure 68: Cold leg pipe temperature and z-velocity distribution in a time 59 s

The continued development of the temperature field in the distribution chamber and cold leg piping is shown in Figure 69. The maximum cooling in the chamber is reached at time  $t = 62$  s, with the temperature decreasing by approximately 55 K. Subsequently, the trend reverses and the temperature gradually increases due to a helium inflow of temperature about 500 K. In the case of the cold leg pipe, the decrease occurs with a delay of about 2.5 s and the lowest temperature is reached at time  $t = 63$  s, with a temperature difference of up to 65 K.

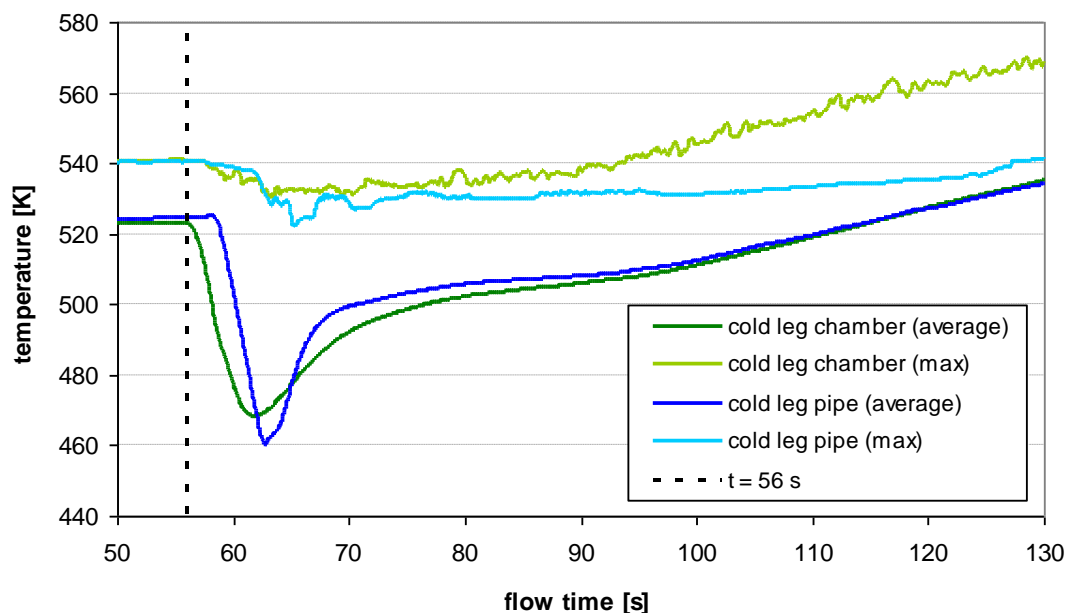


Figure 69: Time temperature profiles in parts of cold leg

Figure 70 shows the situation at the top of the cold leg at time  $t = 62$  s. This is the time when the temperature drop in the cold leg chamber is maximal. A significant cooling can

be seen practically in the whole space. The higher temperature helium is only held below the baffle. At the same time, an increase in the minimum helium temperature can be seen due to helium flowing from the heat exchanger outlet chamber that already has not been cooled to such low temperatures.

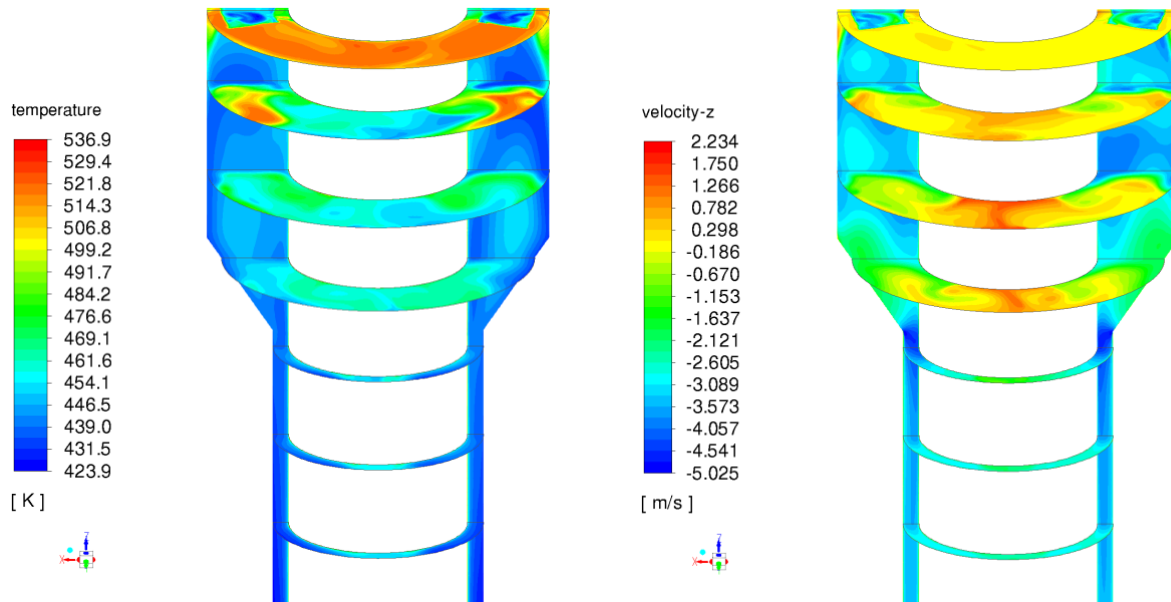


Figure 70: Cold leg pipe temperature and z-velocity distribution in a time 62 s

The gradual development of the temperature field in the cold leg distribution chamber for times  $t = 64$  s to  $t = 70$  s is shown in Figure 71. It shows a gradual inflow of warmer helium and a clear equalization of the temperature field across the entire cold leg distribution chamber.



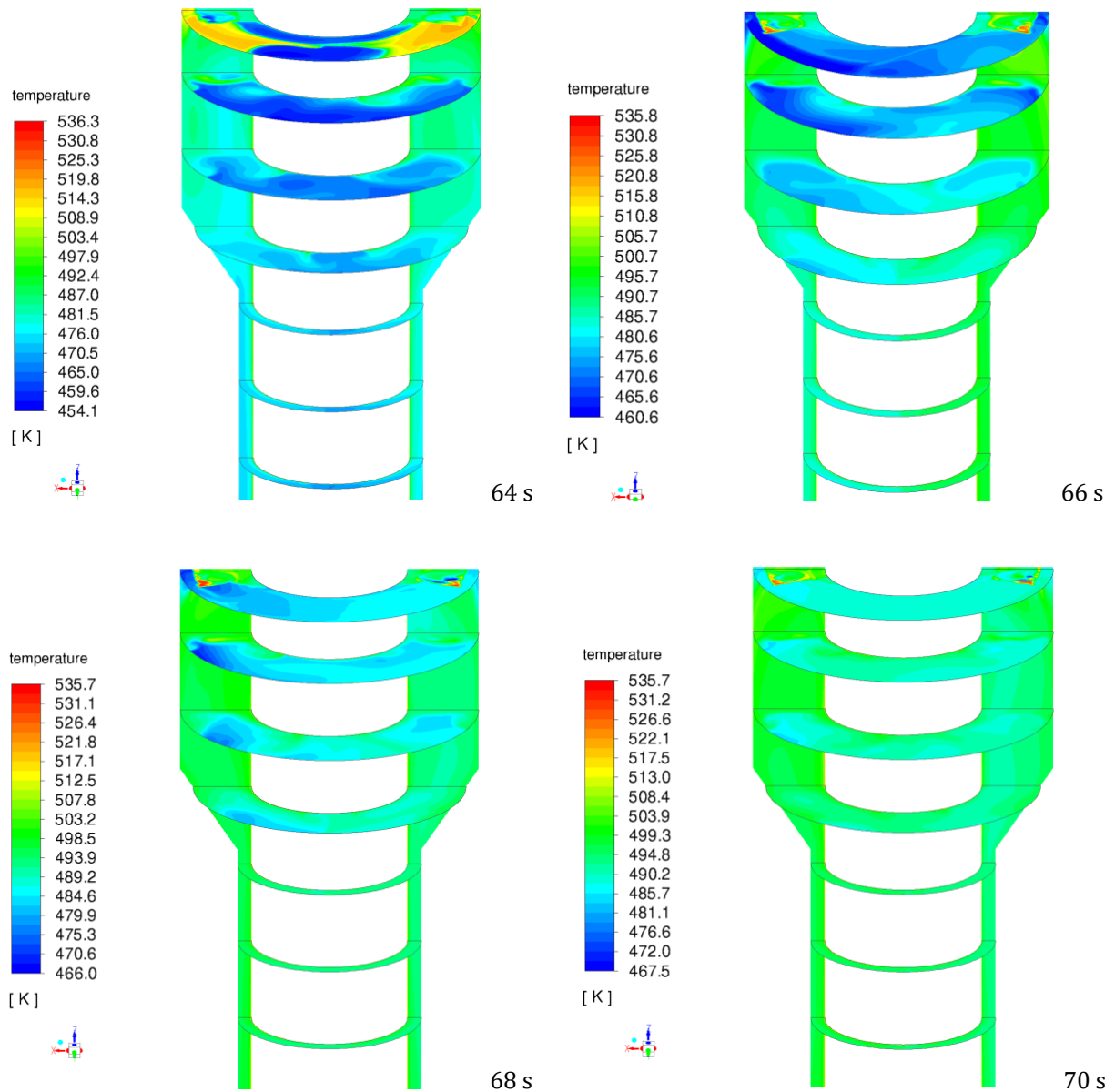


Figure 71: Cold leg pipe temperature distribution in a given times

Figure 72 shows the distribution of temperature and velocity  $v(z)$  on selected cross-sections of the cold leg at time  $t = 80$  s. This character of the flow in the cold leg space subsequently remains the same until the end of the simulated transient. It can be seen that the temperature distribution is largely uniform throughout the space and that the backflow in the distribution chamber space continues to persist.

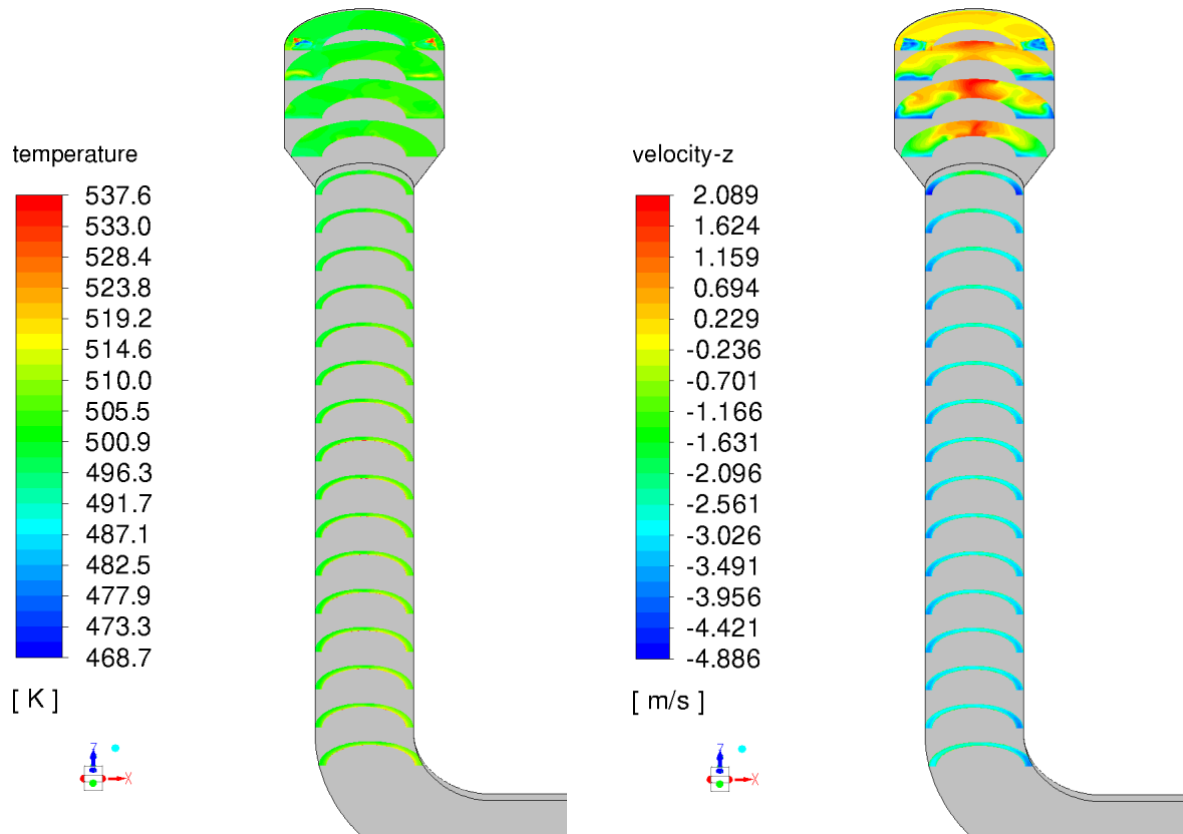


Figure 72: Cold leg pipe temperature and z-velocity distribution in a time 80 s

### 8.3 SUMMARY

The analyses performed on the Test Model were used to prepare the Complex Model. The newly developed model was designed to simulate two basic tasks. The first problem represents the nominal operating condition and the results obtained describe the basic helium temperature and velocity fields throughout the DHR system. The subsequent problem simulates the initial part of the emergency condition with complete loss of power. The results of the solved transient, defined according to [7], demonstrate the capability of the DHR system to set up a natural circulation after the interconnection of hot and cold leg and determine the expected amount of power removed in the initial part of the modelled emergency condition.

## 9 CONCLUSION

The main objective of Deliverable 3.4 was to perform a detailed study of conditions in isolated DHR loop in long-term reactor operation. The study included also verification of loop operability during a defined emergency condition. For these reasons, two basic scenarios of loop operation were simulated - during normal operation and during a defined design accident with complete loss of power.

During normal reactor operation, the DHR loop is closed at the point of the baffle that separates the hot and cold legs. In this condition, only partial circulation of helium occurs, separately in the hot and cold legs of the loop. The power transferred to the cooling water from the hot leg and, through the steel partition, also partially from the cold leg, reaches a level of *70 kW* (or *140 kW* for the whole symmetry). The condition of the insulated loop was described in Section 8.1.

The transient scenario simulates the beginning of an accident with complete loss of power. After reactor shutdown ( $t = 0$  s), the main compressor is running out (to  $t = 56$  s) and subsequently, at the interface of the cold and hot legs of the DHR loop, the flaps in the steel baffle are opened to allow flow through the loop to cool the heated helium flowing from the region above the core. The simulation of the transient is terminated at time  $t = 126$  s after reactor shutdown. The simulation of the considered scenario was divided into two phases. In the first phase of the transient, changes in boundary conditions occur only at the reactor/DHR loop interface until the flaps in the steel baffle separating the hot and cold leg of the loop open ( $t = 56$  s). The next phase of the calculation simulates the start of the helium circulation after the two legs have been connected, until the end of the scenario at  $t = 126$  s. The two phases of the accident process considered are described in Section 8.2.

The prepared report describes a detailed study of the operating conditions of the isolated DHR loop both at the nominal operating condition of the ALLEGRO reactor and at the initial part of the emergency condition with complete loss of coolant according to [7]. Simulations of the transient scenario have confirmed the functionality of the DHR system, which, after opening the flaps in the baffle separating the hot and cold loop legs, very quickly activates the natural helium circulation capability. The establishment of natural circulation occurs within seconds after the two legs are connected. Removed power for the next *10 s* ( $t = 66$  s) reaches *2100 kW* (or *4200 kW* for the whole symmetry). Thereafter, there is a gradual decrease to *1500 kW* (or *3000 kW* for the whole symmetry) at the end of the simulated transient ( $t = 126$  s).

Based on the obtained results, it can be concluded that the main objective of Deliverable 3.4 (Detailed study of conditions in isolated DHR loop in long-term reactor operation) has been met. For the purposes of comprehensive assess the functionality of the DHR loop, the simulation results of the initial part of the design accident with complete loss of power were added beyond the Deliverable requirement.

## 10 REFERENCES

- [1] ANSYS Fluent Theory Guide, Release 18.2. Ansys Inc., Southpointe, 2600 Canonsburg, PA 15317, USA, January 2017
- [2] ANSYS Fluent Users Guide, Release 18.2. Ansys Inc., Southpointe, 2600 Canonsburg, PA 15317, USA, January 2017
- [3] C. Poette et al.: ALLEGRO 75 MW system definition at start of GOFASTR, FP7 GoFastR del.1.2-02, 2010
- [4] G. Mayer, F. Bentivoglio: Preliminary study of the decay heat removal strategy for the gas demonstrator ALLEGRO, Nuclear Engineering and Design 286 (2015), p. 67-76
- [5] C. Poette et al.: ALLEGRO Preliminary Viability Report, CEA/DEN/CAD/DER/SESI/LCSI/NT D012, 2009
- [6] M. Lackova et. al: Summary of input data of ALLEGRO demonstrator for deterministic safety analyses (ALLEGRO Database), 2016
- [7] SBO scenario dataset, RELAP program, UJV Rez 2022